CORROSION OF UO_2 AND THERMODYNAMIC PROPERTIES OF SOLID SOLUTIONS IN THE ZIRCON GROUP

by

Elizabeth D. A. Ferriss

A dissertation submitted in partial fulfillment
of the requirements for the degree of
Doctor of Philosophy
(Geology)
in The University of Michigan
2009

Doctoral Committee:

Associate Professor Udo Becker, Co-Chair
Professor Rodney C Ewing, Co-Chair
Professor Emeritus Eric J Essene
Professor Youxue Zhang
Assistant Professor Anton van der Ven

ACKNOWLEDGMENTS

First, thank you to my co-chairs Rod Ewing and Udo Becker. Also thanks to my co-authors Pat Brady, Charles Bryan, Eric Essene, and especially Kate Helean. I am grateful to my other committee members past and present: Youxue Zhang, Anton van der Ven, Lars Stixrude, and Kim Hayes. Also to my husband Mark, who provided a fabulous last name, abundant encouragement, and mad formatting skills. Peter van Keken and Eric Kneller taught me essentially everything I know about programming. Artur Deditius, Carl Henderson, and Eric Essene were particularly helpful with the EMPA/WDS and SEM/EDS work. Corey Lambert and Ted Huston were always patient and willing to help me with my latest project. I would not have gotten far at all without Anne Hudon and the rest of the office staff. Lynn Walter was wonderful in helping to get me settled in my first year. Two anonymous reviewers and Thomas Zack provided comments that lead to a substantial improvement in the manuscripts for Chapters 2 and 4. Thanks to Satoshi Utsunomiya and Edgar Buck for discussion about the applicability of TEM to the work described in Chapter 4. Edgar also hosted me for an internship at PNNL. Thanks to Charles Anderson (hi dad!) for the statistics work. Thank you also to my fellow students and friends, particularly Frannie Skomurski (U), Lindsay Shuller (Np), Qiaona Hu ("Joanna"), Monamie (Bhadra) and Sam Haines, the "Friday Night Coven", Sarah Rilling, Darius Dixon, Subhashis

Biswas, Cheryl Peyer, Chris Stefano, Devon Renock, J.P. Brandenburg, and Martin Reich.

Financial support came in the form of fellowships from the Dept. of Geological Sciences (1st year), the U.S. Department of Energy Office for Civilian Radioactive Waste Management (2nd year), and the National Science Foundation (3rd-5th years). This work was supported by the Office of Science and Technology and International (OST&I) of the Office of Civilian Radioactive Waste Management (DE-FE28-04RW12254) and NSF-NIRT (EAR-0403732). Many of the computations in Chapter 3 were performed on the University of Michigan Legato cluster (funded through National Science Foundation grant EAR-0651056 to Peter van Keken and Jeroen Ritsema).

CONTENTS

LIST OF FIGURES

LIST OF TABLES

LIST OF APPENDICES

ABSTRACT

Corrosion resistance and the ability to incorporate and retain impurities are important properties in determining the usefulness of a material for applications as varied as designing a nuclear waste form or calculating the temperature or time at which a particular rock formed. This thesis applies both experimental and computational techniques in order to gain insight into the corrosion and substitution behavior of actinide oxides and orthosilicates.

Experimental studies of uraninite corrosion in miniature waste packages show that oxidation of UO_2, a proxy for spent nuclear fuel (SNF), is minimal in the presence of a relatively large amount of corroding steel over laboratory time-scales. The oxidative dissolution of spent nuclear fuel in an oxidizing repository with a steel canister may be broken into three phases: (1) before breach, when no water is available and the corrosion rate is negligible, (2) immediately after breach, when the steel begins to corrode, conditions inside of the canister are more reducing, and SNF does not corrode significantly, and (3) long after breach, SNF is exposed to the open air and oxidized.

The common accessory mineral zircon ($ZrSiO_4$) is considered a host phase for Pu and other elements using a combination of quantum-mechanical and Monte-Carlo simulations. Results show that while hafnon ($HfSiO_4$) and zircon form a nearly ideal

solid solution, the maximum amount of Pu, U, Th, and Ce that can be incorporated at thermodynamic equilibrium is extremely limited and can be ranked in the following order: $(Zr,Hf)SiO_4$ > $(Th,U)SiO_4$ > $(Zr,Ce)SiO_4$ > $(Zr,Pu)SiO_4$ > $(Hf,Pu)SiO_4$ > $(Zr,U)SiO_4$ > $(Zr,Th)SiO_4$.

Calculations on Ti incorporation in zircon for use as a geothermometer confirm that Ti prefers to occupy the Si site at pressures below 1 GPa. However, at higher pressures, particularly above 3.5 GPa, substitution into the Zr site is preferable. Results suggest a pressure correction of 100 °C/GPa at 750 °C, twice as large as a previous estimate. The Ti-in-zircon geothermometer must be recalibrated if it is to be used on ultra-high pressure samples.

CHAPTER 1.
INTRODUCTION

Corrosion resistance and the ability to incorporate and retain impurities are important properties in determining the usefulness of a material for applications as varied as designing a nuclear waste form or calculating the temperature or time at which a particular rock formed. Crystalline UO_2 (space group $Fm3m$) is of particular interest as the mineral uraninite (the most important ore for U) and as a proxy for spent nuclear fuel. The orthosilicate zircon ($ZrSiO_4$, $I4_1/amd$) is also important for both nuclear and geoscience applications. This thesis applies both experimental and computational techniques in order to gain insight into the corrosion and substitution behavior of actinide oxides and orthosilicates.

Chapters 2 and 3 are primarily motivated by the need for a durable waste form for long-term disposal of actinides created in nuclear reactors (*e.g.*, Pu, Np, Am and Cm). Used or "spent" nuclear fuel (SNF) consists almost entirely of cubic UO_2, which for a typical burn-up (40 MWd/kg U), will consist of about 1 wt. % Pu and 2-3 wt. % fission products, such as ^{99}Tc and ^{129}I (Oversby, 1994). The license application that was recently submitted by the U.S. Department of Energy to the U.S. Nuclear Regulatory Commission proposes to dispose of the used fuel rods by placing them directly in steel waste containers in tunnels at Yucca Mountain, Nevada (DOE, 2008). In this scenario, the SNF itself will be the long-term waste form for all

actinides and fission products (*e.g.*, ^{99}Tc), and the release of radionuclides will be largely governed by the corrosion rate of the SNF in this oxidizing environment. An alternative strategy is to incorporate individual radionuclides into more durable ceramic materials such as perovskite ($(Ca,Sr)TiO_3$), pyrochlore ($Gd_2(Ti,Hf)_2O_7$), or monazite ($(REE)PO_4$) (Lutze and Ewing, 1988; Ringwood et al., 1979). In an extension of this approach, the mineral zircon ($ZrSiO_4$) has been proposed as a waste form for Pu (Ewing et al., 1995). This suggestion relies on the chemical and mechanical durability of zircon and its ability to incorporate actinides for very long periods of time (Cherniak et al., 1997). However, the maximum waste-loading (the amount that may be incorporated) of Pu in zircon is uncertain (Lumpkin, 2006).

Chapter 2 examines the behavior of UO_2 powder as a proxy for SNF in the presence of a steel waste package surrounded by an oxidizing environment (air). Under oxidizing conditions, UO_2 typically alters to the ion UO_2^{2+}, which forms a variety of mobile aqueous complexes such as $(UO_2)_2CO_3(OH)^{3-}$, $UO_2CO_3^0$, $UO_2(CO_3)_2^{2-}$, and $UO_2(CO_3)_3^{4-}$ (Grenthe et al., 1992; Wronkiewicz et al., 1996; Murphy and Shock, 1999; Kubatko et al., 2006). However, relatively little attention has been paid to the effect of corroding steel, which may produce radionuclide-sorbing oxidation products such as magnetite (Fe_3O_4) (Grambow et al., 1996; Dunn et al., 2000; Dodge et al., 2002; Missana et al., 2003; Scott et al., 2005; Rovira et al., 2007; Duro et al., 2008) and green rust ($Fe(II)_{1-x}Fe(III)_x(OH)_2Y_{x/n}$) (O'Loughlin et al., 2003) and may also influence the redox potential and pH inside the waste package. In order to simulate the behavior of SNF in a corroding waste package, a series of six miniature steel waste packages containing carbon steel inserts were constructed, and

the nature of the steel corrosion products, local redox and pH conditions inside these waste packages, and resulting uranium mineralogy and mobility in these packages after 0.5-2 years are presented. These results were used to construct a new conceptual model for the long-term stability of spent nuclear fuel in steel waste packages, as planned at the proposed nuclear waste repository at Yucca Mountain.

Chapter 3 addresses the thermodynamic stability of solid solutions having the zircon structure using a combination of quantum-mechanical and Monte-Carlo methods. Particular emphasis has been placed on calculating the incorporation limit of Pu and its chemical analogue, Ce, in the proposed waste form, zircon. The initiation of a nuclear chain reaction when a critical mass is achieved, is a concern when concentrations of Pu exceed a few weight percent (Ushakov et al., 1999). In order to decrease the risk of a criticality event (Weber et al., 1996; Meldrum et al., 1999; Burakov et al., 2000), ^{174}Hf, which has a high neutron absorption cross-section (561 barn for 2200 m/s neutrons), may be added. Therefore, solid solutions that include Hf (*e.g.*, $ZrSiO_4$-$HfSiO_4$ and $PuSiO_4$-$HfSiO_4$) are also important. The stability, ordering and exsolution patterns, and incorporation limits are determined as a function of temperature for each of these solid solutions using Monte-Carlo methods.

Simulations of impurities in zircon, such as those described for Pu and Hf in Chapter 3, are also of great interest for geologic applications. Zircon has long been used by geoscientists for U/Th/Pb age-dating and thermochronology based on the release of He. Lu/Hf and ^{176}Hf/^{177}Hf ratios have been used to determine crustal residence and growth, as well as the sources of the magma from which zircon formed,

and rare earth element (REE) distributions provide further insight into magmatic histories (Harley and Kelly, 2007; Hawkesworth and Kemp, 2006; Scherer et al., 2007). Chapter 3 presents computational simulations of five solid solutions of geologic interest: $(Zr,Hf)SiO_4$, $(Zr,U)SiO_4$, $(Zr,Th)SiO_4$, $(Zr,Ce)SiO_4$, and $(U,Th)SiO_4$. Naturally occurring minerals with the zircon structure include $USiO_4$ (coffinite), $ThSiO_4$ (thorite), and $HfSiO_4$ (hafnon). The anomalously high Ce content of some natural zircons relative to other REE has been attributed to the presence of some Ce^{4+} (Hinton and Upton, 1991)., which has been confirmed using X-ray absorption near-edge structure (XANES) (Takahashi et al., 2003). Ce^{4+} may substitute directly for Zr^{4+} rather than undergoing, for instance, the xenotime-type coupled substitution, in which REE^{3+} substitutes for Zr^{4+} while P^{5+} substitutes for Si^{4+}, that is often used to explain the incorporation mechanism of REE in zircon (Finch et al., 2001; Speer, 1982). The incorporation mechanism for these cations in the zircon structure is predominantly by direct substitution into the 8-fold Zr site, although some incorporation may also occur at interstitial sites (Begg et al., 2000; Williford et al., 2000; Finch and Hanchar, 2003). For smaller cations such as Ti^{4+} the incorporation mechanism in zircon is less well understood, particularly as a function of pressure.

The Ti content of zircon has also been suggested to give a direct indication of the temperature of crystallization (or metamorphic growth), providing insight into the major geologic conditions and processes operating during Earth's distant past such as minimum melting conditions during the Hadean Eon (Watson and Harrison, 2005; Watson et al., 2006; Ferry and Watson, 2007). Chapter 4 investigates the Ti-in-zircon

geothermometer using a combination of quantum mechanical calculations and Monte-Carlo simulations in order to ascertain the incorporation mechanism of Ti in the structure as a function of pressure (i.e., does Ti substitute for Si or Zr?) and the usefulness of this thermometer at higher pressures. Ti is typically found in octahedral coordination (Stoyanov et al., 2007), and tabulations of ionic radii (e.g., Shannon, 1976) indicate no clear preference of Ti for the IV-coordinated Si site, as compared with the VIII-coordinated Zr site. Experiments involving zircon crystallization in the presence of SiO_2 and TiO_2 indirectly suggest that substitution of Ti into the Si site dominates (Ferry & Watson, 2007), but this cannot be confirmed using more direct methods because Ti concentrations in zircon are typically below 20 ppm (Fu et al., 2008) and reach a maximum at about 100 ppm (Harley and Kelly, 2007). Two incorporation mechanisms are compared using two different conceptual approaches: (1) as two different reactions ($TiO_2 + ZrSiO_4 \leftrightarrow ZrO_2 + TiSiO_4$) and ($TiO_2 + ZrSiO_4 \leftrightarrow SiO_2 + ZrTiO_4$), and (2) as two different solid solutions $(Zr,Ti)SiO_4$ and $Zr(Si,Ti)O_4$. In addition, the molar volume of $ZrTiO_4$ ($I4_1/amd$) was calculated and used to suggest a new pressure correction for the Ti-in-zircon geothermometer.

Two appendices provide additional information. Appendix A contains procedural details for the Fe speciation method developed as part of the research program described in chapter 2. Appendix B is a computational investigation of the use of Re as an analogue for the geochemical behavior of Tc. The isotope ^{99}Tc is a particularly important radionuclide because it is mobile in most geochemical environments and has a long half-life (212,000 years). The use of non-radioactive analogues is common, particularly during the initial phases of a study (Pepin et al.,

1981; Brookins, 1986; Vance, 1994; Darab and Smith, 1996; Ushakov et al., 1998; Xu and Wang, 1999). Quantum mechanics is used to calculate the absorption and electronic behavior of the radionuclide Tc and its chemical analogue Re in the presence of a galena (PbS) surface, and the chemistry of the two elements is compared.

1.1. References

Begg, B.D., Hess, N.J., Weber, W.J., Conradson, S.D., Schweiger, M.J., and Ewing, R.C. (2000) XAS and XRD study of annealed Pu-238- and Pu-239-substituted zircons ($Zr_{0.92}Pu_{0.08}SiO_4$). Journal of Nuclear Materials, 278(2-3), 212-224.

Brookins, D.G. (1986) Rhenium as analog for fissiogenic technetium: Eh-pH diagram (25 °C 1 bar) constraints. Applied Geochemistry, 1, 513-517.

Burakov, B.E., Anderson, E.B., Zamoryanskaya, M.V., Yagovkina, M.A., Strykanova, E.E., and Nikolaeva, E.V. (2000) Synthesis and study of Pu-239-doped ceramics based on zircon, $(Zr,Pu)SiO_4$, and hafnon, $(Hf,Pu)SiO_4$. Scientific Basis for Nuclear Waste Management XXIV, 663, 307-313.

Cherniak, D.J., Hanchar, J.M., and Watson, E.B. (1997) Diffusion of tetravalent cations in zircon. Contributions to Mineralogy and Petrology, 127, 383-390.

Darab, J.G., and Smith, P.A. (1996) Chemistry of technetium and rhenium species during low-level radioactive waste vitrification. Chemistry of Materials, 8(5), 1004-1021.

Dodge, C.J., Francis, A.J., Gillow, J.B., Halada, G.P., Eng, C., and Clayton, C.R. (2002) Association of uranium with iron oxides typically formed on corroding steel surfaces. Environmental Science & Technology, 36(16), 3504-3511.

DOE. (2008) Yucca Mountain Repository License Application. Department of Energy.

Dunn, D.S., Bogart, M.B., Brossia, C.S., and Cragnolino, G.A. (2000) Corrosion of iron under alternating wet and dry conditions. Corrosion, 56(5), 470-481.

Duro, L., El Aamrani, S., Rovira, M., de Pablo, J., and Bruno, J. (2008) Study of the interaction between U(VI) and the anoxic corrosion products of carbon steel. Applied Geochemistry, 23(5), 1094-1100.

Ewing, R.C., Lutze, W., and Weber, W.J. (1995) Zircon - a host-phase for the disposal of weapons plutonium. Journal of Materials Research, 10(2), 243-246.

Ferry, J.M., and Watson, E.B. (2007) New thermodynamic models and revised calibrations for the Ti-in-zircon and Zr-in-rutile thermometers. Contributions to Mineralogy and Petrology.

Finch, R.J., and Hanchar, J.M. (2003) Structure and chemistry of zircon and zircon-group minerals. In J.M. Hanchar, and P.W.O. Hoskin, Eds. Zircon, 53, p. 1-21. Mineralogical Society of America, Washington, D.C.

Finch, R.J., Hanchar, J.M., Hoskin, P.W.O., and Burns, P.C. (2001) Rare-earth elements in synthetic zircon: Part 2. A single-crystal X-ray study of xenotime substitution. American Mineralogist, 86(5-6), 681-689.

Fu, B., Page, F.Z., Cavosie, A.J., Fournelle, J., Kita, N.T., Lackey, J.S., Wilde, S.A., and Valley, J.W. (2008) Ti-in-zircon thermometry: applications and limitations. Contributions to Mineralogy and Petrology, 156(2), 197-215.

Grambow, B., Smailos, E., Geckeis, H., Muller, R., and Hentschel, H. (1996) Sorption and reduction of uranium(VI) on iron corrosion products under reducing saline conditions. Radiochimica Acta, 74, 149-154.

Grenthe, I., Fuger, J., Konings, R., Lemire, R.J., Muller, A.B., Nguyen-Trung, C., and Wanner, J. (1992) The Chemical Thermodynamics of Uranium. Elsevier.

Harley, S.L., and Kelly, N.M. (2007) Zircon - tiny but timely. Elements, 3(1), 13-18.

Hawkesworth, C.J., and Kemp, A.I.S. (2006) Using hafnium and oxygen isotopes in zircons to unravel the record of crustal evolution. Chemical Geology, 226(3-4), 144-162.

Hinton, R.W., and Upton, B.G.J. (1991) The chemistry of zircon - variations within and between large crystals from syenite and alkali basalt xenoliths. Geochimica et Cosmochimica Acta, 55(11), 3287-3302.

Kubatko, K.A., Helean, K., Navrotsky, A., and Burns, P.C. (2006) Thermodynamics of uranyl minerals: Enthalpies of formation of uranyl oxide hydrates. American Mineralogist, 91(4), 658-666.

Lumpkin, G.R. (2006) Ceramic waste forms for actinides. Elements, 2(6), 365-372.

Lutze, W., and Ewing, R.C. (1988) Radioactive Waste Forms for the Future, 778 p. North-Holland Physics Publishing, Amsterdam.

Meldrum, A., Zinkle, S.J., Boatner, L.A., and Ewing, R.C. (1999) Heavy-ion irradiation effects in the ABO_4 orthosilicates: Decomposition, amorphization, and recrystallization. Physical Review B, 59(6), 3981-3992.

Missana, T., Maffiotte, U., and Garcia-Gutierrez, M. (2003) Surface reactions kinetics between nanocrystalline magnetite and uranyl. Journal of Colloid and Interface Science, 261(1), 154-160.

Murphy, W.M., and Shock, E.L. (1999) Environmental aqueous geochemistry of actinides. In P.C. Burns, and R.J. Finch, Eds. Uranium: Mineralogy, Geochemistry and the Environment, 38, p. 221-253. Mineralogical Society of America, Washington, D.C.

O'Loughlin, E.J., Kelly, S.D., Cook, R.E., Csencsits, R., and Kemner, K.M. (2003) Reduction of Uranium(VI) by mixed iron(II)/iron(III) hydroxide (green rust): formation of UO2 nanoparticles. Environmental Science and Technology, 37, 721-727.

Oversby, V.M. (1994) Nuclear Waste Materials. In B.R.T. Frost, Ed. Material Science and Technology: a Comprehensive Treatment, p. 392. VCH, Weinheim, Germany.

Pepin, J.G., Vance, E.R., and McCarthy, G.J. (1981) The crystal-chemistry of cerium in the monazite structure-type phase of tailored-ceramic nuclear waste forms. Materials Research Bulletin, 16(6), 627-633.

Ringwood, A.E., Kesson, S.E., Ware, N.G., Hibberson, W., and Major, A. (1979) Immobilization of High-Level Nuclear-Reactor Wastes in Synroc. Nature, 278(5701), 219-223.

Rovira, M., El Aamrani, S., Duro, L., Gimenez, J., de Pablo, J., and Bruno, J. (2007) Interaction of uranium with in situ anoxically generated magnetite on steel. Journal of Hazardous Materials, 147(3), 726-731.

Scherer, E.E., Whitehouse, M.J., and Munker, C. (2007) Zircon as a monitor of crustal growth. Elements, 3(1), 19-24.

Scott, T.B., Allen, G.C., Heard, P.J., and Randell, M.G. (2005) Reduction of U(VI) to U(IV) on the surface of magnetite. Geochimica Et Cosmochimica Acta, 69(24), 5639-5646.

Shannon, R.D. (1976) Revised effective ionic-radii and systematic studies of interatomic distances in halides and chalcogenides. Acta Crystallographica Section A, 32(SEP1), 751-767.

Speer, J.A. (1982) Zircon. In P.H. Ribbe, Ed. Orthosilicates, 5. Mineralogical Society of America, Washington, D.C.

Stoyanov, E., Langenhorst, F., and Steinle-Neumann, G. (2007) The effect of valence state and site geometry on Ti L-3,L-2 and OK electron energy-loss spectra of Ti_xO_y phases. American Mineralogist, 92(4), 577-586.

Takahashi, Y., Sakashima, T., and Shimizu, H. (2003) Observation of tetravalent cerium in zircon and its reduction by radiation effect. Geophysical Research Letters, 30(3).

Ushakov, S.V., Burakov, B.E., Garbuzov, V.M., Anderson, E.B., Strykanova, E.E., Yagovkina, M.M., Helean, K.B., Guo, Y.X., Ewing, R.C., and Lutze, W. (1998) Synthesis of Ce-doped zircon by a sol-gel process. Scientific Basis for Nuclear Waste Management XXI, 281-288.

Ushakov, S.V., Gong, W., Yagovkina, M.M., Helean, K.B., Lutze, W., and Ewing, R.C. (1999) Solid solutions of Ce, U, and Th in zircon. Environmental Issues and Waste Management Technologies in the Ceramic and Nuclear Industries IV, 93, 357-363.

Vance, E.R. (1994) Synroc - a Suitable Waste Form for Actinides. Material Research Society Bulletin, 19(12), 28-32.

Watson, E.B., and Harrison, T.M. (2005) Zircon thermometer reveals minimum melting conditions on earliest Earth. Science, 308(5723), 841-844.

Watson, E.B., Wark, D.A., and Thomas, J.B. (2006) Crystallization thermometers for zircon and rutile. Contributions to Mineralogy and Petrology, 151(4), 413-433.

Weber, W.J., Ewing, R.C., and Lutze, W. (1996) Performance assessment of zircon as a waste form for excess weapons plutonium under deep borehole burial conditions. Scientific Basis for Nuclear Waste Management XIX, 412, 25-32.

Williford, R.E., Begg, B.D., Weber, W.J., and Hess, N.J. (2000) Computer simulation of Pu^{3+} and Pu^{4+} substitutions in zircon. Journal of Nuclear Materials, 278(2-3), 207-211.

Wronkiewicz, D.J., Bates, J.K., Wolf, S.F., and Buck, E.C. (1996) Ten-year results from unsaturated drip tests with UO_2 at 90 °C: implications for the corrosion of spent nuclear fuel. Journal of Nuclear Materials, 238(1), 78-95.

Xu, H.F., and Wang, Y.F. (1999) Electron energy-loss spectroscopy (EELS) study of oxidation states of Ce and U in pyrochlore and uraninite - natural analogues for Pu- and U-bearing waste forms. Journal of Nuclear Materials, 265(1-2), 117-123.

1.2. Publications and Abstracts Resulting from this Disssertation

1.2a. Publications

Ferriss, E.D.A., Helean, K.B., Bryan, C.R., Brady, P.V., and Ewing, R.C. (2009) UO_2 corrosion in an iron waste package. Journal of Nuclear Materials, 384, 130-139. **(Chapter 2)**

Ferriss, E.D.A., Ewing, R.C., and Becker, U. (2009) Simulation of thermodynamic mixing properties of actinide-containing orthosilicate solid solutions. American Mineralogist, *submitted.* **(Chapter 3)**

Ferriss, E.D.A., Essene, E.J., and Becker, U. (2008) Computational study of the effect of pressure on the Ti-in-zircon geothermometer. European Journal of Mineralogy, 20(5), 745-755. **(Chapter 4)**

Husler, J.W., Ferriss, E.D.A., Helean, K., Bryan, C.R., and Brady, P.V. (2009) Optimized ferrozine method for determination of ferrous and ferric iron in minerals. Geostandards and Geoanalytical Research, *submitted*. **(Appendix A)**

Ferriss, E.D.A., Becker, U., and Ewing, R.C. (2009) Critical evaluation of Re as an analogue for Tc. Journal of Nuclear Materials, *in preparation*. (extension of Appendix B)

1.2b. Conference Proceedings

Ferriss, E. D. A., Helean, K. B., Bryan, C. R., Brady, P. V., and Ewing, R. C. (2009) UO_2 corrosion in an iron waste package, Scientific Basis for Nuclear Waste Management XXXII, Proceedings of the Materials Research Society, *in press.*

Anderson, B.E. *(former name)*, Helean, K.B., Bryan, C.R., Brady, P.V., and Ewing, R.C. (2008) Waste package corrosion studies using small mockup experiments. Scientific Basis for Nuclear Waste Management XXXI, Proceedings of the Materials Research Society, 1107, 519-526.

Anderson, B.E. *(former name)*, Helean, K., Bryan, C.R., Brady, P.V., and Ewing, R.C. (2007) Perrhenate and pertechnetate Behavior on iron and sulfur-bearing compounds. Scientific Basis for Nuclear Waste Management XXX, Proceedings of the Materials Research Society, 985, 425-430. **(Appendix B)**

1.2c. Presentations

Ferriss, E. D. A., Helean, K. B., Bryan, C. R., Brady, P. V., and Ewing, R. C. (2008) UO_2 corrosion in an iron waste package. Spent Fuel Workshop, May 7-8, 2009, Toronto, Canada.

Ferriss, E. D. A., Helean, K. B., Bryan, C. R., Brady, P. V., and Ewing, R. C. (2008) UO_2 corrosion in an iron waste package, Material Research Society Fall Meeting, Dec. 1-5, 2008, Boston, MA

Anderson, B. E. *(former name)*, Helean, K. B., Bryan, C. R., Brady, P. V., and Ewing, R. C. (2007) Waste package corrosion studies using small mockup experiments, Material Research Society Scientific Basis for Nuclear Waste Management XXXI, Sept. 16-21, 2007, Sheffield, England. (Best Student Talk)

Anderson, B.E. *(former name)*, Essene, E.J., and Becker, U. (2007) Ti substitution in zircon. Geochimica Et Cosmochimica Acta, 71(15), A27. 17^{th} Annual V.M. Goldschmidt Conference, August 19-24, 2007, Cologne, Germany.

Anderson, B. E. *(former name)*, Becker, U., Helean, K. B., Ewing , R.C. (2006) Perrhenate and pertechnetate behavior on iron and sulfur-bearing compounds, Material Research Society Fall meeting, Nov. 27-Dec. 1, 2006, Boston, MA.

Anderson, B. E. *(former name)*, Skomurski, Shuller, Ewing, Becker, Computational investigations of UO_2 oxidation and of TcO_4^- (UO_2^{2+}, and NpO_2^+) adsorption on sulfides, Surface Reactivity in Minerals Workshop, April 10-11, 2006, Gargnano, Italy.

CHAPTER 2.

UO_2 CORROSION IN AN IRON WASTE PACKAGE

2.1. Abstract

In order to investigate the interactions between spent nuclear fuel, corroding iron waste packages, and water under conditions likely to be relevant at the proposed repository at Yucca Mountain, six small-scale waste packages were constructed. Each package differed with respect to water input, exposure to the atmosphere, and temperature. Two of the packages contained 0.1 g UO_2. Simulated Yucca Mountain process water (YMPW) was injected into five of the packages at a rate of 200 μL per day for up to two years, at which point the solids were characterized with X-ray powder diffraction, scanning electron microscopy, wet chemistry, and electron microprobe analysis. Fe(II) is abundant in the corrosion products that form, and the dominant crystalline product in all cases according to X-ray diffraction is magnetite or the structurally similar maghemite. Minor phases included akaganeite (β-FeOOH) and possibly also hematite (Fe_2O_3), lepidocrocite (γ-FeOOH), and green rust ($Fe(II)_{1-x}Fe(III)_x(OH)_2Y_{x/n}$). Under these conditions, UO_2 is expected to alter to the uranyl silicate uranophane ($Ca[(UO_2)SiO_3(OH)]_2 \cdot 5H_2O$). Neither oxidation of the UO_2 nor any oxidized (uranyl) solid was observed, suggesting that conditions were sufficiently reducing to kinetically hinder U(IV) oxidation.

2.2. Introduction

Corrosion of iron metal in an enclosed environment is an important phenomenon in both preserving and understanding archeological sites containing iron artifacts (e.g. Gerwin and Baumhauer, 2000) and in nuclear waste disposal scenarios, such as those proposed by the United States and Spain, involving a waste package composed primarily of steel. The focus of this paper is the nature of corrosion products of steel waste packages planned for use at the proposed nuclear waste repository at Yucca Mountain, the local redox and pH conditions inside these waste packages, and the resulting uranium mineralogy and mobility.

Steel and steel corrosion products may play an important role in limiting radionuclide release (Gu et al., 1998; Dodge et al., 2002; Eng et al., 2003). Uranyl ions (UO_2^{2+}), typical products of the oxidative dissolution of spent nuclear fuel (SNF), may be sorbed by a variety of Fe-bearing minerals including hematite (Fe_2O_3) (Ho and Miller, 1986), lepidocrocite (γ-FeOOH) (Moyes et al., 2000), and goethite (α-FeOOH) (Moyes et al., 2000; Sherman et al., 2008) and perhaps also reduced to a less labile form by magnetite (Fe_3O_4) (Grambow et al., 1996; Dunn et al., 2000; Dodge et al., 2002; Missana et al., 2003; Scott et al., 2005; Rovira et al., 2007; Duro et al., 2008) and green rust ($Fe(II)_{1-x}Fe(III)_x(OH)_2Y_{x/n}$) (O'Loughlin et al., 2003). Aqueous Fe(II) and steel corrosion products may also immobilize other radionuclide species such as TcO_4^- (Cui and Eriksen, 1996; Pepper et al., 2003; Zachara et al., 2007), I^- (Fuhrmann et al., 1998), and NpO_2^+ (Teterin et al., 2006).

Corroding steel inside of these waste packages may also influence the redox potential (Eh or pe) and pH, two variables that will strongly influence the degradation

behavior of the spent nuclear fuel and the subsequent mobility of radionuclides. Current conceptual models (SNL, 2007d) assume that once the waste package has been breached, the inside of the package will be flooded with oxygenated water and highly oxidizing air. This situation is unfavorable because oxidizing conditions typically lead to the formation of potentially mobile ions such as TcO_4^-, NpO_2^+, and UO_2^{2+}. The availability of electrons from corroding steel may be an important factor in establishing and maintaining overall reducing conditions. Although the measured system Eh is typically not useful for quantitative predictions (Morris and Stumm, 1967; Jenne, 1981; Hostettler, 1984; Lindberg and Runnells, 1984; Stefansson et al., 2005), an overall decrease in redox potential may, depending on water chemistry, stabilize spent nuclear fuel (SNF), kinetically hinder SNF oxidation, or influence the nature of any SNF alteration products.

2.3. Methods

2.3a. Miniature steel waste packages

Six small-scale (~1:40 by length) miniature waste packages were constructed using 316 stainless steel (nominal composition: $Fe_{62.0}Cr_{18.0}Ni_{14.0}Mo_{3.0}Mn_{2.0}N_{0.08}Si_{0.75}P_{0.045}S_{0.03}C_{0.02}$ (ASTM, 2002)), the same material as the proposed Yucca Mountain waste packages (SNL, 2007d), for the body, end-caps, and fittings (Figure 2.1). This steel corrodes less rapidly under most conditions than the A-516 carbon steel (nominal composition: $Fe_{97.87}C_{0.31}Mn_{1.3}P_{0.035}S_{0.035}Si_{0.45}$ (ASTM, 2005)) proposed for use as guides for spent nuclear fuel inside the waste packages. The A-516 steel and 316 stainless steel were obtained from Laboratory Testing, Inc., a DOE-approved supplier, and are certified to

meet the ASTM standards for those materials. Electron microprobe analysis showed that the A-516 steel also contained 0.19 wt % Cr and 0.29 wt % Cu.

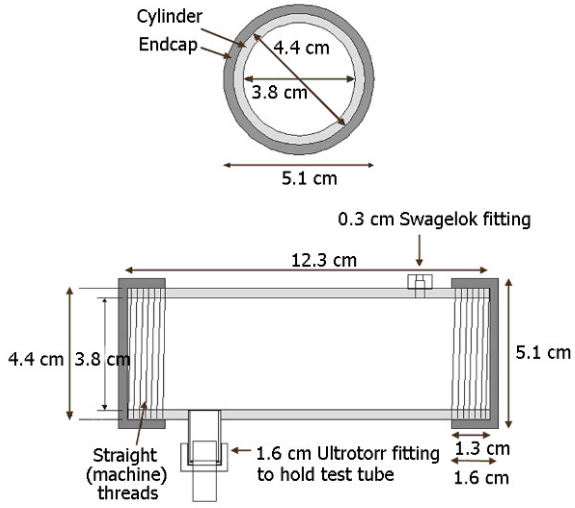

Figure 2.1. Schematic of miniature waste package viewed from two angles

In order to maintain the same ratio of body-interior surface area to guide surface area, 25 1 x 10 x 0.1 cm strips of A-516 carbon steel (mass 7.9g each) were inserted into each waste package, and inert polytetrafluoroethylene (PTFE) balls with a diameter of 9.53 mm were used to separate the steel strips and fill some of the excess void space. Each package had an internal diameter of 38.1 mm, an internal length of 123 mm, two upper ports (diameter 0.32 mm) and one lower port (diameter 16.0 mm) with an Ultra-torr® fitting and a heavy-gauge glass test tube for effluent sample collection. The caps on both ends of each package were sealed using Viton® O-rings and parafilm to prevent higher corrosion rates on the straight-threaded end-caps.

The six packages differed with respect to water input, exposure to the atmosphere, temperature, and the presence of uranium (

Table 2.1). In most cases, the upper port on the opposite side from the lower port was covered by a rubber septum for the introduction of the aqueous phase. The exception was package C, which was not injected with water but was left entirely open to an atmosphere with near 100% relative humidity and partial pressures of oxygen and carbon dioxide of $10^{-0.7}$ bar and $10^{-3.4}$ bar, respectively. The second upper ports of packages A, D, and E were sealed using a Swagelok snubber, which limits airflow but allows sufficient exchange to avoid pressurization, whereas those of packages B and F were left open to the same atmospheric conditions as that of package C. No effort was made to seal the edges around the rubber septum in the upper port. Because of their increased exposure to the atmosphere, the "open" packages B, C, and F were more likely to simulate conditions for a breached waste package at Yucca Mountain. Humid conditions were maintained by enclosing the package setup in a sealed plastic bag and pumping air, which had been saturated with water vapor by bubbling deionized water through the bag. A Traceable® digital hygrometer was used to check these conditions. Package D was maintained at 60°C using a hot plate, and all other packages were allowed to corrode at room temperature. Package D is significantly different from the other three packages because it was initiated as a preliminary study, a short test to determine if the steel would corrode quickly under the chosen conditions. Ideally, other packages would be run at elevated temperatures and high relative humidity in order to better gauge the effect of changing these variables.

Table 2.1. Test matrix for waste package experiments.

Package	Atmosphere	YMPW Volume	Temp. (°C)	Relative Humidity	UO_2 present
A	Closed	200 µl/day (~ 50 mL total)	25	100%	none
B	Open	200 µl/day (~ 50 mL total)	25	100%	none
C	Open	-	25	100%	none
D	Closed	1 mL/week YMPW-2	60	environmental	none
E	Closed	200 µl/day – (~ 25 mL total)	25	100%	0.1 g
F	Open	200 µl/day – (~30 mL total)	25	100%	0.1 g

The uranium in packages E and F was present as synthetic UO_2 prepared from large crystal boules grown from an arc-fusion melt (Weber, 1981) (Figure 2.2). The mineral uraninite (naturally occurring UO_2) is considered an excellent analogue for commercial SNF, having the same structure, dominant composition, and similar abundant impurities (Janeczek et al., 1996). Although a less appropriate analogue for SNF than uraninite because of a lack of impurities, synthetic UO_2 was preferred in this study both in order to simplify the system and to minimize radiation levels associated with decay products such as radon. A small mass (0.1 g) was used in order to further minimize associated radiation, and the UO_2 was crushed using a mortar and pestle, creating sand and silt-sized grains (0.005 – 2 mm in diameter) to increase available surface area.

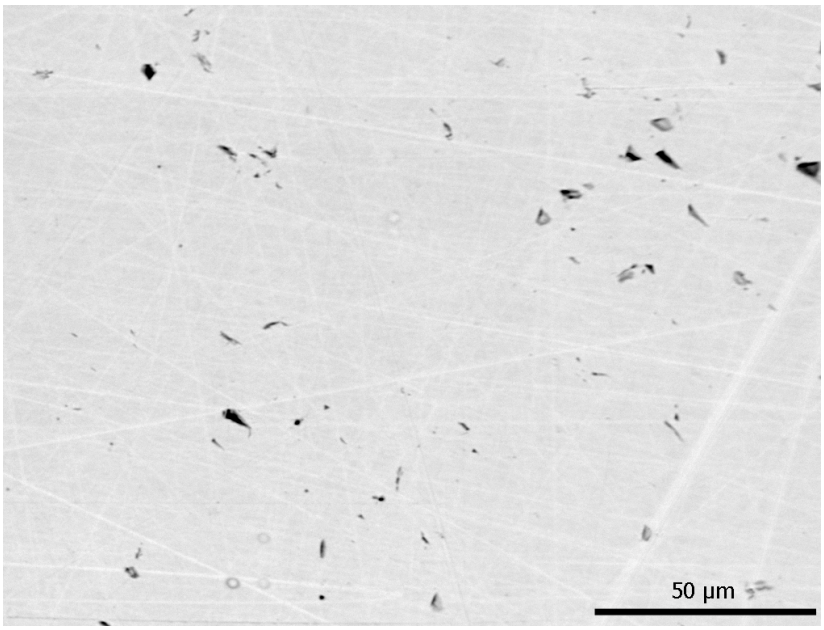

Figure 2.2 Secondary electron image of polished cross-section of UO_2 grain prior to crushing for use in miniature waste packages. SEM/EDS of all areas showed only U and O.

2.3b. Yucca Mountain process water

A simulated Yucca Mountain process water (YMPW) was injected into packages A, B, E, and F at a rate of 200 µL per day five days a week using a calibrated needle syringe. Scaling by volume, this rate is equivalent to the introduction of 1.3 mL of water per minute in a full-size waste package. YMPW consists of 50 mg/L silica, 38.3 mg/L Na, enough hydrochloric acid to lower the pH to 7.6, and an excess of powdered calcite. The solution was equilibrated with the atmosphere for 5 days, filtered, and allowed to equilibrate with the atmosphere for an additional 5 days. The final pH for different batches stabilized between 7.5 and 7.9. J-13 well water (Harrar et al., 1990; Langmuir, 1996), pore waters from the unsaturated zone near Yucca Mountain (SNL, 2007b), and various calculated waters have been used to approximate the composition of fluids entering a breached waste package. However, there is no universally accepted optimal fluid composition for use in studies

of the release of radionuclides at a proposed nuclear waste repository (source term work) because of large uncertainties in, for example, breach time, fluid sources, and the extent of prior fluid-rock interactions. The waters currently found at at Yucca Mountain are typically highly supersaturated with respect to quartz and approximately saturated with respect to calcite (SNL, 2007b), and the major element chemistry of YMPW is similar to these waters (Table 2.2). Another fluid, YMPW-2, a pH 7.9 dilute Na-Ca-HCO_3- silicate water with approximately 0.8 ppm chloride and 1.0 ppm fluoride, was injected into package D at a rate of 1 mL per week.

Table 2.2. Saturated zone (J-13) (Harrar et al., 1990) and selected pore water compositions (SNL, 2007) compared with initial concentrations in YMPW and YMPW-2.

Component	unit	J-13	Ca pore water	Na pore water	YMPW [a]	YMPW-2
pH [b]	pH	7.4 (7.8)	7.6 (8.1)	7.4 (8.3)	7.8	7.9
$SiO_{2(aq)}$	mmolar	0.95	0.66	0.66	0.83	0.90
HCO_3^-	mmolar	2.34	6.51	5.93	0.45	1.95
Cl^-	mmolar	0.20	0.59	0.68	1.00	0.02
Na^+	mmolar	1.99	1.70	5.22	1.66	2.00
Ca^{2+}	mmolar	0.32	2.35	2.02	5.02	0.87

[a] All but pH are calculated values given known Na and Si inputs, atmospheric carbon dioxide levels and calcite equilibria. Actual values produced may vary slightly.
[b] Values given in parentheses assume for J-13 and pore waters assume the solution is equilibrated to log fCO_2 = -3.0
[c] HCO_3^- was used for charge balance in the calculating J-13 composition.

2.3c. Characterization of solids

Non-radioactive packages were handled primarily at Sandia National Laboratories (SNL), and the U-bearing package (E and F) work was done at the University of Michigan (UM). The surfaces of the A-516 steel and UO_2 were examined using scanning electron microscopy with energy dispersive spectroscopy

(SEM/EDS; Hitachi S3200N at UM; JEOL JSM-5900LV at SNL) prior to being placed in the packages. Packages A, B, E, and F were allowed to corrode at room temperature and 100% relative humidity until the test tubes in the lower port were nearly full of effluent. Package C was opened at the same time as packages A and B, and package D was sampled at 30 and 90 days. During sampling, the packages were disassembled under inert atmosphere (N_2-filled glove bag at SNL; Coy Laboratories glove box containing a mixture of N_2 and 5% H_2 gas, a catalyst for O_2 combination with H_2, and a desiccant at UM).

Characterization of corrosion products included powder X-ray powder diffraction (XRD, Scintag X1 at UM and Bruker D8-ADVANCE at SNL, Cu Kα radiation), SEM/EDS, electron microprobe analysis (Cameca SX100) with wavelength dispersive spectroscopy (EMPA/WDS), and wet chemical analysis. XRD samples from packages A, B, and D were prepared as smear mounts and analyzed within two hours after the packages were opened. Due to a catastrophic XRD failure at SNL, the original XRD data for package D was lost except for a graphical image, and the samples were analyzed again 3.5 years later at UM. Corrosion products from the U-containing packages E and F were scraped onto a glass slide with a plastic scraper and allowed to dry under inert atmosphere for two hours prior to being analyzed. Strips from packages E and F with relatively high levels of corrosion but low levels of radioactivity were cross-sectioned, given a diamond polish, and examined with SEM/EDS and EMPA/WDS. SEM analyses were conducted at an accelerating voltage of 20 kV, and EMPA/WDS analyses used 25 kV and a beam current of 40 nA and typical counting times of 30 s, except for U Lα, which was run

at 50 nA and 300 sec to obtain comparable precision to U Mα. The standards used for the calibration were: UO_2 for U Mβ (count time 200 s) and U Lα (count time 300 s); Cu metal for Cu; manganotantalite ($MnTa_2O_6$)for Mn; and andradite ($Ca_3Fe_2(SiO_4)_3$) for Fe and Si.

Fe(II)/Fe(III) ratios in the corrosion products were measured using a method combining the standard Pratt and ferrozine wet chemical methods (Pratt, 1984; Stookey, 1970). The samples were dissolved in H_2SO_4 and HF rather than HCl (Anastácio et al., 2008), and the resulting solution was analyzed using the spectrophotometric agent ferrozine. Two potential weaknesses of all wet chemical methods are: 1) a very small sample analyzed may not be representative of the whole, and 2) the Fe(II) can be easily oxidized during sample digestion. In this study, as in the traditional Pratt method, oxidation was prevented by immediate and continuous boiling of the acid mixture during digestion. Given the likelihood of oxidation, the numbers reported for all Fe(II)/Fe(III) ratios are *minimum* values.

2.3d. Water chemistry

Total U and Fe were measured in the effluent of packages E and F using inductively-coupled mass spectrometry (ICP-MS, Thermo Fisher Finnigan Mat Element at UM). Effluent pH was analyzed using a Ross electrode with a Symphony SB70P meter, and Fe(II)/Fe(III) values were measured using the ferrozine method (Stookey, 1970). These values, along with initial YMPW water chemistry, were used as input in the software package EQ3NR (Wolery and Jarek, 2002) to calculate speciation, solution-mineral equilibria, pe, and oxygen fugacities using a thermodynamic database developed specifically for application to the Yucca

Mountain Project (SNL, 2007c). The major assumptions that went into these calculations were: 1) the concentrations of elements other than Fe (Table 2.2) remained constant throughout the experiment, 2) K^+ and Al^{3+} are also present due to the groundwater interaction with the surrounding tuff at Yucca Mountain, and 3) all aqueous and gas phases have reached thermodynamic equilibrium. Assumption three is rarely correct in natural waters (Morris and Stumm, 1967; Jenne, 1981; Hostettler, 1984; Lindberg and Runnells, 1984; Stefansson et al., 2005) and is almost certainly incorrect here. Aqueous Fe(II)/Fe(III) ratios may have been controlled primarily by the rates of Fe corrosion, precipitation, and sorption, and the calculated oxygen fugacities and pe's determined and reported here based on the Fe(II)/Fe(III) redox couple should be considered only estimates of a theoretical system pe (pe is defined as –log[activity of electrons]) that may bear little resemblance to the actual potential of the U(IV)/U(VI) couple.

2.4. Results

2.4a. Fe speciation and pe-pH conditions

Figure 2.3 shows the pe-pH conditions inside of the packages determined from the measured pH and Fe(II)/Fe(III) ratio in the effluent (Table 2.3) and superimposed on the pe-pH diagrams for aqueous Fe species in YMPW. Over time, the internal chemistry becomes both more basic and more reducing as the steel corrodes, releasing more electrons from the iron. The open packages are more oxidizing than similar closed packages. Aqueous species were chosen for the pe-pH diagram based on the results of EQ3NR speciation calculations (Table 2.4). Calculated aqueous Fe species include $HFeO_{2(aq)}$, FeO_2^-, Fe^{2+}, $HFeO_2^-$, and $FeOH^+$,

and in most packages, $FeCO_{3(aq)}$ is the dominant Fe species in the packages after 1.5 years. Siderite ($FeCO_{3(s)}$) has extremely sluggish precipitation kinetics (Jensen et al., 2002) and was not observed.

Table 2.3. Measured solid corrosion product Fe(II)/Fe(III) ratios, effluent Fe(II) and Fe(III) values[a] , and pH, as well as pe and log oxygen fugacity (fO_2) calculated using the geochemical modeling tool EQ3NR.

Package	Sample Time	Solids[b] Fe(II)/Fe(III)	$[Fe(II)_{(aq)}]$ (μg/L)	$[Fe(III)_{(aq)}]$ (μg/L)	pH	pe	log fO_2
A (closed)	1.5 years	0.72	11	3.1	8.9	-1.4	-53.0
B (open)	1.5 years	0.60 (± 0.05)	6.4 (± 3.6)	60. (± 6)	8.7	0.63	-45.6
B	0.5 years	ND[c]	38 (± 2)	58 (± 2)	6.6	5.21	-35.7
D (heated)	90 days	0.04	ND	ND	ND	ND	ND
E (Uclosed)	2 years	0.90 (± 0.3)	88	77	10.2	-4.39	-59.7
F (Uopen)	2 years	1.5 (± 0.4)	62	70	9.5	-2.16	-53.7

[a]When enough material for multiple samples was available, error estimates were made.
[b]These are minimum values in all cases. Because of a delay in transferring the sample during preparations for titration, package D is particularly likely to have experienced oxidation.
[c]ND stands for 'not determined'.

Table 2.4. Activity (mM) of aqueous Fe species in packages calculated by EQ3NR.

species	A	B 0.5 year	B 1.5 year	E (U-closed)	F
$HFeO_{2(aq)}$	5.04E-07	7.85E-06	1.05E-05	2.77E-06	7.67E-06
FeO_2^-	1.17E-07	negligible	1.54E-06	1.29E-05	6.59E-06
FeO^+	negligible	5.48E-06	negligible	negligible	negligible
$FeCO_{3(aq)}$	1.45E-06	1.79E-07	8.04E-07	8.53E-06	8.61E-06
Fe^{2+}	3.61E-07	1.22E-05	3.09E-07	2.77E-07	6.76E-07
$HFeO_2^-$	negligible	negligible	negligible	4.77E-06	negligible
$FeOH^+$	1.01E-07	negligible	5.43E-08	1.51E-06	7.02E-07

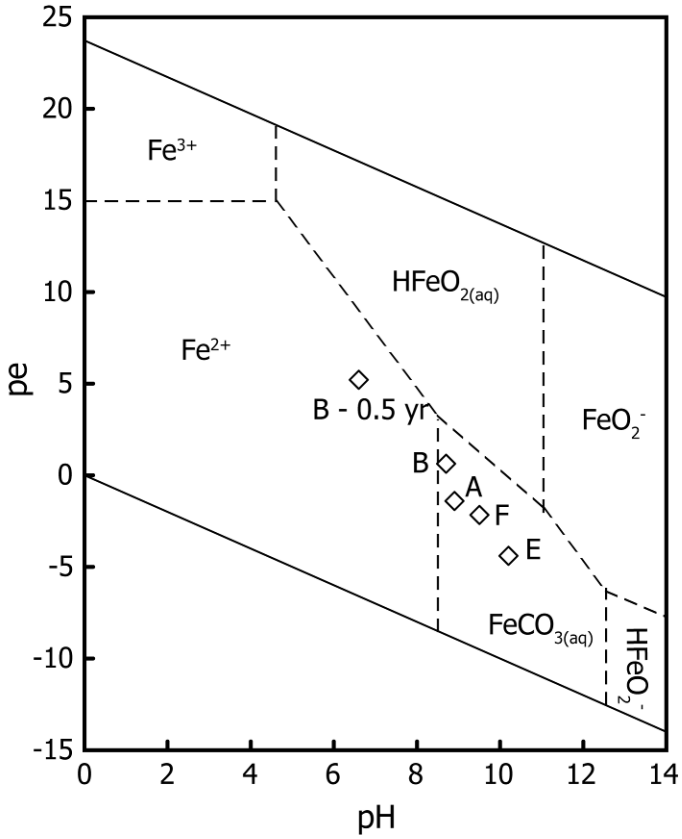

Figure 2.3 pe-pH diagrams showing package chemistry (letters explained in Table 2.3) and dominant aqueous Fe phases in YMPW.

2.4b. Metal corrosion products

The extent of metal corrosion varied from virtually nothing, most notably in package C, which was not injected with water, to up to 50% on some strips. Typically 5% or less of an individual strip appeared corroded. EDS analysis showed a major chemistry of Fe or Fe-O in all areas, but Cu, S, Si, and Mn were also noted in corrosion products. EMPA/WDS results of the corrosion products also show a high level of heterogeneity (Figure 2.4). This variability in chemistry suggests that solid samples taken for XRD (a few tens of mg) and wet chemical analyses (about 5 mg) may not be representative. To minimize this problem, multiple analyses were performed when a sufficient mass of corrosion products was available.

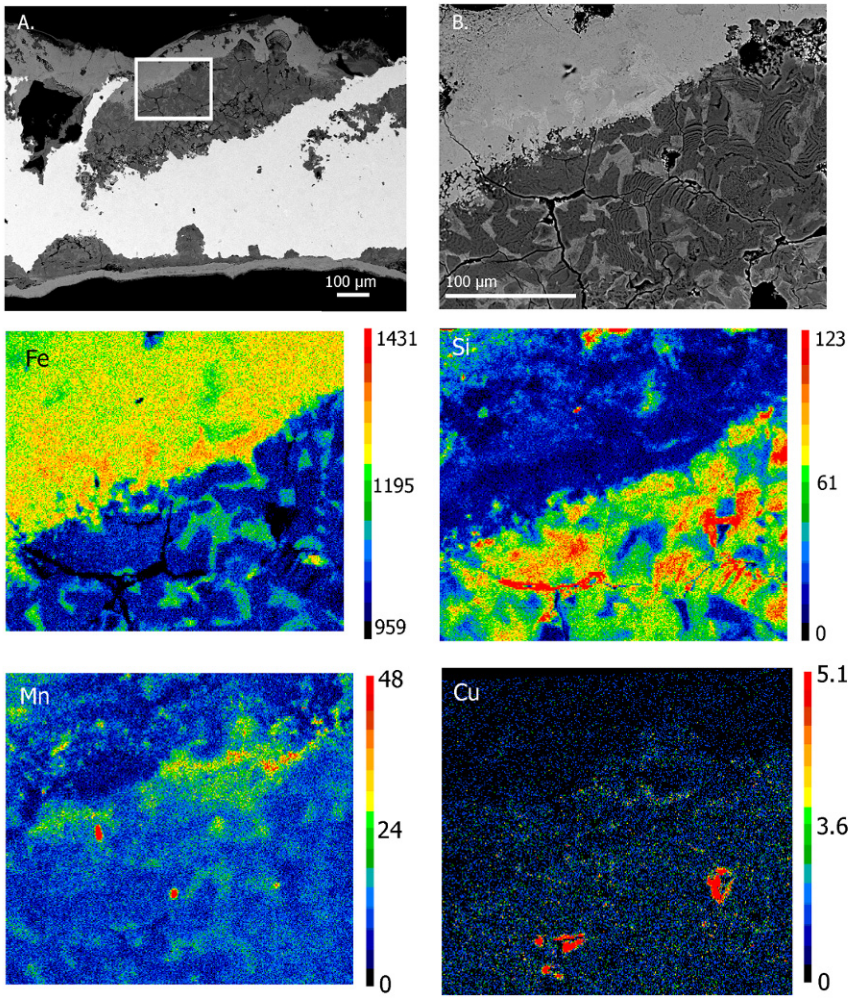

Figure 2.4. BSE images of corroded steel from package E showing iron corrosion products. Bright areas in A are largely uncorroded steel, and the darker phases consist of Fe oxides, most likely magnetite. The boxed area of A is shown magnified in B. Electron microprobe analysis with WDS was used to create elemental maps of the boxed area in B. These are shown labeled by element. Map scale bars show total counts per pixel.

The major corrosion product identified by XRD in packages A, B, D, E, and F was either magnetite, Fe_3O_4, or the structurally similar maghemite, γ-Fe_2O_3 (Figure 2.5). Wet chemical analyses of corrosion products from all of the packages (Table 2.3) confirmed the presence of Fe(II), which suggests the dominant corrosion product is magnetite rather than maghemite. However, given that the Fe(II)/Fe(III) ratio in the

bulk solids is greater than that of magnetite (0.5) at least one other reduced Fe phase must be present, or the magnetite has significant maghemite solid solution (Xu et al., 1997). Because no other significant peaks appeared in the XRD spectra, a second phase is probably amorphous. It is also possible that maghemite is the dominant corrosion product, and all of the Fe(II) was present in poorly crystalline phases.

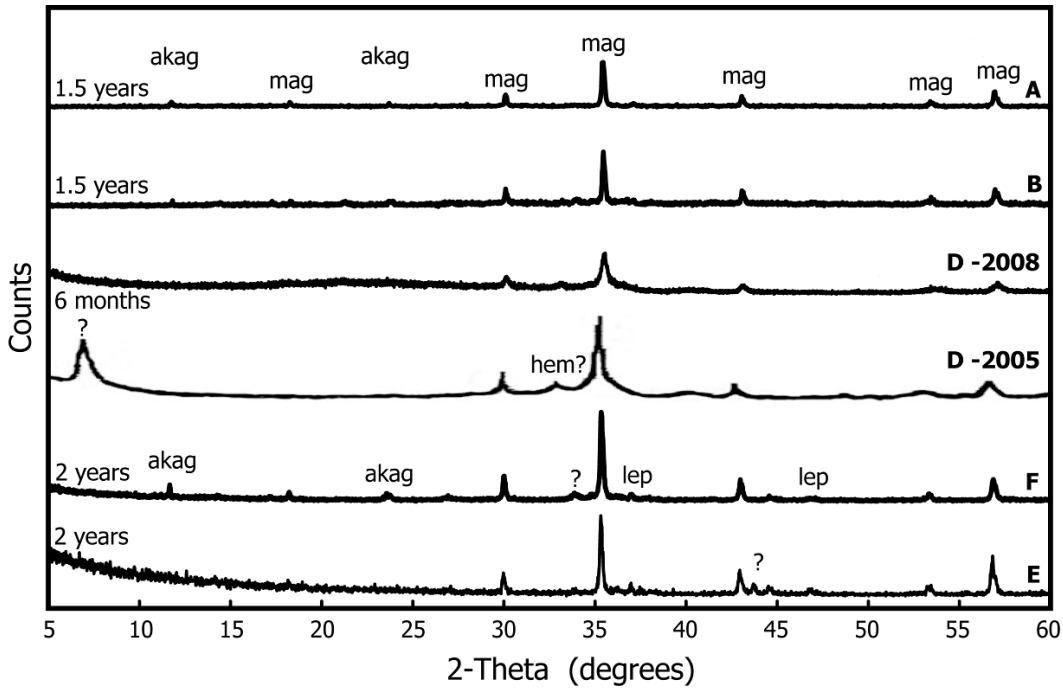

Figure 2.5. X-ray diffraction spectra (Cu Kα radiation) of corrosion products in packages A, B, D, F, and E showing magnetite/maghemite (mag), hematite (hem), akaganeite (akag), lepidocrocite (lep), and an unidentified mineral (?). All patterns were obtained within six hours of opening the packages except D-2008, which was obtained 3.5 years after the initial analysis. The original data for the high temperature study (D-2005) has been lost, and all peak positions for that pattern should be treated as approximate values.

The XRD data suggest the presence akaganeite in packages A, B, and F. Akaganeite is nominally β-FeOOH but is perhaps better described as $\beta\text{-}FeO_{1-2x}(OH)_{1+x}Cl_x$ because Cl^- or F^- ions are typically present (Remazeilles and Refait, 2008). Formation of akaganeite is associated with corrosion processes induced by Cl^- ions (Stahl et al., 2003). Small lepidocrocite (γ-FeOOH) peaks were observed in

packages E and F after two years, and one peak suggesting the presence of hematite (Fe_2O_3) was observed in package D after 90 days. An unidentified phase with a large *d*-spacing of 13 Å was noted in the initial survey of package D, the high temperature study. This mineral may correlate with a platy Fe-O-Cl phase that was noted using SEM/EDS (Figure 2.6). The layered structure, high Fe(II) to Fe(III) ratio, Cl content, and evidence of lepidocrocite formation in packages E and F suggest the presence of the layered Fe-oxyhydrate green rust (Schwertmann and Fechter, 1994), which has also been noted as a corrosion product of reactive barriers made of iron metal (Roh et al., 2000).

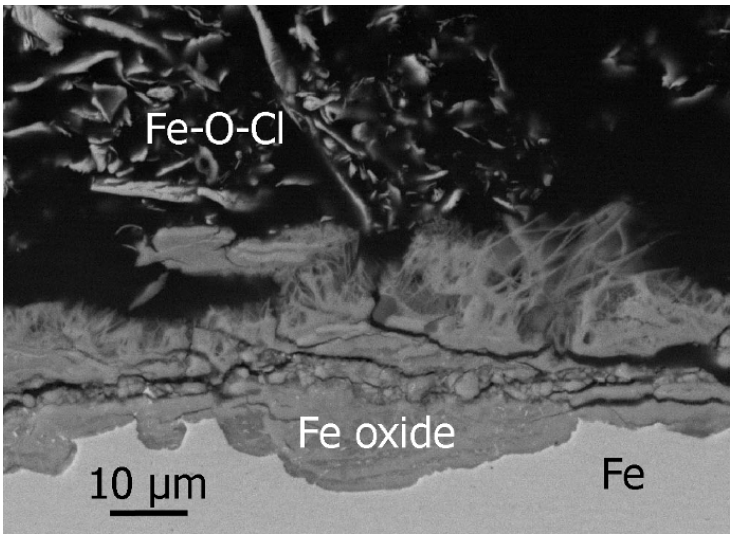

Figure 2.6. Back-scattered electron micrographs of Package D corroded steel of at 90 days. The polished cross-section shows oxidized areas along the steel surface and loosely consolidated fibers or plates of a Cl-rich phase.

The results of this study are in general agreement with previous studies of Fe and steel corrosion, in which magnetite is typically the dominant phase. Maghemite, goethite, lepidocrocite, hematite, siderite, and green rust may also be present, depending on experimental conditions, such as relative humidity, water chemistry,

steel composition, time, and temperature (Kassim et al., 1982; Leidheiser and Music, 1982; Ohtsuka et al., 1986; Oh et al., 1998; Kim, 1999; Legrand et al., 2000; Dunn et al., 2000; Maslar et al., 2000; Savoye et al., 2001; McMillian et al., 2002; Janot and Guerard, 2002; Garcia et al., 2003; Cheng and Steward, 2004; Music et al., 2004; Ben Lagha et al., 2007). Bench-top experiments, even those such as the current study that were run over a series of years, are short-term compared to the life of a repository. Corrosion studies of archeological artifacts suggest that magnetite, goethite and maghemite are the most important long-term corrosion products, although akaganeite, lepidocrocite, and siderite have also been found as corrosion products of iron artifacts in certain environments. Unfortunately, those studies are not sufficiently well developed to be useful for quantitative long-term corrosion modeling (Murphy et al., 1998; Neff et al., 2005).

Under anoxic conditions, the reduction of H^+ becomes important (Callister, 2003), and the corrosion of Fe is typically thought of as a transformation first to $Fe(OH)_2$ followed by oxidation to magnetite via the Schikorr reaction (Schikorr, 1933):

$$3Fe(OH)_2 \rightarrow Fe_3O_4 + H_2 + 2H_2O \qquad (2.1)$$

Given the very low redox potentials, some hydrogen of may have accumulated, but the lack of XRD evidence for $Fe(OH)_2$ formation suggests that the Schikorr reaction was of minor importance.

Copper, which was observed to be a minor constituent of the original A-516 steel strips used in this study, migrated out of the steel during corrosion and formed distinctive small balls highly enriched in Cu (Figure 2.7). While the Cu balls are very

common in the cracks and crevices throughout the corroded steel, they do not appear to be interacting with the U directly. The potential effects of Cu and other minor components in the steel on the corrosion of UO_2 under these conditions were not evaluated.

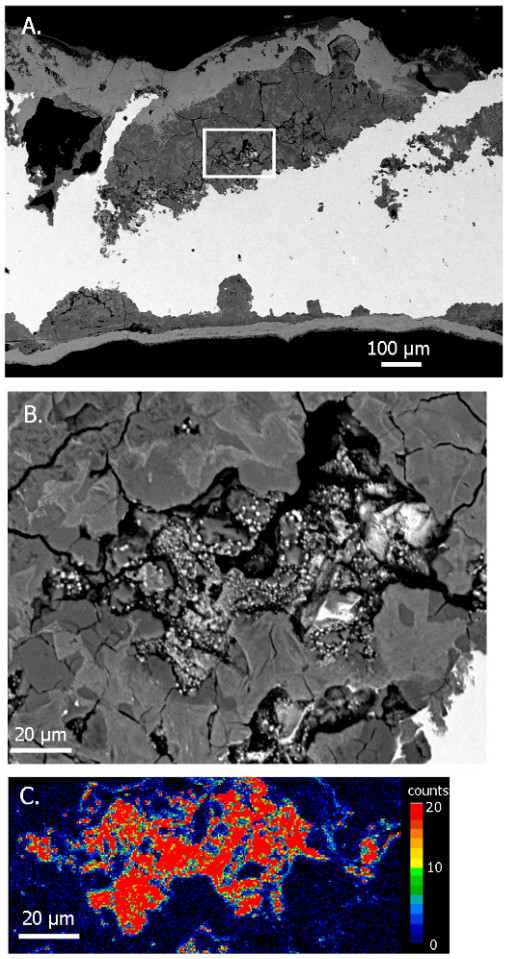

Figure 2.7. Back-scattered electron images of a steel strip cross-sections from package E. The bright phases in the boxed area of A are shown magnified in B. Electron microprobe analysis was used to generate an elemental map of Cu, shown in C. Elemental map scale bar shows total counts per pixel.

2.4c. Corrosion of UO_2

Several particles containing U and O were found with SEM/EDS associated with the corrosion products. Most of these were only a few μm wide (Figure 2.8), although one 20 μm-wide grain was located. Because of the small size of the grain, microscale characterization, for instance with transmission electron microscopy, could not be carried out, but elemental maps and line scans were generated around the grain using EMPA/WDS (Figure 2.9). Measured UO_2 for points on the uraninite were close to 100 wt %. Areas with lower measured wt % UO2 also showed low total measured wt %. These pores on the surface of the grain are similar to those observed in original grains (Figure 2.2), although they may have increased in size during the polishing process. The broken areas of the grain along an otherwise sharp boundary may also be a result of polishing.

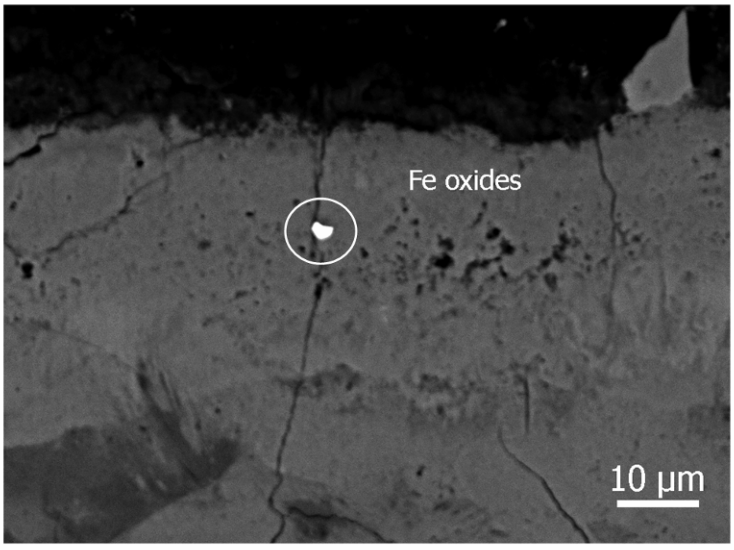

Figure 2.8. Back-scattered electron image of a typical small UO_2 fragment (circled and identified by EDS) found in the package E after two years. No other solid uranium phases were detected using SEM/EDS, XRD, or EMPA.

Weight percentages of 0.3% - 0.1% UO_2 were observed with EMPA/WDS up to 15 μm from the grain. These results may have been caused by 1) secondary fluorescence of the U in the grain by Fe, 2) the remainder of the UO_2 grain buried just below the surface, 3) poor resolution of spot size during EMPA measurements, 4) migration of U from the grain and association with iron corrosion products , or 5) the higher topographic relief of the UO_2 relative to the much softer Fe oxide matrix. If the U Mβ lines were being fluoresced by Fe, the weight percent U measured using Mβ lines should be higher than weight percent U measured using Lα lines. A comparison of quantitative results for U Lα (25 kV, 50 nA, 300s count time) and Mβ lines (20 kV, 20 nA, 20 s count time) indicates that this is not the case (Figure 2.10), and therefore secondary fluorescence is not an important phenomenon in this system. The similarities in line scans on two different sides of the grain and fairly sharp grain boundary suggest that either the buried grain is highly symmetrical or counts from buried UO_2 are negligible. Because the grain may not be well anchored in the corrosion products, the sample was not polished additionally for a definitive test. The spot size could not be determined without modeling software or comparison to a similar sample known to have a very sharp grain boundary. If EMPA/WDS measurements do correctly indicate the presence of U surrounding the original grain, the U may be present as 1) a very small grains of a reprecipitated uranium mineral such as UO_2, as was observed in a recent study with iron nanoparticles (Riba et al., 2008), 2) uranyl ions absorbing to magnetite or other iron oxide surfaces, or 3) part of a poorly crystalline phase.

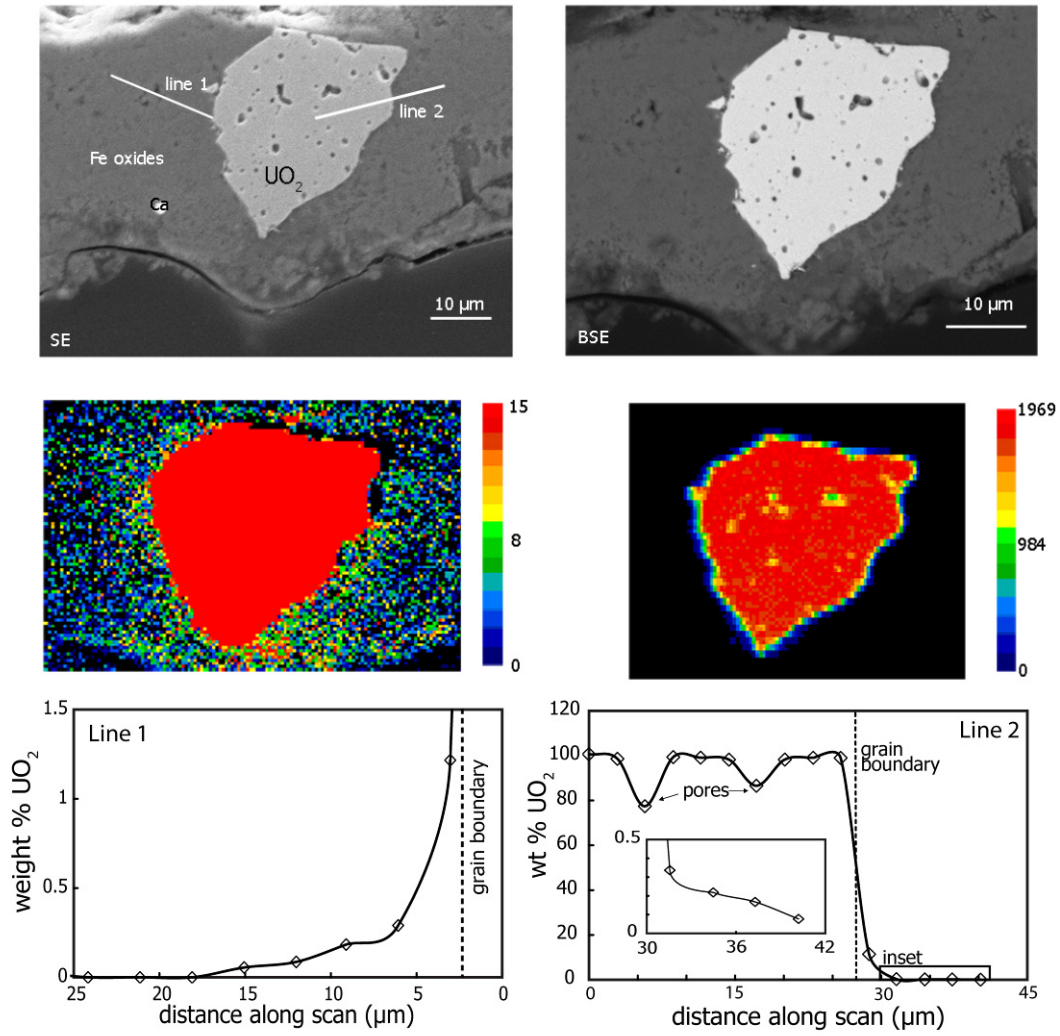

Figure 2.9. Secondary electron (SE) and back-scattered electron (BSE) image of UO_2 grain surrounded by steel corrosion products (most likely magnetite) in package E with associated EMPA/WDS line scans and elemental maps of U focused at different levels of total counts per pixel.

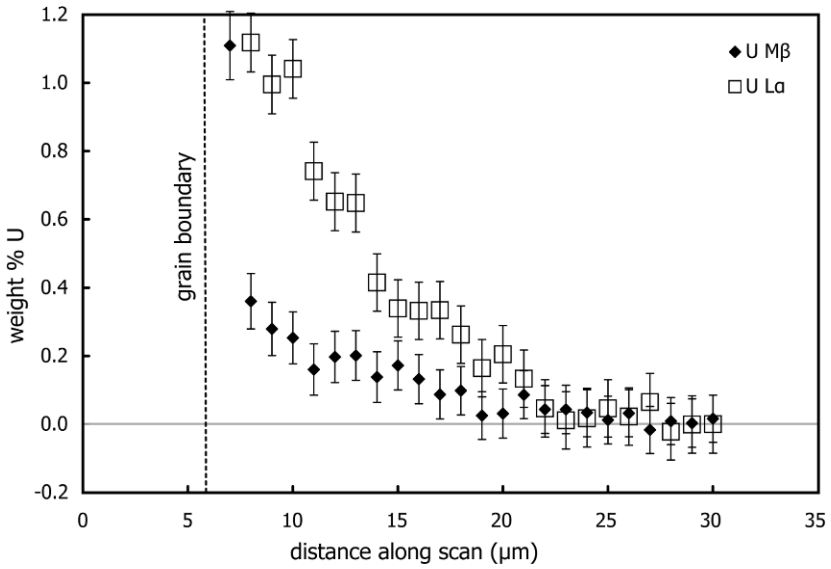

Figure 2.10. EMPA/WDS line scans of U Lα and Mβ taken near line 1 of the UO_2 grain shown in Figure 2.9. Vertical error bars represent one standard deviation in the measured weight % U.

Although the exact nature of the U-Fe association cannot be made clear without more detailed nanoscale analysis such as with transmission electron microscopy (which cannot be applied due to the small size of the sample), the low values of U associated with the iron corrosion products, generally sharp appearance of the boundary between the grain and surrounding corrosion products, and low concentration of dissolved U in the water (0.868 ppb in package E and 4.536 ppb in package F) strongly suggest that overall UO_2 corrosion was minimal.

2.5. Discussion

2.5a. Lowered redox conditions

The heterogeneity of the corrosion products and presence of uncorroded steel demonstrates that even after two years, the solids are far from thermodynamic equilibrium. The pe-pH conditions for all packages plot in the hematite, not magnetite, stability field (Figure 2.11). Therefore, calculated pe conditions, which are

based on only the aqueous Fe(II)/Fe(III) ratio without regard to the possible influence of solid iron phases, should be taken as estimates.

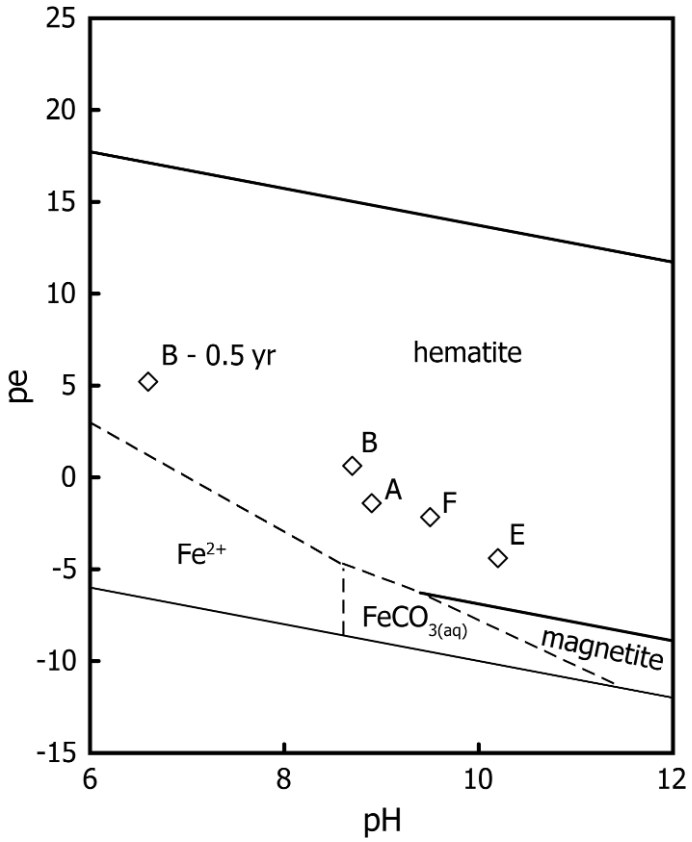

Figure 2.11. Close-up of measured redox and pH conditions inside of the packages (letters explained in Table 2.3) superimposed on the field of iron minerals expected to be most thermodynamically stable in YMPW. The activity of Fe is taken as 1.7 x 10^{-6} M, an average measured value.

The high Fe(II)/Fe(III) ratios in the package effluent (assuming Fe redox chemistry dominates the system) and negligible UO_2 corrosion suggest that the internal chemistry of the packages is much more reducing than the outside air. This is likely due to a combination of low oxygen transport rates into the packages relative to Fe and U oxidation reactions (which remove oxygen from the system through the formation of magnetite and other oxides or oxyhydroxides) and the presence of a

buffering system that resists the Eh change that would be expected when oxygen enters the system.

Although the packages were filled with air initially and allowed some contact with the surrounding environment, the rate of oxygen transport into the packages was a controlling factor. The higher value of dissolved U in package F as compared with package E indicates a greater degree of oxidative dissolution of the uraninite, which follows directly from the greater access to oxygen through the open port (assuming no uranyl phases precipitated in either case). Similarly, an identical experiment conducted with one side left completely open would be expected to show far higher levels of both Fe and U corrosion (this would be an appropriate control in future experiments).

As Fe oxidation proceeds, equilibrium reactions involving secondary phases may also play a role. A buffer is traditionally defined as a system that resists changes in pH (e.g., a mixture of roughly equal proportions of a weak acid and its conjugate base) or Eh (e.g., the magnetite-hematite buffer). Equilibrium lines for these reactions plot on Pourbaix diagrams as vertical and horizontal lines, respectively. If both products and reactants of a given reaction involving both redox and pH changes are present in a system, they may create a "buffer" that resists deviations in the system away from the equilibrium line. The measured pe-pH points for the packages form a rough line with a slope of approximately 1 e^- to 3 H^+, suggesting some buffering system with rapid kinetics relative to other reactions in this system.

The relative importance of above processes may have changed over the course of the experiment. Perhaps Fe(III) phases such as ferrihydrite (poorly crystalline

$Fe(OH)_3$), akaganeite (β-FeOOH), or lepidocrocite (γ-FeOOH) formed early, when oxygen was relatively abundant in the packages and corrosion rates may have been more rapid, and then slowly dissolved or converted to Fe(II)-bearing species after oxygen became depleted. This would explain the general increase in the Fe(II)/Fe(III) ratios of the solid corrosion products over time, and, depending on the reaction, may also account for the observed pH increase as in equation (2.2):

$$3FeOOH + H^+ + e^- \rightarrow Fe_3O_4 + 2H_2O \qquad (2.2)$$

If $O_{2(aq)}$ is sufficiently depleted, Fe(III) species may be the most important oxidizing agent in the system.

2.5b. Kinetic hindrance of UO_2 corrosion

The pe-pH diagram for U system depends largely on the water chemistry. In YMPW, which contains high levels of both Ca^{2+} and silica (Table 2.2), geochemical modeling using the Yucca Mountain Project thermodynamic database (SNL, 2007c) predicts that *under all pe-pH conditions tested* uranophane ($Ca[(UO_2)SiO_3(OH)]_2 \cdot 5H_2O$) is the thermodynamically stable phase. Uranophane has been noted as a corrosion product of uraninite/UO_2 under oxidizing conditions (Pearcy et al., 1994; Wronkiewicz et al., 1996).

The above thermodynamic prediction should be taken only as a starting point, both because of likely kinetic effects and because errors in thermodynamic measurements may lead to large changes in the calculated stability field (Ewing et al., 1999). The thermodynamic data for coffinite, which is known to be an important alteration product of uraninite under reducing and Si-rich conditions (Janeczek and Ewing, 1992), is especially problematic. Although coffinite was first synthesized over

50 years ago (Hoekstra and Fuchs, 1956; Fuchs and Gebert, 1958; Fuchs and Hoekstra, 1959), no calorimetric studies have been performed because of difficulties synthesizing a large enough pure sample (Robit-Pointeau et al., 2006) and available thermodynamic data for coffinite are not generally considered valid (Arcos et al., 2008). Also, this database does not include becquerelite ($Ca(UO_2)_6O_4(OH)_6 \cdot 8(H_2O)$), which is expected to be one of the most important phases in the UO_3-CaO-H_2O system (Kubatko et al., 2006).

The UO_2 grains in these experiments are not expected to be thermodynamically stable with the oxygenated fluids of the experiments, and their persistence indicates that oxidation was kinetically hindered. The decrease in measured redox conditions reflects a decrease in availability of the chemical reactant O_2, and limited reactant availability leads to slower reaction times. A layer of corrosion products surrounding the UO_2 grains may also have contributed by forming a protective barrier against oxygen and water.

2.5c. Implications for radionuclide release from waste packages

Standard conceptual models used in performance assessment analyses consider only two possible scenarios in the lifetime of the waste package: Before breach, when no water is available and the corrosion rate is negligible, and after breach, when water infiltrates the package and the spent nuclear fuel (SNF) is exposed to the open air and oxidized relatively quickly (SNL, 2007d). The results of this study suggest that a more accurate description of the rate of oxidative corrosion of spent nuclear fuel at the proposed repository site at Yucca Mountain should

include at least one intermediate stage: when the steel begins to corrode, conditions inside of the canister are more reducing, and SNF does not corrode significantly.

Given the many tons of carbon and stainless steel within the actual waste packages, reducing conditions are certain to exist inside of the waste package for some time, but any estimate of that time that is based only on these short-term experiments is unlikely to be meaningful. The relative rates of oxygen ingress and steel oxidation will be largely determined by the form and extent of the breach and the rate of water flow into the package, both of which may change over time. Even assuming a constant water flow and breach size, these experiments are too short in duration to determine any relation between the complete oxidation of carbon steel (expected in tens to hundreds of thousands of years (SNL, 2007a)) and final redox chemistry. Oxidizing conditions may, for instance, become established well before all of the carbon steel has corroded if the breached area is large, or reducing conditions may persist long afterwards due to the effect of corrosion of the stainless steel container or the formation of a protective layer of corrosion products.

The relatively low oxygen fugacities of this study (Figure 2.11) were measured using a steel type that corrodes relatively easily. Stainless steel, which has been proposed to replace carbon steel in the waste packages (SNL, 2007d), corrodes more slowly. Depending on the rate of fluid flow, use of this steel may either extend the period of lowered redox chemistry or, if the steel is sufficiently corrosion resistant, may not contribute to reducing conditions at all.

The effectiveness of corrosion products such as magnetite and hematite as radionuclide “getters” will depend on the water chemistry, particularly the carbonate

concentration and pH. Uranyl ions are known to form highly mobile carbonate complexes such as $(UO_2)_2CO_3(OH)_3^-$, $UO_2CO_3^o$, $UO_2(CO_3)_2^{2-}$ and $UO_2(CO_3)_3^{4-}$ (Grenthe et al., 1992), which are not easily adsorbed onto Fe oxides or other mineral surfaces (Jaffrezicrenault et al., 1980; Maya, 1982; Hsi and Langmuir, 1985; Ho and Miller, 1986; Venkataramani and Gupta, 1991; Duff and Amrhein, 1996). High carbonate concentrations, which may also increase the mobility of NpO_2^+ (Kohler et al., 1999), are expected at Yucca Mountain, and basic waters like those found in the packages will facilitate carbonate complex formation. However, over much longer time scales, corrosion modeling suggests that pH will be acidic, minimizing the importance of uranyl carbonate complexation (SNL, 2007b).

2.6. Conclusions

This study examined the corrosion products of A-516 steel and synthetic UO_2 over a two-year period under conditions likely to prevail at the proposed nuclear waste repository at Yucca Mountain shortly after the waste package is breached. Over this time period, approximately 5% of the steel interacting with water experienced some degree of corrosion, and the redox potential for the Fe(II)/Fe(III) couple decreased steadily. The UO_2 did not experience significant alteration, suggesting that for several years after breach, spent nuclear fuel corrosion and radionuclide release will be minimal.

2.7. References

Anastácio, A.S., Harris, B., Yoo, H.-I., Fabris, J.D., and Stucki, J.W. (2008) Limitations of the ferrozine method for quantitative assay of mineral systems for ferrous and total iron. Geochimica et Cosmochimica Acta, 72, 5001-5008.

Arcos, D., del Villar, L.P., Bruno, J., and Domenech, C. (2008) Geochemical modelling of the weathering zone of the "Mina Fe" U deposit (Spain): a natural analogue for nuclear spent fuel alteration and stability processes in radwaste disposal. Applied Geochemistry, 23, 807-821.

ASTM (2002) Standard Specification for Chromium and Chromium-Nickel Stainless Steel Plate, Sheet, and Strip for Pressure Vessels and for General Applications. American Society for Testing and Materials, West Conshohocken, PN.

- (2005) Standard Specification for High-Strength, Low-Alloy Structural Steel, up to 50 ksi (345Mpa) Minimum Yield Point, with Atmospheric Corrosion Resistance. American Society for Testing and Materials, West Conshohocken, PN.

Ben Lagha, S., Crusset, D., Mabille, I., Tran, M., Bernard, M.C., and Sutter, E. (2007) Corrosion of iron: A study for radioactive waste canisters. Journal of Nuclear Materials, 362, 485-492.

Callister, W.D. (2003) Material Science and Engineering: An Introduction. John Wiley & Sons, Inc, New York.

Cheng, Y.F., and Steward, F.R. (2004) Corrosion of carbon steels in high-temperature water studied by electrochemical techniques. Corrosion Science, 46(10), 2405-2420.

Cui, D.Q., and Eriksen, T.E. (1996) Reduction of pertechnetate in solution by heterogeneous electron transfer from Fe(II)-containing geological material. Environmental Science & Technology, 30(7), 2263-2269.

Dodge, C.J., Francis, A.J., Gillow, J.B., Halada, G.P., Eng, C., and Clayton, C.R. (2002) Association of uranium with iron oxides typically formed on corroding steel surfaces. Environmental Science & Technology, 36(16), 3504-3511.

Duff, M.C., and Amrhein, C. (1996) Uranium(VI) adsorption on goethite and soil in carbonate solutions. Soil Science Society of America Journal, 60(5), 1393-1400.

Dunn, D.S., Bogart, M.B., Brossia, C.S., and Cragnolino, G.A. (2000) Corrosion of iron under alternating wet and dry conditions. Corrosion, 56(5), 470-481.

Duro, L., El Aamrani, S., Rovira, M., de Pablo, J., and Bruno, J. (2008) Study of the interaction between U(VI) and the anoxic corrosion products of carbon steel. Applied Geochemistry, 23(5), 1094-1100.

Eng, C.W., Halada, G.P., Francis, A.J., Dodge, C.J., and Gillow, J.B. (2003) Uranium association with corroding carbon steel surfaces. Surface and Interface Analysis, 35(6), 525-535.

Ewing, R.C., Tierney, M.S., Konikow, L.F., and Rechard, R.P. (1999) Performance assessments of nuclear waste repositories: a dialogue on their value and limitations. Risk Analysis, 19(5), 933-958.

Fuchs, L.H., and Gebert, E. (1958) X-Ray studies of synthetic coffinite, thorite and uranothorites. American Mineralogist, 43, 243-248.

Fuchs, L.H., and Hoekstra, H.R. (1959) The preparation and properties of uranium(IV) silicate. American Mineralogist, 44, 1057-1063.

Fuhrmann, M., Bajt, S., and Schoonen, M.A.A. (1998) Sorption of iodine on minerals investigated by X-ray absorption near edge structure (XANES) and I-125 tracer sorption experiments. Applied Geochemistry, 13(2), 127-141.

Garcia, K.E., Morales, A.L., Arroyave, C.E., Barrero, C.A., and Cook, D.C. (2003) Mossbauer characterization of rust obtained in an accelerated corrosion test. Hyperfine Interactions, 148(1-4), 177-183.

Gerwin, W., and Baumhauer, R. (2000) Effect of soil parameters on the corrosion of archaeological metal finds. Geoderma, 96(1-2), 63-80.

Grambow, B., Smailos, E., Geckeis, H., Muller, R., and Hentschel, H. (1996) Sorption and reduction of uranium(VI) on iron corrosion products under reducing saline conditions. Radiochimica Acta, 74, 149-154.

Grenthe, I., Fuger, J., Konings, R., Lemire, R.J., Muller, A.B., Nguyen-Trung, C., and Wanner, J. (1992) The Chemical Thermodynamics of Uranium. Elsevier, Amsterdam.

Gu, B., Liang, L., Dickey, M.J., Yin, X., and Dai, S. (1998) Reductive precipitation of uranium(VI) by zero-valent iron. Environmental Science & Technology, 32(21), 3366-3373.

Harrar, J.E., Carley, J.F., Isherwood, W.F., and Raber, E. (1990) Report of the Committee to Review the Use of J-13 Well Water in Nevada Nuclear Waste Storage Investigations. Lawrence Livermore National Laboratory, Livermore, California.

Ho, C.H., and Miller, N.H. (1986) Adsorption of uranyl species from bicarbonate solution onto hematite particles. Journal of Colloid and Interface Science, 110(1), 165-171

Hoekstra, H.R., and Fuchs, L.H. (1956) Synthesis of Coffinite-$USiO_4$. Science, 123(3186), 105-105.

Hostettler, J.D. (1984) Electrode electrons, aqueous electrons, and redox potentials in natural-waters. American Journal of Science, 284(6), 734-759

Hsi, C.K.D., and Langmuir, D. (1985) Adsorption of uranyl onto ferric oxyhydroxides - application of the surface complexation site-binding model. Geochimica Et Cosmochimica Acta, 49(9), 1931-1941.

Jaffrezicrenault, N., Poirierandrade, H., and Trang, D.H. (1980) Models for the adsorption of uranium on titanium-dioxide. Journal of Chromatography, 201(NOV), 187-192

Janeczek, J., and Ewing, R.C. (1992) Dissolution and alteration of uraninite under reducing conditions. Journal of Nuclear Materials, 190, 157-173.

Janeczek, J., Ewing, R.C., Oversby, V.M., and Werme, L.O. (1996) Uraninite and UO_2 in spent nuclear fuel: a comparison. Journal of Nuclear Materials, 238(1), 121-130.

Janot, R., and Guerard, D. (2002) One-step synthesis of maghemite nanometric powders by ball-milling. Journal of Alloys and Compounds, 333(1-2), 302-307.

Jenne, E.A. (1981) Geochemical Modeling: A Review. Battelle Pacific Northwest Laboratory., Richland, WA.

Jensen, D.L., Boddum, J.K., Tjell, J.C., and Christensen, T.H. (2002) The solubility of rhodochrosite ($MnCO_3$) and siderite ($FeCO_3$) in anaerobic aquatic environments. Applied Geochemistry, 17(4), 503-511.

Kassim, J., Baird, T., and Fryer, J.R. (1982) Electron-Microscope Studies of Iron Corrosion Products in Water at Room-Temperature. Corrosion Science, 22(2), 147-158.

Kim, Y.J. (1999) Analysis of oxide film formed on type 304 stainless steel in 288 °C water containing oxygen, hydrogen, and hydrogen peroxide. Corrosion, 55(1), 81-88.

Kohler, M., Honeyman, B.D., and Leckie, J.O. (1999) Neptunium(V) sorption on hematite (alpha-Fe_2O_3) in aqueous suspension: the effect of CO_2. Radiochimica Acta, 85(1-2), 33-48.

Kubatko, K.A., Helean, K., Navrotsky, A., and Burns, P.C. (2006) Thermodynamics of uranyl minerals: enthalpies of formation of uranyl oxide hydrates. American Mineralogist, 91(4), 658-666.

Langmuir, D.L. (1996) Aqueous environmental geochemistry. Prentice-Hall, Upper Saddle River, NJ.

Legrand, L., Savoye, S., Chausse, A., and Messina, R. (2000) Study of oxidation products formed on iron in solutions containing bicarbonate/carbonate. Electrochimica Acta, 46(1), 111-117.

Leidheiser, H., and Music, S. (1982) The atmospheric corrosion of iron as studied by Mössbauer-spectroscopy. Corrosion Science, 22(12), 1089-1096.

Lindberg, R.D., and Runnells, D.D. (1984) Groundwater redox reactions - an analysis of equilibrium state applied to Eh measurements and geochemical modeling. Science, 225(4665), 925-927.

Maslar, J.E., Hurst, W.S., Bowers, W.J., Hendricks, J.H., and Aquino, M.I. (2000) In situ Raman spectroscopic investigation of aqueous iron corrosion at elevated

temperatures and pressures. Journal of the Electrochemical Society, 147(7), 2532-2542.

Maya, L. (1982) Sorbed uranium (VI) species on hydrous titania, zirconia, and silica-gel. Radiochimica Acta, 31(3-4), 147-151.

McMillian, S., Elkonz, S., Zarrabi, K., Cizdziei, J., and Stockman, H. (2002) Corrosion and transport processes in miniature waste packages. Abstracts of Papers of the American Chemical Society, 223, U614-U614.

Missana, T., Maffiotte, U., and Garcia-Gutierrez, M. (2003) Surface reactions kinetics between nanocrystalline magnetite and uranyl. Journal of Colloid and Interface Science, 261(1), 154-160.

Morris, J.C., and Stumm, W. (1967) Redox equilibria and measurements of potentials in the aquatic environment. In W. Stumm, Ed. Equilibrium Concepts in Natural Water Systems. American Chemical Society Advances in Chemistry Series 67, p. 270-285. American Chemical Society, Washington, D.C.

Moyes, L.N., Parkman, R.H., Charnock, J.M., Vaughan, D.J., Livens, F.R., Hughes, C.R., and Braithwaite, A. (2000) Uranium uptake from aqueous solution by interaction with goethite, lepidocrocite, muscovite, and mackinawite: an X-ray absorption spectroscopy study. Environmental Science & Technology, 34(6), 1062-1068.

Murphy, W.M., Pearcy, E.C., Green, R.T., Prikryl, J.D., Mohanty, S., Leslie, B.W., and Nedungadi, A. (1998) A test of long-term, predictive, geochemical transport modeling at the Akrotiri archaeological site. Journal of Contaminant Hydrology, 29(3), 245-279.

Music, S., Nowik, I., Ristic, M., Orehovec, Z., and Popovic, S. (2004) The effect of bicarbonate/carbonate ions on the formation of iron rust. Croatica Chemica Acta, 77(1-2), 141-151.

Neff, D., Dillmann, P., Bellot-Gurlet, L., and Beranger, G. (2005) Corrosion of iron archaeological artefacts in soil: characterisation of the corrosion system. Corrosion Science, 47(2), 515-535.

Oh, S.J., Cook, D.C., and Townsend, H.E. (1998) Characterization of iron oxides commonly formed as corrosion products on steel. Hyperfine Interactions, 112(1-4), 59-65.

Ohtsuka, T., Kubo, K., and Sato, N. (1986) Raman-spectroscopy of thin corrosion films on iron at 100-C to 150-C in air. Corrosion, 42(8), 476-481.

O'Loughlin, E.J., Kelly, S.D., Cook, R.E., Csencsits, R., and Kemner, K.M. (2003) Reduction of uranium(VI) by mixed iron(II)/iron(III) hydroxide (green rust): formation of UO2 nanoparticles. Environmental Science and Technology, 37, 721-727.

Pearcy, E.C., Prikryl, J.D., Murphy, W.M., and Leslie, B.W. (1994) Alteration of uraninite from the Nopal-I deposit, Pena-Blanca District, Chihuahua, Mexico,

compared to degradation of spent nuclear-fuel in the proposed United-States high-level nuclear waste repository at Yucca Mountain, Nevada. Applied Geochemistry, 9(6), 713-732.

Pepper, S.E., Bunker, D.J., Bryan, N.D., Livens, F.R., Charnock, J.M., Pattrick, R.A.D., and Collison, D. (2003) Treatment of radioactive wastes: an X-ray absorption spectroscopy study of the reaction of technetium with green rust. Journal of Colloid and Interface Science, 268(2), 408-412.

Pratt, J.H. (1894) On the determination of ferrous iron in silicates. American Journal of Science, 48, 149.

Remazeilles, C., and Refait, P. (2008) Formation, fast oxidation and thermodynamic data of Fe(II) hydroxychlorides. Corrosion Science, 50(3), 856-864.

Riba, O., Scott, T.B., Ragnarsdottir, K.V., and Allen, G.C. (2008) Reaction mechanism of uranyl in the presence of zero-valent iron nanoparticles. Geochimica et Cosmochimica Acta, 72(16), 4047-4057.

Robit-Pointeau, V., Poinssot, C., Vitorge, P., Grambow, B., Cui, D., Spahiu, K., and Catalette, H. (2006) Assessment of the relevance of coffinite formation within the near-field environment of spent nuclear fuel geological disposals. In P.V. Iseghem, Ed, 932, p. 489-496. Material Research Society Symposium Proceedings, Ghent, Belgium.

Roh, Y., Lee, S.Y., and Elless, M.P. (2000) Characterization of corrosion products in the permeable reactive barriers. Environmental Geology, 40(1-2), 184-194.

Rovira, M., El Aamrani, S., Duro, L., Gimenez, J., de Pablo, J., and Bruno, J. (2007) Interaction of uranium with in situ anoxically generated magnetite on steel. Journal of Hazardous Materials, 147(3), 726-731.

Savoye, S., Legrand, L., Sagon, G., Lecomte, S., Chausse, A., Messina, R., and Toulhoat, P. (2001) Experimental investigations on iron corrosion products formed in bicarbonate/carbonate containing solutions at 90 °C. Corrosion Science, 43(11), 2049-2064.

Schikorr, G. (1933) On iron (II)-hydroxide and a ferromagnetic iron(III)-hydroxide. Zeitschrift für Anorganische und Allgemeine Chemie, 212(1), 33-39.

Schwertmann, U., and Fechter, H. (1994) The formation of green rust and its transformation to lepidocrocite. Clay Minerals, 29(1), 87-92.

Scott, T.B., Allen, G.C., Heard, P.J., and Randell, M.G. (2005) Reduction of U(VI) to U(IV) on the surface of magnetite. Geochimica et Cosmochimica Acta, 69(24), 5639-5646.

Sherman, D.M., Peacock, C.L., and Hubbard, C.G. (2008) Surface complexation of U(VI) on goethite ([alpha]-FeOOH). Geochimica et Cosmochimica Acta, 72(2), 298-310.

SNL (2007a) EBS Radionuclide Transport Abstraction. Sandia National Laboratories, Las Vegas, NV.

- (2007b) In-package Chemistry Abstraction. Sandia National Laboratories, Las Vegas, NV.

- (2007c) Qualification of Thermodynamic Data for Geochemical Modeling of Mineral-Water Interations in Dilute Systems. Sandia National Laboratories, Las Vegas, NV.

-. (2007d) Total System Performance Assessment Data Input Package for Requirements Analysis for Transportation Aging and Disposal Canister and Related Waste Package Physical Attributes Basis for Performance Assessment. Sandia National Laboratories, Las Vegas, NV.

Stahl, K., Nielsen, K., Jiang, J.Z., Lebech, B., Hanson, J.C., Norby, P., and van Lanschot, J. (2003) On the akaganeite crystal structure, phase transformations and possible role in post-excavational corrosion of iron artifacts. Corrosion Science, 45(11), 2563-2575.

Stefansson, A., Amorsson, S., and Sveinbjornsdottir, A.E. (2005) Redox reactions and potentials in natural waters at disequilibrium. Chemical Geology, 221(3-4), 289-311.

Stookey, L.L. (1970) Ferrozine - a new spectrophotometric reagent for iron. Analytical Chemistry, 42, 779.

Teterin, A.Y., Maslakov, K.I., Teterin, Y.A., Kalmykov, S.N., Ivanov, K.E., Vukcevic, L., Khasanova, A.B., and Shcherbina, N.S. (2006) Interaction of neptunyl with goethite (alpha-FeOOH), maghemite (gamma-Fe_2O_3), and hematite (alpha-Fe_2O_3) in water as probed by X-ray photoelectron spectroscopy. Russian Journal of Inorganic Chemistry, 51(12), 1937-1944.

Xu, W.X., VanderVoo, R., Peacor, D.R., and Beaubouef, R.T. (1997) Alteration and dissolution of fine-grained magnetite and its effects on magnetization of the ocean floor. Earth and Planetary Science Letters, 151(3-4), 279-288.

Venkataramani, B., and Gupta, A.R. (1991) Effect of anions on the sorption of uranyl ions on hydrous oxides - application of the surface hydrolysis model. Colloids and Surfaces, 53(1-2), 1-19.

Weber, W.J. (1981) Ingrowth of lattice-defects in alpha irradiated UO2 single-crystals. Journal of Nuclear Materials, 98(1-2), 206-215.

Wolery, T.W., and Jarek, R.L. (2002) EQ3NR Speciation-Solubility Code (EQ3/6-V8-EQ3NR-EXE-R43-PC). The Regents of the University of California, Lawrence Livermore National Laboratory.

Wronkiewicz, D.J., Bates, J.K., Wolf, S.F., and Buck, E.C. (1996) Ten-year results from unsaturated drip tests with UO_2 at 90 °C: implications for the corrosion of spent nuclear fuel. Journal of Nuclear Materials, 238(1), 78-95.

Zachara, J.M., Heald, S.M., Jeon, B.H., Kukkadapu, R.K., Liu, C.X., McKinley, J.P., Dohnalkova, A.C., and Moore, D.A. (2007) Reduction of pertechnetate Tc(VII) by aqueous Fe(II) and the nature of solid phase redox products. Geochimica et Cosmochimica Acta, 71(9), 2137-2157.

CHAPTER 3.

SIMULATION OF THERMODYNAMIC MIXING PROPERTIES OF ACTINIDE-CONTAINING ZIRCON SOLID-SOLUTIONS

3.1. Abstract

Solid solutions among zircon ($ZrSiO_4$, $I4_1/amd$) and zircon-structured orthosilicates $ASiO_4$ (A = Hf, Th, U, Pu, or Ce) are important to a wide variety of applications: nuclear materials, geochronology, and even electronic materials. The thermodynamic mixing properties of the following seven binary solid solutions were simulated using density functional theory followed by Monte Carlo modeling and thermodynamic integration: $(Zr,Hf)SiO_4$, $(Zr,Th)SiO_4$, $(Zr,U)SiO_4$, $(Zr,Pu)SiO_4$, $(Zr,Ce)SiO_4$, $(Hf,Pu)SiO_4$, and $(Th,U)SiO_4$. $ZrSiO_4$ and $HfSiO_4$ were found to form a nearly ideal solid solution, but the miscibility of the other solid solutions was limited to no more than 12 mol% of the substituting cation. The binaries were ranked by extent of miscibility: $(Zr,Hf)SiO_4$ > $(Th,U)SiO_4$ > $(Zr,Ce)SiO_4$ > $(Zr,Pu)SiO_4$ > $(Hf,Pu)SiO_4$ > $(Zr,U)SiO_4$ > $(Zr,Th)SiO_4$. The extent of solid solution has been estimated for each binary. The end-members $PuSiO_4$, $CeSiO_4$, and $USiO_4$ were determined to be unstable relative to a mixture of $SiO_{2(quartz)}$ and crystalline PuO_2, $CeO_{2(cerianite)}$, or $UO_{2(uraninite)}$. Isostructural thorite ($ThSiO_4$) is calculated to be marginally stable, but its monoclinic polymorph, huttonite, which has the structure of

monazite, is marginally unstable relative to $SiO_{2(quartz)}$ and $ThO_{2(thorianite)}$. If thermodynamic equilibrium could be reached at low temperatures, exsolution textures would appear in most zircon solid solutions perpendicular to [001] but parallel to [001] in $(Hf,Pu)SiO_4$.

3.2. Introduction

Zircon ($ZrSiO_4$, $I4_1/amd$) is a ubiquitous trace mineral known for its high melting point (Levin and McMurdie 1975), hardness (7.5 on Moh's hardness scale), low thermal expansion (Subbarao 1990), low compressibility (Sirdeshmukh and Subhadra 1975), good thermal shock resistance (Grover and Tyagi 2005), and ability to incorporate and retain a wide range of impurities, particularly actinides and the rare earths. $ZrSiO_4$ is an important opacifier in the manufacturing of glazes (Bhushan and Sen 1965; Naher and Haseeb 2008), and has been suggested for use in thermal barrier coatings in engines (Cao et al. 2004) and in solid state lasers (Babsail et al. 1991). Both $ZrSiO_4$ and isostructural $HfSiO_4$ have also been proposed for use as gate materials in silicon field effect transistors (Wilk and Wallace 1999; Robertson 2000; Wilk et al. 2000). Zircon is most important for applications in geoscience and nuclear engineering.

Zircon has long been used by geoscientists for U/Th/Pb age-dating, thermochronology based on the release of He, and for distinguishing between crustal and mantle sources of magma based on rare earth distributions (Harley and Kelly 2007). Fine-scale chemical zoning and isotopic signatures may be preserved over long time scales because diffusion for elements such as Hf^{4+}, the rare-earths (REE)

and the actinides, Th^{4+} and U^{4+}, is so slow that they are essentially immobile in the zircon structure (Cherniak et al. 1997a; 1997b). Lu/Hf and $^{176}Hf/^{177}Hf$ ratios have been used to determine the timing of crustal residence and growth, as well as the sources of the magma from which zircon formed, and REE distributions provide further insight into magmatic histories (*e.g.* (Hawkesworth and Kemp 2006; Harley and Kelly 2007; Scherer et al. 2007)).

Phases with the zircon structure are also an important class of nuclear materials. Coffinite ($USiO_4$), for example, is expected to be an important alteration phase of spent nuclear fuel under reducing conditions (Janeczek and Ewing 1992b; Bros et al. 2003; Amme et al. 2005), and the coprecipitation of actinides by $USiO_4$ has been noted as a potentially important retardation mechanism in a geologic repository (Bros et al. 2003; Grambow and Giffaut 2006). Zircon has also been proposed as a principal phase in inert matrix fuels (IMF), a type of nuclear fuel that may be used to fission Pu and the minor actinides Cm, Am, and Np, thereby reducing the actinide inventory (Kleykamp 1999; Grover and Tyagi 2005). Zr-based compounds also have the advantage that Zr has a very low neutron cross-section, and the neutronic characteristics of this system, particularly the Doppler reactivity feedbacks, may be improved by the additional incorporation of Th (Vettraino et al. 1999).

Zircon has been proposed as a nuclear waste form for the immobilization of Pu (Ewing et al. 1995; Gibb et al. 2008). However, zircon is more susceptible to radiation damage than other potential actinide waste forms (Lumpkin 2006; Farnan et al. 2007) and has a relatively low waste loading capacity as compared with other

ceramic waste forms, such as pyrochlore ($Gd_2(Ti,Hf)_2O_7$) and monazite ($(REE)PO_4$), which can incorporate more than 20 wt% Pu (Lumpkin 2006). Zircon grains have been successfully synthesized and doped with up to 10 wt% Pu (Haaker and Ewing 1981; Exarhos 1984; Weber 1990; Burakov et al. 1996; Hanchar et al. 2004) or 7 wt% Ce, a commonly used surrogate for Pu (Pepin et al. 1981; Vance 1994; Ushakov et al. 1998; Xu and Wang 1999; Kim et al. 2008), but the solvus and maximum actinide incorporation capacity has not been determined. When concentrations of Pu exceed a few weight percent, the possibility of sustained criticality must be considered (Ushakov et al. 1999). Therefore, there an interest in knowing the extent of solution sollution for elements, such as Hf and Gd, which have large neutron cross-sections (Weber et al. 1996; Meldrum et al. 1999; Burakov et al. 2000). Gd is less probably less applicable than Hf as a neutron absorber in zircon because of its relatively large size and 3+ charge, which would require a coupled substitution.

In this study, quantum mechanical modeling is combined with statistical methods to simulate the thermodynamic mixing properties of solid solutions with the zircon structure as a function of Hf, U, Th, Pu, and Ce substitution into the 8-fold site.

3.3. Zircon solid solutions in nature and experiments

Minerals with the zircon structure include $HfSiO_4$ (hafnon), $USiO_4$ (coffinite), $ThSiO_4$ (thorite), and YPO_4 (xenotime). The most common substitutions in zircon are Hf, Y, rare earth elements (REE), P, U, and Th (Hoskin and Schaltegger 2003). Incorporation of Hf, REE, and actinides in zircon may occur by one or more of the following mechanisms (Romans et al. 1975; Hinton and Upton 1991; Finch et al. 2001; Hanchar et al. 2001): (1) direct substitution into the Zr site, (2) coupled

substitution, such as YPO_4 for $ZrSiO_4$ (Speer 1982b; Caruba and Iacconi 1983; Halden et al. 1993), (3) substitution at an interstitial site (Hoskin et al. 2000), and (4) substitution of two trivalent cations for Zr^{4+} coupled with an oxygen vacancy (Williford et al. 2000). The incorporation mechanism for large 4+ cations such as Hf^{4+}, Th^{4+}, U^{4+} and Pu^{4+} into zircon and thorite is predominantly by direct substitution into the 8-fold Zr-site, although some incorporation may also occur at interstitial sites (Begg et al. 2000; Williford et al. 2000; Finch and Hanchar 2003). The Zr site consists of four shorter $\langle Zr-O \rangle$ bonds (2.13 Å) and four longer $\langle Zr-O' \rangle$ bonds (2.26 Å) (Figure 3.1).

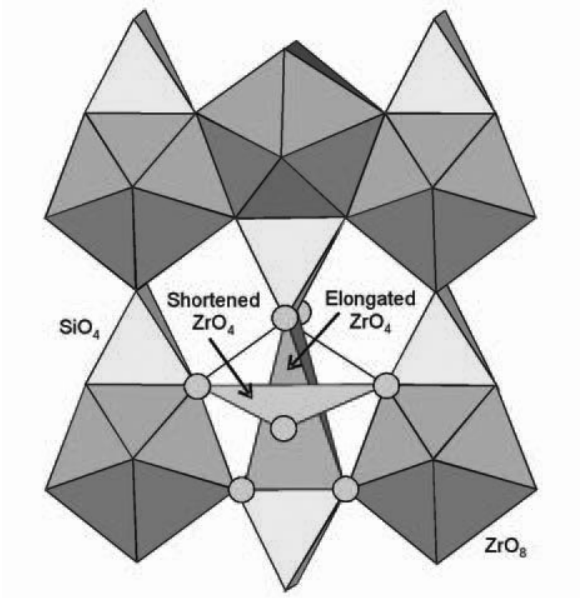

Figure 3.1. Zircon structure projected on [100]. Lighter polyhedra are SiO_4, and darker polyhedra are ZrO_8. One ZrO_8 polyhedron is drawn to show the sub-structure of two distorted ZrO_4 tetrahedra (taken from Harley and Kelly (2007)).

3.3a. Hf and rare earth elements

$HfSiO_4$ and $ZrSiO_4$ have been shown to form a complete solid solution (Ramakrishnan et al. 1969), although the extent of Hf solid solution in natural samples is more limited (Hoskin and Schaltegger 2003). The Hf concentrations

observed in natural zircon range from 0.15 wt% HfO_2 in zircon from Chilean granodiorite (Ballard et al. 2002) to 22 wt% in Slovakian granitic pegmatite zircon (Uher and Cerny 1998). Higher Hf levels are typically associated with more evolved rock types and increased magmatic differentiation (Hoskin and Schaltegger 2003).

While the Hf content is often high enough for it to be considered a minor element in zircon, the rare earth elements (REE) usually occur as trace elements at ppm levels (Hoskin and Schaltegger 2003). The REE may be classified into three groups: light REE (LREE), La-Pr; medium REE (MREE), Nd-Gd; and heavy REE (HREE) Tb-Lu. Most REE are trivalent, and the incorporation of REE^{3+} into zircon is often explained by the coupled xenotime-type substitution in which Y^{3+} and $HREE^{3+}$ substitute for Zr^{4+} while P^{5+} substitutes for Si^{4+} (Speer 1982b). Because of their smaller size, MREE and HREE are typically more compatible in the zircon structure than LREE. However, the ability of zircon to incorporate P^{5+} and other charge-balancing species also plays a role (Hanchar et al. 2001). Anhydrous xenotime usually does not substitute for more than 1 mol% in $ZrSiO_4$, although Y and HREE have been reported up to about 15 wt% (Förster 2006) and references therein). The element Ce has a higher concentration in some natural zircon than would be expected from an LREE (Zinner and Crozaz 1986). Studies of samples with low P content suggest that this anomaly may be attributed to the presence of Ce^{4+}, which substitutes directly for Zr^{4+} (Hinton and Upton 1991). Ce ranges in natural zircon from roughly 3 to 160 ppm (Hoskin and Schaltegger 2003), and references therein), or less than 0.02 mol% $CeSiO_4$.

Zircon containing 4 mol% and 2 mol% $CeSiO_4$ have synthesized using the sold-gel technique with sintering in air at 1400 °C and at 1600 °C, respectively (Ushakov et al. 1998). These compositions were estimated based on measured unit cell contents and an assumption of linearity between the unit cell constants of $ZrSiO_4$ and $CeSiO_4$. $CeSiO_4$ had not yet been synthesized at the time of the study, so its unit cell parameters were estimated as **a**=6.96 Å, **c**=6.20 Å (Caruba et al. 1975), which are not much different from subsequently measured unit cell parameters (**a**= 6.9564 Å, **c**= 6.1953 Å) (Skakle et al. 2000). High resolution transmission electron microscopy (HRTEM) of some samples showed inclusions of $Ce_2Si_2O_7$ and 50-200 nm globules of $(Zr,Ce)O_2$ (Ushakov et al. 1998). Subsequent laboratory studies at sintering temperatures ranging between 1400 and 1700 °C (calcining was at 900 °C) found an average of 7 ± 1 mol% $CeSiO_4$ using analytical electron microscopy (AEM) (Ushakov et al. 1999). The presence of Ce^{3+} could not be ruled out, but Ce^{3+} substitution into zircon in the absence of P or S would require an anion deficiency. A different study, in which powders of ZrO_2 and CeO_2 were crushed and annealed at 1400 °C, found almost no incorporation of Ce in $ZrSiO_4$ (Grover and Tyagi 2005). If the Ce in this study was reduced to Ce^{3+}, incorporation may be limited due to an absence of charge balancing species such as P^{5+}. The same study noted about 10 mol% Ce incorporated in $ThSiO_{4(thorite)}$ (Grover and Tyagi 2005).

3.3b. Actinides

All of the lighter actinides (Th - Am) form $ASiO_4$ phases isostructural with zircon, including the minerals coffinite ($USiO_4$) and thorite ($ThSiO_4$) (Keller 1963; Speer 1982a). The two lightest actinides, Th and Pa, also form monoclinic

polymorphs of $ASiO_4$ isostructural with monazite $(REE)PO_4$ (Finch and Hanchar 2003). The actinide orthosilicates show only limited solid solution with zircon ($ZrSiO_4$) in laboratory studies (Mumpton and Roy 1961; Ushakov et al. 1999), although many natural samples show much higher levels of Th and U (Förster 2006). The apparently wide miscibility gaps among $ZrSiO_4$ and $ASiO_4$ (A=actinide) have been explained as being due to the large differences in ionic radii between the actinides and 8-fold coordinated Zr^{4+} (Speer and Cooper 1982). The heavier actinides Am, Cm, and Bk are most often in the trivalent state (Cm^{4+} has not been observed), suggesting that a coupled substitution, such as the xenotime-type substitution, is the preferred mechanism of incorporation at trace levels in zircon.

Two methods have been used to synthesize Pu-doped zircon: hydrothermal- or solution-gelation for preparing polycrystalline zircon (Haaker and Ewing 1981; Exarhos 1984; Weber 1990) and the flux method (usually involving lithium molybdate), which can produce single crystals up to a few mm in size (Ballman and Laudise 1965; Ball and Wanklyn 1976; Poirot et al. 1989; Burakov et al. 2002; Hanchar et al. 2003). A variation of the solution-gelation method has also been used to prepare Ce, U, and Th-doped zircon (Ushakov et al. 1999). Zircon has not been prepared with greater than 8 mol% $PuSiO_4$ (10 wt% Pu) using either method.

Zircon synthesized using a hydrothermal gelation has been used primarily in radiation damage effect studies (e.g. (Weber 1990; Weber et al. 1994)). These crystals have been shown to contain trivalent Pu when sintered under reducing conditions (Hess et al. 1998a; 1998b). One possible charge-balancing mechanism involves a substitution of two nearest-neighbor Zr^{4+} atoms for two Pu^{3+} atoms coupled with a

nearby oxygen vacancy (Williford et al. 2000). Sintering in air resulted in oxidation of Pu to Pu^{4+} and a decrease in structural distortion as a result of the smaller ionic radius of Pu^{4+} than Pu^{3+} on the Zr^{4+} site (Begg et al. 2000). Studies using the hydrothermal gelation method (Exarhos 1984; Weber 1990; 1991) observed a total of 10 wt% Pu (8 mol% $PuSiO_4$), but two points remain unclear: (1) how much of this Pu is actually incorporated into the structure? and (2) was thermodynamic equilibrium reached? When a sample of the 10 wt% Pu zircon is annealed in air at 1200 °C, a "significant amount" of PuO_2 formed, enough to be apparent in an X-ray diffraction pattern (Begg et al. 2000). The authors describe this PuO_2 as having been "exsolved", but this term is not correct because a balanced reaction must also include a third product, SiO_2: $2(Zr,Pu)SiO_4 \rightarrow ZrSiO_4 + PuO_2 + SiO_2$.

Pu-doped zircon generated using the flux method also resulted in the formation of PuO_2 in samples containing 10 wt% Pu (Burakov et al. 2000). Hanchar *et al.* (2004) grew zircon crystals at 1220 °C, with 5-14 wt% Pu determined by electron microprobe analysis (EMPA) across a single zircon crystal. No inclusions of separate Pu phases were observed using powder XRD, optical microscopy, and scanning electron microscopy (SEM), and the authors concluded that the zircon structure can incorporate more than 10 wt% Pu in solid solution (Hanchar et al. 2004). The discrepancy with previous studies that showed PuO_2 phases forming in high-Pu content zircon formed by a similar method (Burakov et al. 2000) is not explained, and EMPA appears to have been performed on only one 0.5 mm line of a single sample. The presence of PuO_2 may be compatible with high-Pu zircon, but

SiO_2 must also be present unless the experiments were conducted with compositions off the binary.

The two naturally occurring actinide orthosilicates with the zircon structure are coffinite ($USiO_4$) and thorite ($ThSiO_4$). Coffinite is an important U ore (Plant et al. 1999). Thorite is usually found in pegmatites and as an accessory mineral in a variety of igneous and metamorphic rocks (Speer 1982a). Coffinite typically occurs only as microcrystals associated with a large amount of other phases, such as sulfides or organic material (Smits 1989; Deditius et al. 2008). Relatively large and pure samples of thorite have been synthesized (Mazeina et al. 2005; Konings et al. 2008) but not coffinite (Fuchs and Hoekstra 1959; Robit-Pointeau et al. 2006), and the role of water and $(OH)^-$ in coffinite is unclear (Janeczek 1991; Janeczek and Ewing 1992a), and references therein). Natural samples indicate a extensive of solid solution among coffinite, thorite and zircon (Förster 2006), whereas laboratory studies suggest a much wider solvus (Mumpton and Roy 1961).

Although U in natural zircon is typically less than 5000 ppm, and the Th is less than 1000 ppm, weight percent levels do occur (Harley and Kelly 2007). Zircon from granite has been reported with 11 mol% $USiO_4$ (Breiter et al. 2006) and 37 mol% $ThSiO_4$ (Förster 2006). Zircon formed in the melted nuclear power plant core from the 1986 accident at the Chernobyl contains $USiO_4$ ranging from 0.6 to 11.6 mol% $USiO_4$ (Anderson et al. 1993; Geisler et al. 2005). An intensely altered granite has been described that is reported to contain 28 mol% $ZrSiO_4$ in coffinite and 51 mol% $ZrSiO_4$ in thorite (Pointer et al. 1988a). Conglomerates in Witwatersrand, South Africa, include silicates with 30 wt% UO_2 (36 mol% $USiO_4$) in thorite and 15.9

wt% ThO_2 (19.0 mol% $ThSiO_4$) in coffinite (Smits 1989). High U and Th contents have also been observed in zircon from some granite and altered granite occurrences (Pagel 1982; Lumpkin and Chakoumakos 1988; Pointer et al. 1988b; Förster 2006).

Experimental studies on the simple binary subsystems using two anhydrous end-members show much more limited solid solution in the $USiO_4$-$ThSiO_4$-$ZrSiO_4$ system. Zircon containing up to 20 mol% $USiO_4$ has been synthesized, but this mixture exsolved to 4 ± 2 mol% $USiO_4$ when reheated at unspecified higher temperatures (Mumpton and Roy 1961). They were also able to prepare zircon containing 35 mol% $ThSiO_4$ and thorite containing 25 mol% $ZrSiO_4$. However, they concluded these products were unstable and that less than 4 ± 2 mol% $ThSiO_4$ could be substituted in zircon, and no more than 6 ± 2 mol% $ZrSiO_4$ in either thorite or huttonite. In a different study, zircon containing 4 ± 1 mol% $USiO_4$ and 2 ± 0.5 mol% $ThSiO_4$ was synthesized around 1500 °C (Ushakov et al. 1999). Any inclusions or small-scale exsolution lamellae were not evident from XRD or AEM. Complete solid solution between $USiO_{4(coffinite)}$ and $ThSiO_{4(thorite)}$ has been reported for samples synthesized at 250 °C (Fuchs and Gebert 1958; Fuchs and Hoekstra 1959), whereas up to 20 mol% $USiO_4$ in $ThSiO_4$ was found at 1350 °C (Mumpton and Roy 1961).

Previous studies concluded that the high-U and -Th zircon and thorite observed in nature is unlikely to be thermodynamically stable on the grounds that wide miscibility gaps have been observed in laboratory studies (Pointer et al. 1988a; Förster 2006). However, this conclusion implicitly assumes that laboratory experiments at low pressures are more likely to attain equilibrium than in crystalline rocks. This assumption does not hold for a number of orthosilicate systems (*e.g.*,

natural seed crystals are required in order to synthesize sillimanite or garnet near their stability limits (Richardson et al. 1969; Hensen and Essene 1971; Essene 1989)). Furthermore, natural zircon, coffinite and thorite may contain three or even all four of the components in the system $ZrSiO_4$-$ThSiO_4$-$USiO_4$-YPO_4 (Förster 2006). The presence of additional components, especially Y^{3+} and xenotime ($(Y,HREE)PO_4$), and perhaps OH, may be important for stabilizing solid solutions in zircon. Therefore a comparison between these complex systems and simple binaries is unlikely to be meaningful, particularly given the differences in pressure-temperature conditions and time-scales. Table 3.1 provides a compilation of the maximum amount of solid solution observed in the zircon structure, in natural and synthetic samples. These systems were formed under a range of P-T and chemical conditions (see above discussion), and therefore are not directly comparable.

3.4. Methods

Methods for simulating solid solutions have been discussed thoroughly elsewhere (Bosenick et al. 2001; Dove 2001; Warren et al. 2001) and will, therefore, be described only briefly. Generation of thermodynamic mixing curves involves four steps: (1) calculation of the total energy for representative compositions and configurations, (2) fitting interaction parameters to the exchangeable cation pairs (e.g., nearest neighbor and second nearest neighbor Pu-Zr, Pu-Pu, or Zr-Zr), (3) Monte-Carlo simulations to obtain excess enthalpies of mixing, and (4) subsequent thermodynamic integration to obtain the corresponding free energies and entropies of mixing.

Table 3.1 Maximum observed compositions in different $ASiO_4$ solid solutions

component	host structure	max. in nature (mol% $ASiO_4$)	max. experimental * (mol% $ASiO_4$)	calculated at 1000 K	nature ref.	experiment ref.
$HfSiO_4$	$ZrSiO_4$	21	complete	complete	(Uher and Cerny 1998)	(Ramakrishnan et al. 1969)
$CeSiO_4$	$ZrSiO_4$	0-0.2 (3-160 ppm)	7 ± 1	1.2	(Hoskin and Schaltegger 2003)	(Ushakov et al. 1999)
$PuSiO_4$	$ZrSiO_4$	(no Pu)	8	0.05	-	(Weber 1990; Hanchar et al. 2004)
$PuSiO_4$	$HfSiO_4$	(no Pu)	5	< 0.01	-	(Burakov et al. 2000)
$USiO_4$	$ZrSiO_4$	11	4 ± 1; 11.6 20 → 4 ± 2	0.01	(Breiter et al. 2006)	(Mumpton and Roy 1961; Anderson et al. 1993; Ushakov et al. 1999)
$ThSiO_4$	$ZrSiO_4$	37	2 ± 0.5; 35 → 4 ± 2	< 0.01	(Förster 2006)	(Mumpton and Roy 1961; Ushakov et al. 1999)
$ZrSiO_4$	$ThSiO_4$	51.3	25 → 6 ± 2	0.02	(Pointer et al. 1988a)	(Mumpton and Roy 1961)
$ZrSiO_4$	$USiO_4$	27.5	(not available)	0.07	(Pointer et al. 1988a)	-
$ThSiO_4$	$USiO_4$	19	(not available)	0.10	(Smits 1989)	-
$USiO_4$	$ThSiO_4$	36	complete; 20	0.17	(Smits 1989)	(Fuchs and Gebert 1958; Mumpton and Roy 1961)

* Estimates shown to the left of arrows indicate a likely metastable solid solution.

3.4a. Total-energy calculations

The stability of a given composition within a solid solution series, for instance $Pu_{0.5}Zr_{0.5}SiO_4$, can be assessed by calculating the excess energy of mixing (E_{excess}), i.e., the difference between the total energy of that composition and the energy of a mechanical mixture of end-members ($PuSiO_4$ and $ZrSiO_4$) with the same bulk composition. A negative E_{excess} indicates that the solid-solution composition is favorable, while a composition with a positive E_{excess} is unfavorable.

There are two general categories of simulation techniques for determining total energies: empirical methods, which use fitted force-field potentials using classical mechanics, and quantum-mechanical methods, which solve the Schrödinger equation. Empirical methods are sometimes adequate for simulating solid solutions (Bosenick et al. 2001), but in this system, DFT is the preferred method for two reasons: (1) although empirical potentials have been derived specifically for Pu and U in zircon (Meis and Gale 1998), there are no similar potentials for Th, Ce and Hf (i.e., potentials that have been derived in the same system, using comparable experimental data and the same transferable, e.g., O-O potentials), and (2) quantum mechanics allows electronic relaxation, typically resulting in more accurate total energies. The latter point is particularly important if the solid solution involves atoms that carry unpaired spins, and spin-spin interactions contribute to the overall energy.

Total energies for the zircon structure were calculated for 19 to 27 configurations for each of the following seven solid solutions: $(Zr,Hf)SiO_4$, $(Zr,Th)SiO_4$, $(Zr,U)SiO_4$, $(Zr,Pu)SiO_4$, $(Zr,Ce)SiO_4$, $(Hf,Pu)SiO_4$, and $(Th,U)SiO_4$ using density function theory (DFT) as implemented by the software package VASP

(Vienna Ab-initio Simulation Package). All quantum mechanical calculations were completed using 0.07 $Å^{-1}$ *k*-point spacing and 800 eV planewave cut-off energy. The local density approximation (LDA) was chosen over the general gradient approximation (GGA) because LDA results are in better agreement with experimentally-determined zircon unit cell parameters (Ferriss et al. 2008). Even though the spin distribution was allowed to relax, the atomic spins of U and Pu remained constant at 2 and 4, respectively, in all calculations. All other elements were assigned an initial spin of 0 in agreement with their electron configuration. Energies of constituent oxides (*e.g.*, $SiO_{2(quartz)}$ and $ZrO_{2(baddeleyite)}$ for $ZrSiO_4$) were calculated for each end-member using the same computational parameters.

3.4b. Fitting of Margules and interaction parameters

Each solid solution was evaluated using an 8 × 8 × 8 supercell containing 2048 exchangeable cations. In order to calculate many (on the order of millions) of the possible configurations in this supercell, the calculated excess energies were first fit a series of interaction parameters (*J*'s), each of which represents the energy of a particular cation-cation interaction type *i* (that are dependent on spatial relationship, *e.g.*, distance, between two cations). The total energy E_{config} for a given configuration can then be approximated by the sum of the number *n* of *i*-type interactions for each cation pair multiplied by an interaction parameter *J* that describes the energy of the cation-cation interaction:

$$E_{config} = \sum_i \left(n_i J_i \right) \tag{3.1}$$

J is defined here by the following equation:

$$J = E_{AB} - \frac{1}{2}(E_{AA} + E_{BB}) \quad (3.2)$$

where E is the interaction energy between two exchangeable cations, A and B. A positive J value indicates that for that particular interaction type homo-cationic interactions (*e.g.,* Zr-Zr or Pu-Pu) are favored (i.e., AB avoidance), whereas a negative J value indicates that hetero-cationic interactions (*e.g.,* Pu-Zr) are favored. The value of J will change for each of the interaction types, i, which are defined for each solid solution by the geometric relationships between the exchangeable cations (Table 3.2). The $ZrSiO_4$ end-member interaction types were used for all solid solutions that included zircon as an end-member. The $PuSiO_4$ end-member i's were used for the $(Pu,Hf)SiO_4$ solid solution, which did not contain Zr, and the $USiO_4$ end-member i's were used for the $(U,Th)SiO_4$ and solid solution.

Table 3.2. Cation-cation interaction types *i* defined by distances between exchangeable cations and absolute values of Δx (// to (100), Δy* (// to (010) and Δz (// to (001)

end-member	label *i*	distance (Å)	dx (Å)	dy (Å)	dz (Å)
$ZrSiO_4$	1	3.62	0.00	3.30	1.49
$ZrSiO_4$	2	5.54	3.30	3.30	2.98
$ZrSiO_4$	3	5.56	0.00	3.30	4.48
$ZrSiO_4$	4	5.93	0.00	0.00	5.93
$PuSiO_4$	1	3.76	3.43	0	1.54
$PuSiO_4$	2	5.74	3.43	3.43	3.08
$PuSiO_4$	3	5.75	0	3.43	4.62
$PuSiO_4$	4	6.16	0.00	0.00	6.16
$USiO_4$	1	3.78	3.45	0	1.55
$USiO_4$	2	5.78	3.45	3.45	3.10
$USiO_4$	3	5.79	0	3.45	4.66
$USiO_4$	4	6.21	0.00	0.00	6.21

*dx and dy are interchangeable for a given interaction type.

The J's are fit along with a Margules function, which describes the asymmetry and concentration-dependent (but configuration-independent) aspect of the energy of

a disordered system. The Margules energy term, E_0, represents the excess energy of the disordered system as a function of concentration x in the site and captures any asymmetry in the system:

$$\text{Margules term} = E_0 = x(1-x)(m_1x+m_2(1-x) \quad (3.3)$$

The total energy for a given configuration is equal to the sum of the Margules energy (composition-dependent) and interaction energy (configuration-dependent):

$$E_{config} = E_0 + \sum_i (n_i J_i) \quad (3.4)$$

The sum (second term in Eqn.(4)) then describes how favorable or unfavorable a specific configuration is with respect to the disordered energy E_0. During the fitting, the Margules function is restricted to the approximate range of energies calculated directly using DFT/LDA in order to ensure decrease the likelihood of an unphysical calculated energy E_{config}. Final fitted *J*'s and Margules parameters are given in Table 3.3. A more detailed explanation of the *J*-formalism may be found elsewhere (Dove 1999; Becker et al. 2000; Vinograd et al. 2004).

Table 3.3. Fitted Margules parameters (m_1 and m_2) and interaction parameters* (*J*'s) in kJ/mol in zircon-structured solid solutions (A,B)SiO_4 fitted to n number of intermediate configurations.

cations	n	m_1	m_2	$J\,i$=1	$J\,i$=2	$J\,i$=3	$J\,i$=4	r^2 †
Hf, Zr	27	2.91	2.5	-0.001	0.001	-0.001	0.002	0.99
Pu, Zr	19	35	45	0.282	-0.018	-0.018	-0.064	0.99
Pu, Hf	22	65	45	0.328	-0.011	-0.046	0.177	0.99
U, Zr	22	60	80	0.484	-0.061	-0.166	-0.122	0.99
Th, Zr	26	112.5	136.5	0.140	-0.074	-0.145	0.070	0.99
U, Th	22	20	25	0.140	0.000	0.154	-0.099	0.98
Ce, Zr	24	58	64	0.068	-0.041	-0.085	0.027	1.00

* The interaction types *i* are defined in Table 3.2.
† The goodness of fit between the fitted and original calculated energies is indicated by the correlation coefficient r^2.

3.4c. Thermodynamic properties from Monte-Carlo simulations and subsequent thermodynamic integration

For each step (out of up to millions for one given starting configuration) in the Monte-Carlo algorithm, two cations in the 8 × 8 × 8 supercell are chosen at random and swapped. The energy of the new configuration is calculated using equation (1) and the swap is accepted if either (1) the difference between the new energy and the energy of the previous configuration (ΔE_{swap}) is negative or (2) the probability of the swap is greater than a random number between 0 and 1. The probability P is determined by the Boltzmann factor:

$$P = \exp\left(\frac{-\Delta E_{swap}}{k_B T}\right) \tag{3.5}$$

where k_B is the Boltzmann factor (1.3807×10^{-23} J/K) and T is temperature. All exchangeable atoms are taken as potential swap partners in order to increase the likelihood of the system reaching equilibrium. This Monte-Carlo simulation is allowed to continue until at least 200,000 swaps have been successfully completed at temperatures ranging from 1500 K to 100 K. Radiation-damage effects may limit the temperature range at which actinide-bearing $ZrSiO_4$ is stable to roughly 700 – 900 K (Meldrum et al. 1998; 1999), but this effect is not considered here. The calculations follow an annealing path from high temperature to low temperature, and the initial configuration at a given temperature is taken as the final configuration from the previous (higher) temperature. After equilibration over at least 100,000 successful steps, the energies of the final 100,000 successful swaps are averaged to determine the excess enthalpy of mixing (ΔH_{mixing}). ΔG_{mixing} may then be estimated using

thermodynamic integration, which is typically expressed in terms of the Helmholtz free energy, F, which at 0 GPa pressure is equivalent to G:

$$F = -T\Delta S_{pt} + \int_0^1 \langle H \rangle_\lambda \, d\lambda \tag{3.6}$$

where λ is the mixing or control parameter, which varies from 0 to 1, and $\langle H \rangle_\lambda$ is the average energy of the system subject to the Hamiltonian λH (Dove 2001). These average energies are obtained from the Monte Carlo simulation. The point entropy, ΔS_{pt}, is the entropy of the system in a state of complete disorder:

$$\Delta S_{pt} = -R[x \ln x + (1-x)\ln(1-x)] \tag{3.7}$$

where R is the gas constant 8.3145 J/(mol K). Energy contributions from configurational entropy are taken into account by the J's and Monte-Carlo energy calculations. Calculation of the total excess entropy of mixing, ΔS_{mixing}, is then straightforward:

$$\Delta S_{excess} = \frac{\Delta H_{excess} - \Delta G_{excess}}{T} \tag{3.8}$$

The excess thermodynamic properties calculated are based only on differences in chemistry and bonding environments. Any contributions to excess properties related to changes in vibrational entropies, zero-point energies, or non-harmonic contributions are neglected. However, these other excess properties typically only change the excess free energy by a few percent (Becker and Pollok 2002). Additional descriptions of Monte-Carlo methods applied to cation ordering and thermodynamic integration may be found in (Yeomans 1992; Myers 1998; Warren et al. 2001).

3.5. Results

ΔH_{mixing}, ΔG_{mixing}, and ΔS_{mixing} were calculated for each solid solution based on fitted *J* values and Margules parameters (Table 3.3). Examples of these are shown for the near-ideal solid solution (Hf,Zr)SiO_4 (Figure 3.2), the limited solid solution (U,Th)SiO_4 (Figure 3.3) and the very limited solid solution (Th,Zr)SiO_4 (Figure 3.4). Note the differences in scale for each figure.

Calculated volumes agree with experimental results to within 4 % for solid solution end-member and to within 8 % for related oxides (Table 3.4), which means that calculated and experimental unit cell parameters typically agree by approximately 1 %. Final unit cell parameters and volumes are consistently underestimated, which is typical for quantum-mechanical calculations using the local density approximation (Cohen 2000). The calculated unit cell parameters and $\langle cation - O \rangle$ bond-lengths (Figure 3.5) are in agreement with previous observations of increasing size with increasing ionic radius (Speer and Cooper 1982). The relations of **a**, **c**, shared $\langle O - O \rangle$ edge length, and the two types of $\langle cation - O \rangle$ bond-lengths to the cation radius are close to linear, with correlation coefficients of 0.96 or greater. Calculated unit cell parameters and molar volumes change regularly with composition. Figure 3.6 shows this relation for the (Zr,Hf)SiO_4 and (Zr,Pu)SiO_4 solid solutions. There is no correlation between the average excess structural parameters as a function of cation size or size differences. Excess unit cell parameter values were typically less than 0.02 Å, and the absolute values of most excess volumes did not exceed 0.015 cm^3/mol. Low excess volumes suggest that the internal stress on the

structure is small, but these calculations do not take into account the large amount of swelling (18 %) associated with radiation-damage effects (Weber 1991; Weber et al. 1998; Lumpkin 2006).

Table 3.4 Calculated energies and percent volume errors for solid solution end-members and related oxides.

composition	mineral name	space group	% volume error	stability	reference
$ZrSiO_4$	zircon	$I4_1/amd$	0.00	stable	(Robinson et al. 1971)
$PuSiO_4$	(none)	$I4_1/amd$	-2.34	unstable	(Keller 1963)
$USiO_4$	coffinite	$I4_1/amd$	-3.60	unstable	(Fuchs and Gebert 1958)
$ThSiO_4$	thorite	$I4_1/amd$	-1.29	stable*	(Keller 1963)
$ThSiO_4$	huttonite	$P2_1/n$	-1.97	unstable *	(Taylor and Ewing 1978)
$HfSiO_4$	hafnon	$I4_1/amd$	-2.57	stable	(Speer and Cooper 1982)
$CeSiO_4$	(none)	$I4_1/amd$	-0.98	unstable	(Skakle et al. 2000)
ZrO_2	baddeleyite	$P2_1/c$	-2.45	-	(McCullough and Trueblood 1959)
PuO_2	(none)	$Fm3m$	-6.80	-	(Wyckoff 1963)
UO_2	uraninite	$Fm3m$	-7.86	-	(Wyckoff 1963)
ThO_2	thorianite	$Fm3m$	-2.25	-	(Wyckoff 1963)
HfO_2	(none)	$Fm3m$	-7.55	-	(Wyckoff 1963)
CeO_2	cerianite	$Fm3m$	-2.48	-	(Levien et al. 1980)
SiO_2	quartz	$P3_221$	0.77	-	(Wyckoff 1963)

* see text for discussion

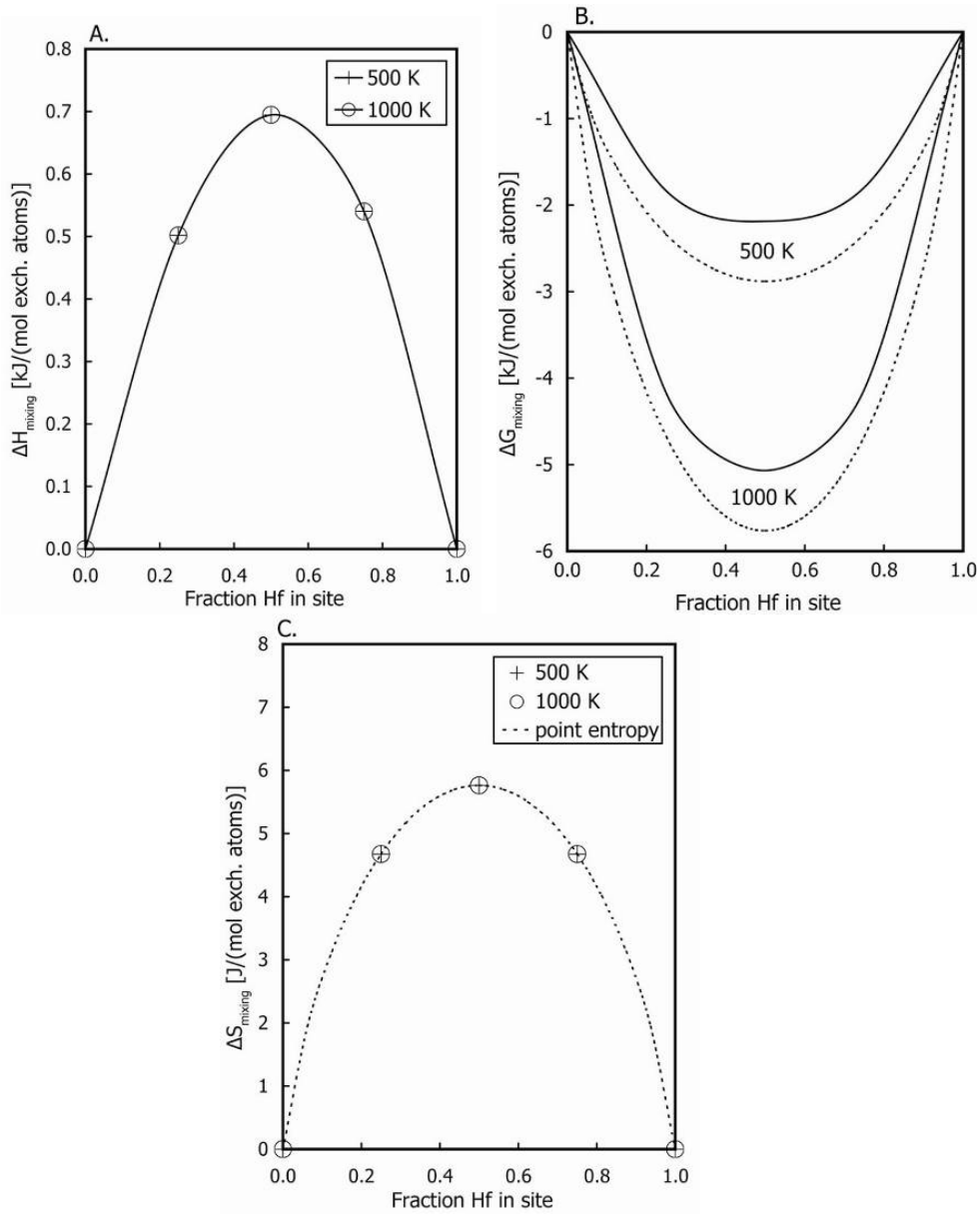

Figure 3.2. Excess thermodynamic enthalpy ΔH_{mixing} (a), free energy ΔG_{mixing} (b), and entropy ΔS_{mixing} (c) for $(Zr,Hf)SiO_4$. The dashed lines in (b) show ΔG_{mixing} values for an ideal solid solution.

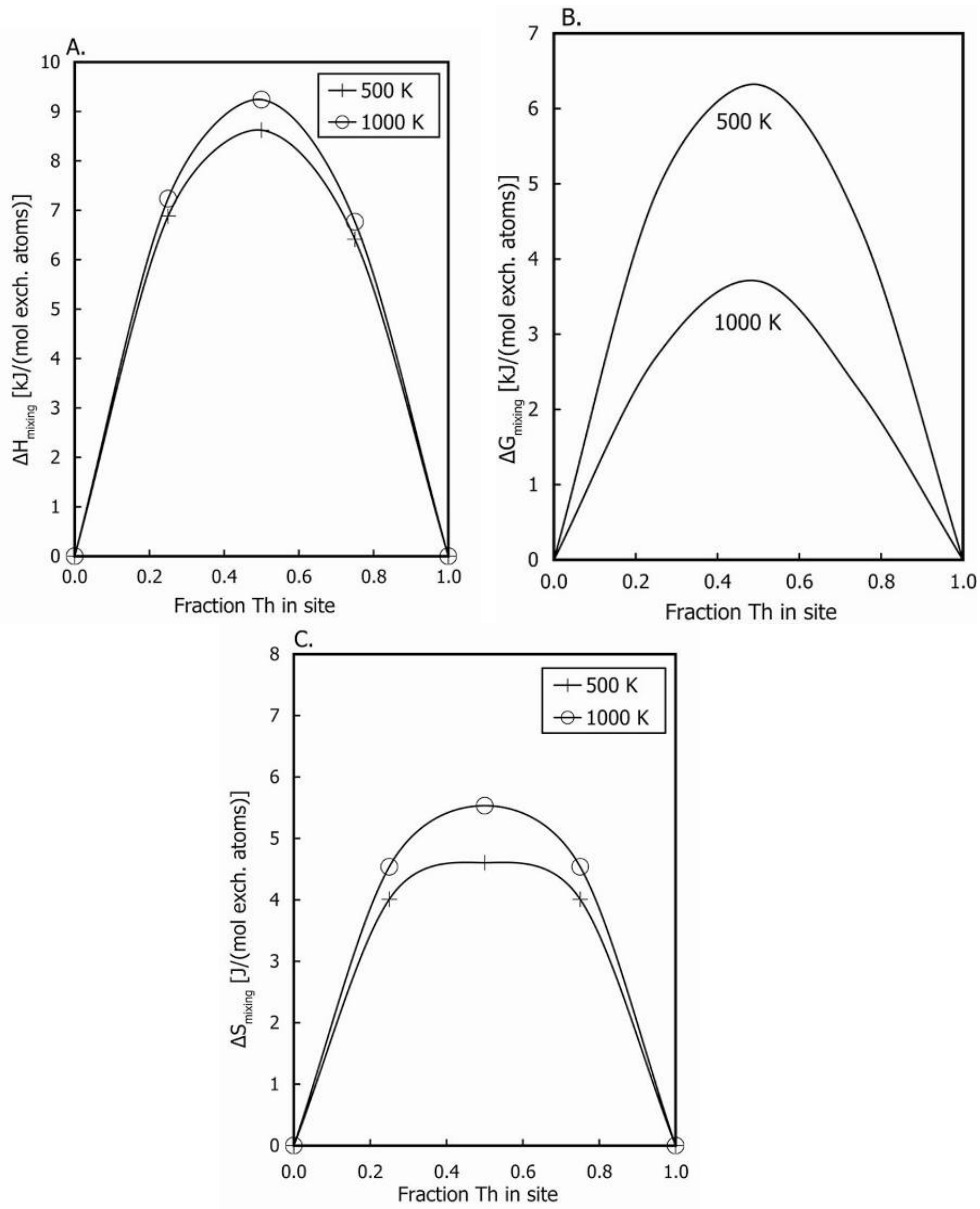

Figure 3.3. Excess thermodynamic enthalpy ΔH_{mixing} (a), free energy ΔG_{mixing} (b), and entropy ΔS_{mixing} (c) for (U,Th)SiO_4.

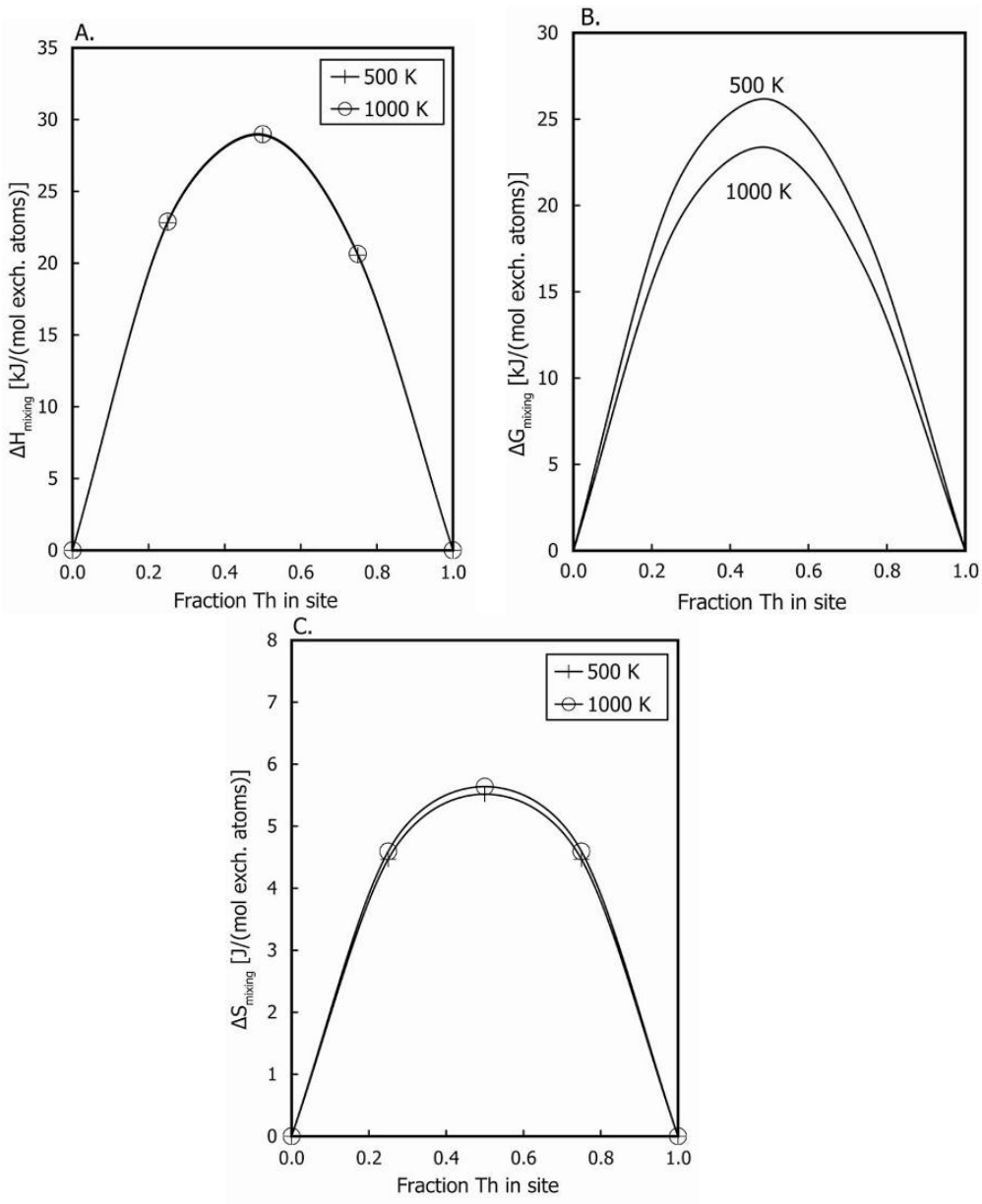

Figure 3.4. Excess thermodynamic enthalpy ΔH_{mixing} (a), free energy ΔG_{mixing} (b), and entropy ΔS_{mixing} (c) for $(Zr,Th)SiO_4$.

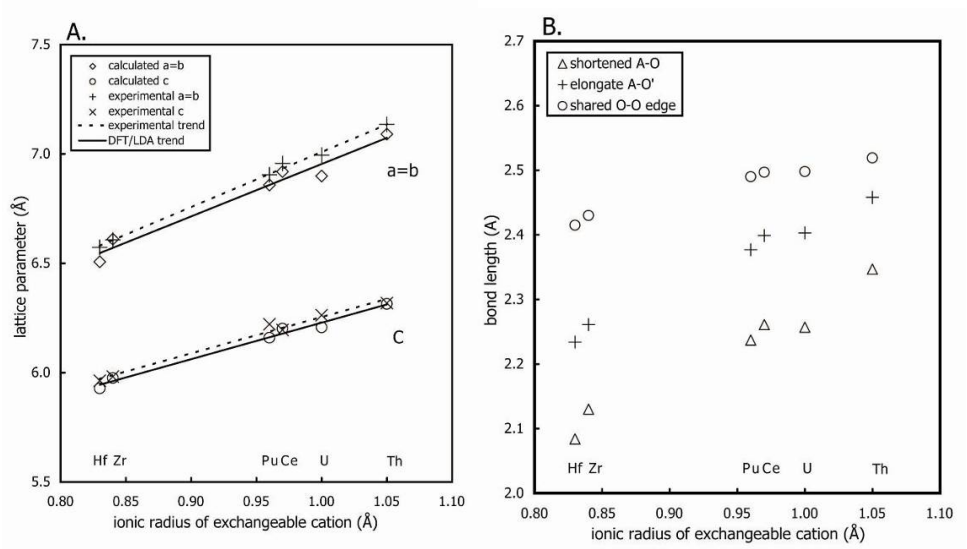

Figure 3.5. Relationship between ionic radius of the cation A in the octahedral site of the zircon-structured compound $ASiO_4$ and the unit cell parameters (a) and calculated site size (b). The octahedral site consists of four shorter A-O bonds and four elongate A-O' bonds. The elongated tetrahedron includes a shared edge between the Zr polyhedron and Si tetrahedron. Ionic radii are taken from (Shannon 1976), and references for experimental data are given in Table 3.4.

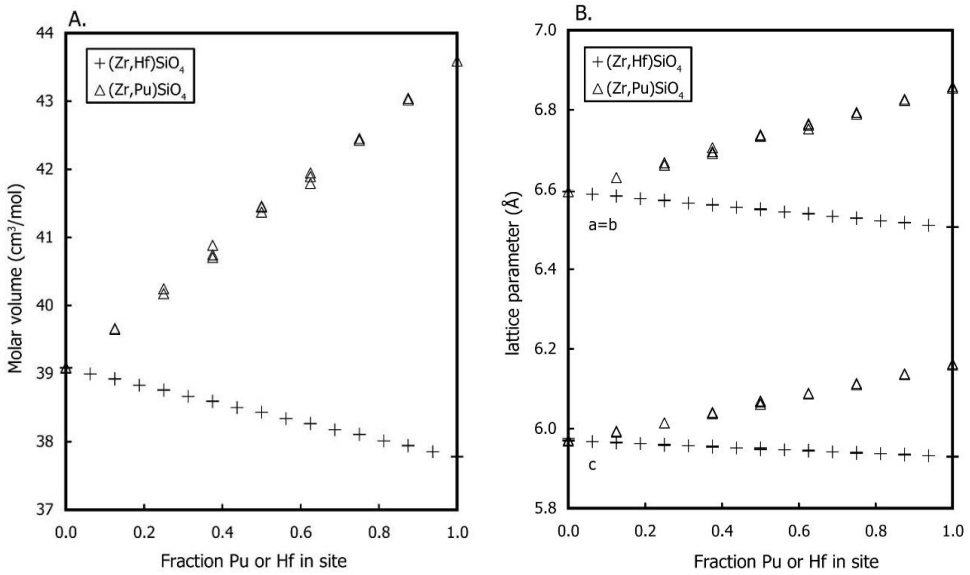

Figure 3.6. Molar volume (a) and unit cell parameters (b) as a function of composition for the $(Zr,Hf)SiO_4$ solid solution. Each point represents one configuration calculated using quantum mechanics.

3.6. Discussion

3.6a. Miscibility trends and bonded radii

The overall shape of the ΔH_{mixing} curves is, to a significant degree, described by Margules energy, $E_{0,}$ (equation (3)), which represents the best fit to the portion of the VASP excess energy without consideration of configurational differences. E_0 may also be thought of as the energy of a completely disordered system in which all possible Monte Carlo swaps are accepted (either by applying very high temperature or by all *J*'s being equal to 0). The lower the absolute value of the fitted *J*'s (Table 3.3), the less pronounced is the effect of configuration on the total energy for a given composition. The maximum absolute value of a J parameter fitted for any solid solution is 0.66 kJ/mol. Typical J values fitted to other solid solutions range in absolute value from 0.05 to 20.0 kJ/mol (Becker et al. 2000; Becker and Pollok 2002; Vinograd et al. 2004). The E_0 term then is the enthalpy of the system in a state of complete disorder and may be used to compare solid solutions (Figure 3.7).

The relative stability of each solid solution may also be predicted using a comparison of the volume mismatch parameter, ΔV,for different solid solutions:

$$\Delta V = \frac{abs(V_1 - V_2)}{V_{\bar{12}}} \tag{3.9}$$

where V_1 and V_2 are the volumes of the two end-members and $V_{\bar{12}}$ is the mean of the two. A larger ΔV is associated with a greater deviation of the intermediate compositions from ideality (Davies and Navrotsky 1983). The energy trends shown in Figure 3.7 correlate well with the trends in ΔV (Table 3.5).

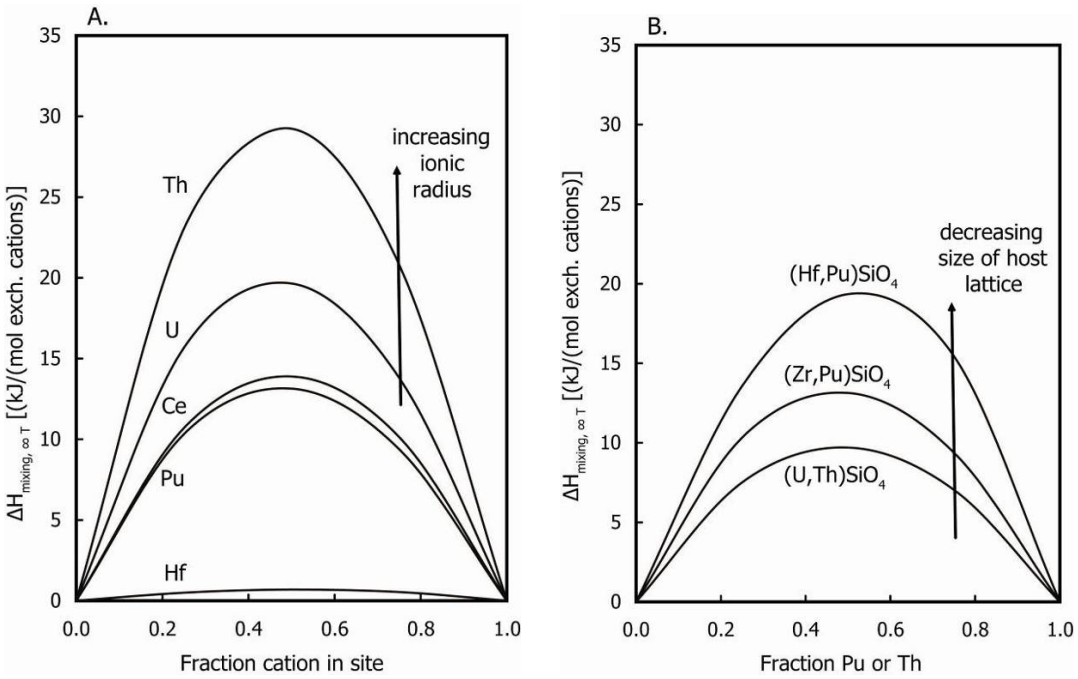

Figure 3.7. Excess enthalpies of mixing of completely disordered systems for (a) solid solutions with end-member $ZrSiO_4$ and (B) other zircon-structured solid solutions with $(Zr,Pu)SiO_4$ included as reference.

Table 3.5. Volume mismatch parameter ΔV for zircon-structured solid solutions $(Y,Z)SiO_4$. References are given in Table 3.4.

Y, Z	ΔV
Th, Zr	0.21
U, Zr	0.16
Hf, Pu	0.15
Ce, Zr	0.14
Pu, Zr	0.13
U, Th	0.05
Pu, U	0.03
Hf, Zr	0.01

The observed trend in miscibility is often described in terms of trends of the ionic radii (*e.g.,* (Speer and Cooper 1982)). However, standard ionic or crystal radii are tabulated by assuming all ions form perfect spheres and do describe any differences in shape and bonding among different cations in the orthosilicate

structure. The actual bonded radii of the cations may be measured in any direction using the charge density isosurfaces, which are shown in Figure 3.8 for two examples structures, $PuSiO_4$ and $CeSiO_4$, projected on [001] and [100]. The isosurface of Ce is more box-like in shape, especially projected onto [001], while Pu is more rounded. The average bonded radius for all elements considered in $ASiO_4$, which has the zircon structure, are on average 0.3 Å larger than the standard crystal radii compiled in (Shannon 1976) (Table 3.6).

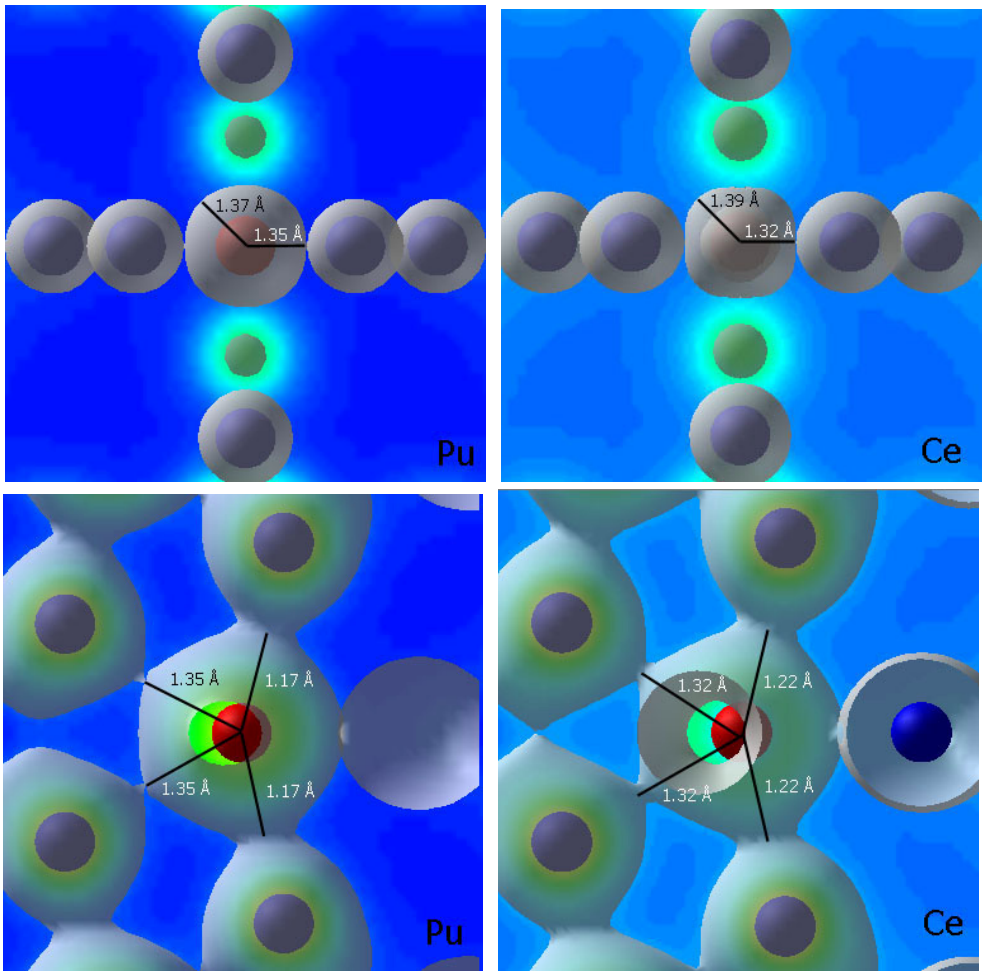

Figure 3.8. Charge density isosurfaces projected on (a) [001] and (b) [100] for Pu and Ce (red) coordinated by eight oxygen atoms (blue). Pu appears to be more rounded than Ce in this structure, and the bonded ionic radius of Pu is slightly larger than that of Ce in the elongate O-cation bonds.

Table 3.6. Tabulated average crystal radii (Shannon 1976), bond lengths to nearest O and second nearest oxygen O', and calculated bonded ionic radii (BIR) for cation A in $ASiO_4$ with the zircon structure. All units in Å.

Y	Shannon	$\langle Y-O \rangle$	$\langle Y-O' \rangle$	BIR $\langle Y-O \rangle$	BIR $\langle Y-O' \rangle$	BIR_{ave}	BIR_{ave}-Shannon
Hf	0.83	2.08	2.23	1.07	1.15	1.11	0.28
Zr	0.84	2.13	2.26	1.12	1.30	1.21	0.37
Pu	0.96	2.24	2.38	1.17	1.35	1.26	0.30
Ce	0.97	2.26	2.40	1.22	1.32	1.27	0.30
U	1.00	2.26	2.40	1.22	1.32	1.27	0.27
Th	1.05	2.35	2.46	1.24	1.31	1.28	0.23

3.6b. Estimates of miscibility and end-member stability

ΔG_{mixing} curves indicate nearly ideal substitutional solid solution for $(Zr,Hf)SiO_4$ but very large miscibility gaps and solubility limits below 3 mol% (the lowest concentration considered in the calculations) at most temperatures. Even for systems such as $(Th,U)SiO_4$ with relatively low ΔH_{mixing} curves at infinite temperature (Figure 3.7), the tangents to the ΔG_{mixing} curve, which define the solvus, were not observed at the concentration resolution of this study (Figure 3.3B). The maximum fraction, x_{inc}, of solute atoms A that may be incorporated into the structure of $BSiO_4$ for a solid solution composition of $A_xB_{(1-x)}SiO_4$ may be estimated using the calculated excess thermodynamic mixing values (Ferriss et al. 2008):

$$x_{inc} = \frac{e^{\left(\frac{\Delta H_1}{X_1}\right)\left(\frac{1}{RT}\right)}}{1+e^{\left(\frac{\Delta H_1}{X_1}\right)\left(\frac{1}{RT}\right)}} \qquad (3.10)$$

where ΔH_1 is the calculated excess enthalpy at temperature, T, for x_1, the lowest fraction of x considered in the Monte Carlo evaluation of the solid solution $A_xB_{(1-x)}SiO_4$ (here x_1=0.03). Equation (9) approximates the entropy as a point entropy near the edges ($x \approx 0$ and $x \approx 1$). Table 3.1 includes x_{inc} for the solid solutions of interest at 1000 K. Table 3.1 also illustrates the asymmetry of each solid-solution system. In all

cases, substitution is more extensive when the smaller exchangeable cation is substituted into a host structure with larger cations. This difference is common in many systems and has been attributed to the difference in cation size (Davies and Navrotsky 1983). Miscibility trends based on x_{inc} estimates are in general agreement with the predictions made using ΔH_{mixing} curves at infinite temperature and ΔV, except for the $CeSiO_4$-$ZrSiO_4$ system, which has the narrowest predicted solvus at 1000 K.

Calculated estimates of the amount of actinides and Ce that may be incorporated into the zircon structure are strikingly low as compared with concentrations in natural and synthetic samples (Table 3.1). This difference may be due to error and oversimplifications made in the calculations, persistent metastable intermediates in nature and/or experiments, or both. Error associated with the calculations may be related to (1) insufficient or unrepresentative configuration sampling when determining excess energies using quantum mechanics, (2) inaccuracies in the quantum mechanical values, (3) the fitting approach and goodness of fit between the interaction and Margules parameters and the excess energies, and (4) insufficient number of attempted cation pair swaps (200,000 in an $8 \times 8 \times 8$ supercell) to reach equilibrium. A thorough analysis of the error in the calculations would involve re-calculating each step of the analysis using multiple techniques. The calculations also consider only anhydrous binary systems. As noted in the above discussion of zircon solid solutions in nature and experiments, H_2O, $(OH)^-$, and the incorporation of multiple end-members may be important in stabilizing the structure, and the wide miscibility gaps in the calculations may be narrowed in the presence of

other impurity elements. Metastable equilibrium states have been noted as common and persistent in zircon solid solutions (Mumpton and Roy 1961), further complicating any comparisons. Another possibility is that the natural and experimental samples were not true solid solutions, but included lamellae or inclusions too small to be resolved by the analytical techniques used. Zoned Ca-rich garnets, for example, have been described with lamellae as small as 10 nm (Pollok et al., 2001).

All calculations assume the thermodynamic stability of both end-members, but this is not necessarily the case. Table 3.4 includes the calculated ground-state energies of all solid solution end-members at 0 K. These energies, *E*, were compared to the energy of the constituent oxides (*e.g.*, $E_{ZrSiO_4} - E_{ZrO_2} - E_{SiO_2}$) in order to estimate the thermodynamic stability of each end-member at 0 K and 0 GPa. Zircon and hafnon, which are common in nature, are stable relative to the oxides. The actinide silicates $USiO_4$, $PuSiO_4$, and $CeSiO_4$ are predicted to be unstable relative to their respective oxides. The metastability of $USiO_4$ with respect to oxides may explain why coffinite has been relatively difficult to synthesize (Pointeau et al. 2009). The stability of the two polymorphs of $ThSiO_4$, tetragonal thorite and monoclinic huttonite, with respect to their oxides is not well established (Konings et al. 2008). Results of DFT with LDA suggest that thorite is marginally stable (-1.0 kJ/mol difference), huttonite is marginally unstable (1.6 kJ/mol), and thorite is the preferred phase by 2.6 kJ/mol at 0 K.

In order for an intermediate composition of a solid solution containing $CeSiO_4$, $USiO_4$, or $PuSiO_4$ to be stable, the chemical potential of an intermediate must

be less than other possibilities, including a mechanical mixture of end-members (as in Figure 3.2, 3.3, and 3.4) or a mixture of constituent oxides (Figure 3.9). Thus, an accurate phase diagram for $ZrSiO_4$-$PuSiO_4$ would include only the constituent oxides of the unstable end-member (Figure 3.10). In a real assemblage AO_2 + SiO_2 + $(B,A)SiO_4$, the oxide AO_2 would also be expected to contain a small amount of B. A long-term, stable waste loading of Pu as $PuSiO_4$ in solid solution with $ZrSiO_4$ is unlikely to be possible above a few mol%, in part because of the inherent instability of $PuSiO_4$. A solid solution between two metastable phases (*e.g.*, $(Pu,U)SiO_4$) will not be thermodynamically stable at any composition.

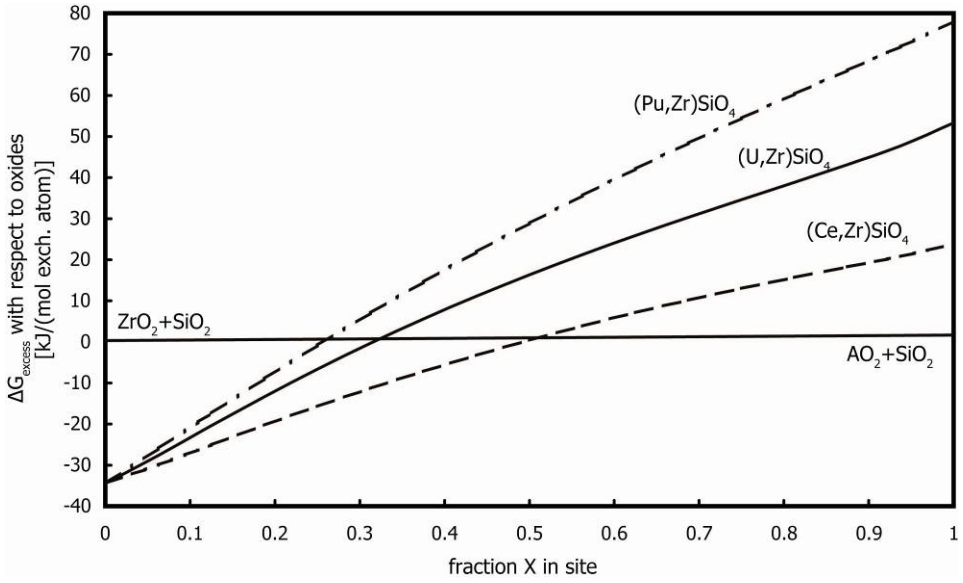

Figure 3.9. ΔG_{mixing} curves at 3000 K for $(A,Zr)SiO_4$ solid solutions where A=Pu, U, or Ce showing stability relative to constituent oxides. The SiO_2 phase is assumed to be quartz, and ZrO_2 is baddeleyite.

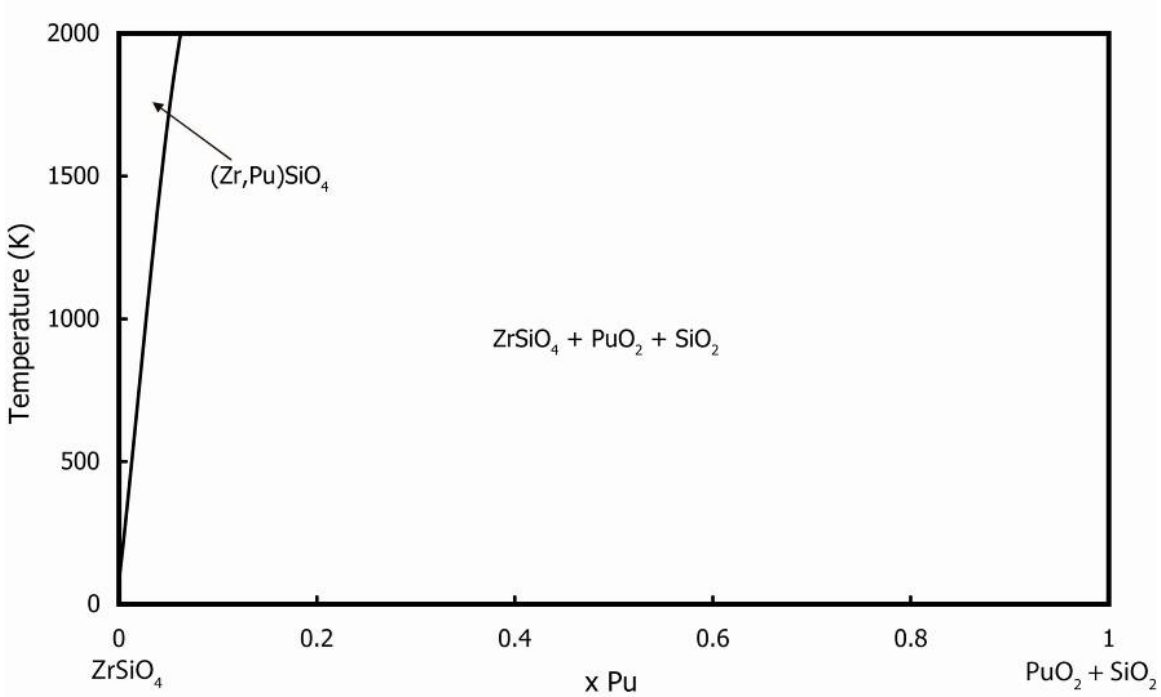

Figure 3.10. Phase diagram for the $ZrSiO_4$-$PuSiO_4$ system. $PuSiO_4$ is unstable relative to crystalline PuO_2 and $SiO_{2(quartz)}$.

3.6c. Exsolution

Solid-state exsolution textures are almost never reported in zircon (Geisler et al. 2007), most likely because of slow cation diffusion at crustal temperatures (Cherniak et al. 1997a). Some thorite inclusions in a Nigerian zircon have been interpreted as the product of exsolution (Pointer et al. 1988b), and structural strain has been noted in high-U content zircon (up to 11.6 mol% $USiO_4$) formed during the Chernobyl nuclear power plant accident in 1986 (Geisler et al. 2005). Monte-Carlo simulations show exsolution at equilibrium for all binaries considered except hafnon-zircon (Figure 3.11). No short-range ordering schemes are evident for any of the intermediate compositions at any temperature.

The differences in exsolution behavior in these systems follow from the differences in fitted interaction parameters (*J*'s) (Table 3.3). The $(Zr,Hf)SiO_4$ solid

solution has very low calculated excess energies and J's, indicating very small energy differences among possible cation arrangements at any temperature (Figure 3.11 F). In contrast, the (Zr,Pu)SiO_4 has relatively large absolute values for the *J*'s, and the largest (*J* for *i*=1) is positive, indicating a preference for homo-cationic (*e.g.* Pu-Pu) interactions. As a result, exsolution textures are observed at equilibrium, even at the very low temperature of 100 K (Figure 3.11 A and B). The (Zr,U)SiO_4 and (U,Th)SiO_4 systems show very similar results to (Zr,Pu)SiO_4. The increase in exsolution at low temperatures corresponds to a decrease in the ΔS_{mixing} curve for these solid solutions (Figure 3.3 C). The (Zr,Ce)SiO_4 and (Zr,Th)SiO_4 systems are also similar but with some differences. (Zr,Ce)SiO_4 show a clear exsolution pattern at 100 K, but at high temperatures (1000 K) there was no evident ordering. In (Zr,Th)SiO_4 the high temperature exsolution is apparent, but the lamellae are thinner (Figure 3.11 E). Surprisingly, the (Zr,Th)SiO_4 at low temperatures appears similar to that of (Zr,Hf)SiO_4, suggesting a lack of strong preference for cation-cation arrangement. The (Hf,Pu)SiO_4 system is distinguished by a large positive *J* for *i*=4, the interaction type parallel to z. This strong preference for homocationic interactions in the z-direction is evident in the low-temperature exsolution textures that are perpendicular to the lamellae observed in other systems (Figure 3.11 D).

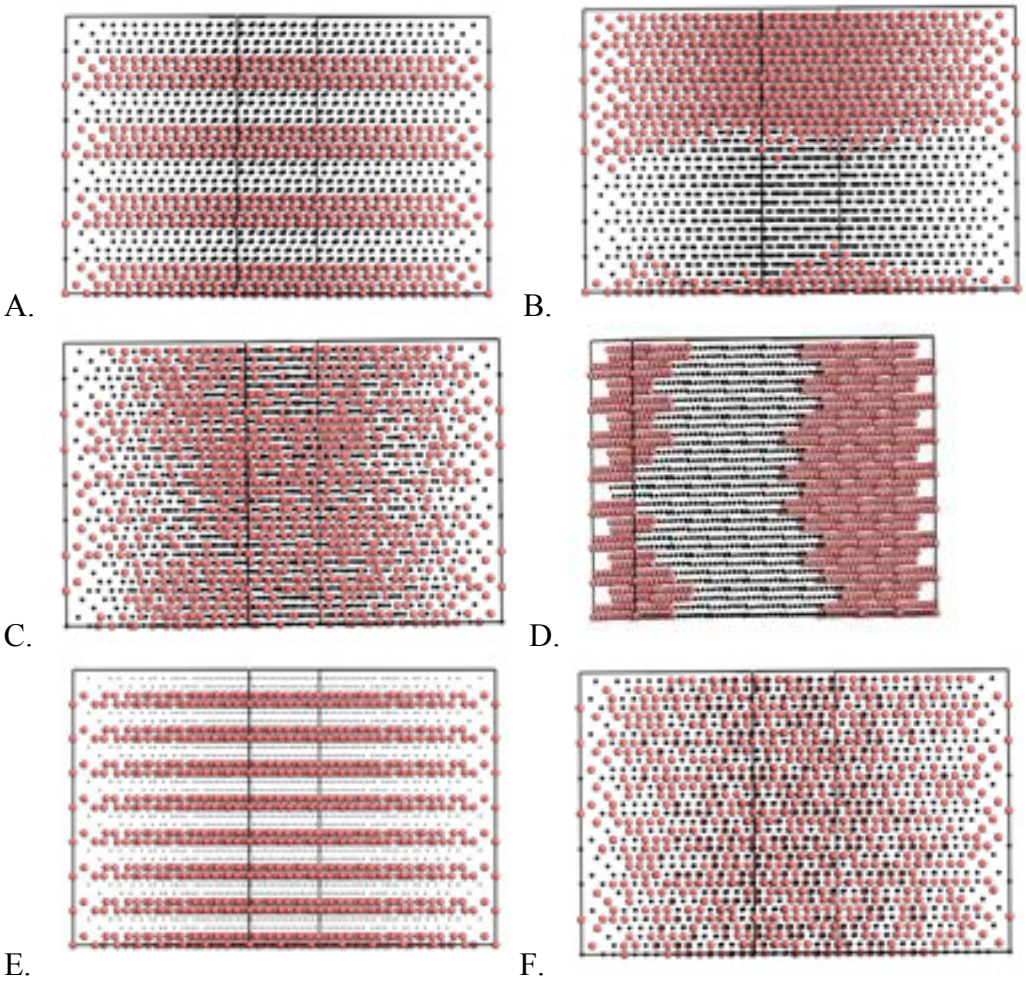

Figure 3.11. Ordering and exsolution patterns in an 8 × 8 × 8 supercell (each side is ~50 Å long) for different solid solutions $A_xB_{(1-x)}SiO_4$ at x=0.5. The z direction is oriented vertically in the plane of the paper (up-down) in all cases. Pink circles and black dots represent the two types of exchangeable cations A and B. Si and O are not shown. (a) $Zr_{0.5}Pu_{0.5}SiO_4$ at 1000 K, (b) $Zr_{0.5}Pu_{0.5}SiO_4$ at 100 K, (c) $Hf_{0.5}Pu_{0.5}SiO_4$ at 1000 K, (d) $Hf_{0.5}Pu_{0.5}SiO_4$ at 100 K, (E) $Zr_{0.5}Th_{0.5}SiO_4$ at 1000 K, (f) $Zr_{0.5}Hf_{0.5}SiO_4$ at 100 K.

3.7. Conclusions

This study used density functional theory, Monte Carlo simulations, and thermodynamic integration to model seven orthosilicate solid solutions. $ZrSiO_4$ and $HfSiO_4$ were determined to form a near-ideal solid solution. The extent of solid solution for the anhydrous systems $(Zr,Ce)SiO_4$, $(Zr,Pu)SiO_4$, $(Zr,U)SiO_4$,

$(Zr,Th)SiO_4$, $(Hf,Pu)SiO_4$, and $(U,Th)SiO_4$ was determined to be limited to a few mole percent, even at high temperatures. Miscibility trends correlate well with experimental results and the volume mismatch between end-members, although calculated solvi are much wider than what would be expected from nature and experimental work. Quantum mechanical energy comparisons indicate that the end-members $CeSiO_4$, $USiO_4$, and $PuSiO_4$ are unstable relative to their constituent oxides $(Ce/U/Pu)O_2$ and $SiO_{2(quartz)}$, further limiting the predicted extent of solid solution in these systems. Long-term waste loading of Pu as $PuSiO_4$ in solid solution with $ZrSiO_4$ is unlikely to be possible above a few mol %, in part because of the inherent instability of $PuSiO_4$.

3.8. References

Anderson, E.B., Burakov, B.E., and Pazukhin, E.M. (1993) High-uranium zircon from Chernobyl lavas. Radiochimica Acta, 60, 149-151.

Babsail, L., Hamelin, N., and Townsend, P.D. (1991) Helium-ion implanted waveguides in zircon. Nuclear Instruments and Methods in Physics Research, 859, 1219-1225.

Becker, U., Fernandez-Gonzalez, A., Prieto, M., Harrison, R., and Putnis, A. (2000) Direct calculation of thermodynamic properties of the barite/celestite solid solution from molecular principles. Physics and Chemistry of Minerals, 27, 291-300.

Becker, U., and Pollok, K. (2002) Molecular simulations of interfacial and thermodynamic mixing properties of grossular-andradite garnets. Physics and Chemistry of Minerals, 29, 52-64.

Begg, B.D., Hess, N.J., Weber, W.J., Conradson, S.D., Schweiger, M.J., and Ewing, R.C. (2000) XAS and XRD study of annealed Pu-238- and Pu-239-substituted zircons ($Zr_{0.92}Pu_{0.08}SiO_4$). Journal of Nuclear Materials, 278, 212-224.

Bhushan, B., and Sen, S. (1965) Zircon glazes. Transactions of the Indian Ceramic Society, 12(2).

Bosenick, A., Dove, M.T., Myers, E.R., Palin, E.J., Sainz-Diaz, C.I., Guiton, B.S., Warren, M.C., Craig, M.S., and Redfern, S.A.T. (2001) Computational methods for the study of energies of cation distributions: applications to cation-ordering phase transitions and solid solutions. Mineralogical Magazine, 65(2), 193-219.

Burakov, B.E., Anderson, E.B., Galkin, B.Y., Starchenko, V.A., and Vasiliev, V.G. (1996) The crystalline host-phases for immobilization of weapons plutonium and waste actinides. Disposal of Weapon Plutonium - Approaches and Prospects, 4, 85-89.

Burakov, B.E., Anderson, E.B., Zamoryanskaya, M.V., Yagovkina, M.A., Strykanova, E.E., and Nikolaeva, E.V. (2000) Synthesis and study of Pu-239-doped ceramics based on zircon, $(Zr,Pu)SiO_4$, and hafnon, $(Hf,Pu)SiO_4$. Scientific Basis for Nuclear Waste Management Xxiv, 663, 307-313.

Burakov, B.E., Hanchar, J.M., Zamoryanskaya, M.V., Garbuzov, V.M., and Zirlin, V.A. (2002) Synthesis and investigation of Pu-doped single crystal zircon, $(Zr, Pu)SiO_4$. Radiochimica Acta, 90(2), 95-97.

Burakov, B.E., Yagovkina, M.A., Zamoryanskaya, M.V., Garbuzov, V.M., Zirlin, V.A., and Kitsay, A.A. (2008) Self-irradiation of ceramics and single crystals doped with Pu-238: Summary of 5 years of research of the V. G. Khlopin radium institute. Scientific Basis for Nuclear Waste Management XXXI, 381-388.

Cao, X.Q., Vassen, R., and Stoever, D. (2004) Ceramic materials for thermal barrier coatings. Journal of the European Ceramic Society, 24, 1-10.

Cherniak, D.J., Hanchar, J.M., and Watson, E.B. (1997a) Diffusion of tetravalent cations in zircon. Contributions to Mineralogy and Petrology, 127, 383-390.

-. (1997b) Rare-earth diffusion in zircon. Chemical Geology, 134, 289-301.

Cohen, R.E. (2000) Theory of ferroelectrics: a vision for the next decade and beyond. Journal of Physics and Chemistry of Solids, 61(2), 139-146.

Davies, P.K., and Navrotsky, A. (1983) Quantitative Correlations of Deviations from Ideality in Binary and Pseudobinary Solid-Solutions. Journal of Solid State Chemistry, 46, 1-22.

Dove, M.T. (1999) Order/disorder phenomena in minerals: ordering phase transitions and solid solutions. In K. Wright, and R. Catlow, Eds. Microscopic properties and processes in minerals, C543, p. 451-475. NATO Science Series, Kluwer Academic Publishers, Dordrecht, The Netherlands.

-. (2001) Computer simulations of solid solutions. In C.A. Geiger, Ed. Solid solutions in silicate and oxide systems, 3, p. 225-250. Eötvös University Press, Budapest.

Ewing, R.C., Lutze, W., and Weber, W.J. (1995) Zircon - a host-phase for the disposal of weapons plutonium. Journal of Materials Research, 10, 243-246.

Farnan, I., Cho, H., and Weber, W.J. (2007) Quantification of actinide alpha-radiation damage in minerals and ceramics. Nature, 445, 190-193.

Ferriss, E.D.A., Essene, E.J., and Becker, U. (2008) Computational study of the effect of pressure on the Ti-in-zircon geothermometer. European Journal of Mineralogy, 20, 745-755.

Finch, R.J., and Hanchar, J.M. (2003) Structure and chemistry of zircon and zircon-group minerals. In J.M. Hanchar, and P.W.O. Hoskin, Eds. Zircon, 53, p. 1-21. Mineralogical Society of America, Washington, D.C.

Finch, R.J., Hanchar, J.M., Hoskin, P.W.O., and Burns, P.C. (2001) Rare-earth elements in synthetic zircon: Part 2. A single-crystal X-ray study of xenotime substitution. American Mineralogist, 86(5-6), 681-689.

Fuchs, L.H., and Gebert, E. (1958) X-Ray studies of synthetic coffinite, thorite and uranothorites. American Mineralogist, 43, 243-248.

Geisler, T., Burakov, B., Yagovkina, M., Garbuzov, V., Zamoryanskaya, M., Zirlin, V., and Nikolaeva, L. (2005a) Structural recovery of self-irradiated natural and Pu-238-doped zircon in an acidic solution at 175 °C. Journal of Nuclear Materials, 336(1), 22-30.

Geisler, T., Burakov, B.E., Zirlin, V., Nikolaeva, L., and Poml, P. (2005b) A Raman spectroscopic study of high-uranium zircon from the Chernobyl "lava". European Journal of Mineralogy, 17(6), 883-894.

Gibb, F.G.F., Taylor, K.J., and Burakov, B.E. (2008) The 'granite encapsulation' route to the safe disposal of Pu and other actinides. Journal of Nuclear Materials, 374(3), 364-369.

Grover, V., Chakraborty, K.R., and Tyagi, A.K. (2005) Structural elucidation of stabilized tetragonal $ThSiO_4$: A neutron diffraction study. Powder Diffraction, 20(3), 215-217.

Grover, V., and Tyagi, A.K. (2005) Preparation and bulk thermal expansion studies in $M_{1-x}Ce_xSiO_4$ (M = Th, Zr) system, and stabilization of tetragonal $ThSiO_4$. Journal of Alloys and Compounds, 390, 112-114.

Hanchar, J.M., Burakov, B.E., Anderson, E.B., and Zamoryanskaya, M.V. (2003) Investigation of single crystal zircon, $(Zr,Pu)SiO_4$, doped with Pu-238. Scientific Basis for Nuclear Waste Management XXVI, 215-225.

Hanchar, J.M., Burakov, B.E., Zamoryanskaya, M.V., Garbuzov, V.M., Kitsay, A.A., and Zirlin, V.A. (2004) Investigation of Pu incorporation into zircon single crystal. Scientific Basis for Nuclear Waste Management XXVIII, 824, 225-229.

Harley, S.L., and Kelly, N.M. (2007) Zircon - Tiny but timely. Elements, 3, 13-18.

Hawkesworth, C.J., and Kemp, A.I.S. (2006) Using hafnium and oxygen isotopes in zircons to unravel the record of crustal evolution. Chemical Geology, 226, 144-162.

Hinton, R.W., and Upton, B.G.J. (1991) The chemistry of zircon - variations within and between large crystals from syenite and alkali basalt xenoliths. Geochimica Et Cosmochimica Acta, 55(11), 3287-3302.

Hoskin, P.W.O., and Rodgers, K.A. (1996) Raman spectral shift in the isomorphous series $(Zr_{1-x}Hf_x)SiO_4$. European Journal of Solid State and Inorganic Chemistry, 33, 1111-1121.

Hoskin, P.W.O., and Schaltegger, U. (2003) The composition of zircon and igneous and metamorphic petrogenesis. In J.M. Hanchar, and P.W.O. Hoskin, Eds. Zircon, 53, p. 27-55. Mineralogical Society of America, Washington, D.C.

Keller, C. (1963) Untersuchung der Germanate und Silikate des Typs ABO_4 der vierwertigen Elemente Thorium bis Americium. Nukleotik, 5, 41-48.

Kim, H.S., Joung, C.Y., Lee, B.H., Oh, J.Y., Koo, Y.H., and Heimgartner, P. (2008) Applicability of CeO_2 as a surrogate for PuO_2 in a MOX fuel development. Journal of Nuclear Materials, 378, 98-104.

Kleykamp, H. (1999) Selection of materials as diluents for burning of plutonium fuels in nuclear reactors. Journal of Nuclear Materials, 275, 1-11.

Konings, R.J.M., Popa, K., Wastin, F., and Colineau, E. (2008) The low-temperature heat capacity and standard entropy of synthetic huttonite $ThSiO_4$. Journal of Chemical Thermodynamics, 40, 931-934.

Levien, L., Prewitt, C.T., and Weidner, D.J. (1980) Structure and elastic properties of quartz at pressure. American Mineralogist, 65, 920-930.

Levin, E.M., and McMurdie, H.F. (1975) Phase Diagrams for Ceramists. 1975 Supplement American Ceramic Society, Columbus, OH, 513 p.

Lumpkin, G.R. (2006) Ceramic waste forms for actinides. Elements, 2, 365-372.

Lumpkin, G.R., and Chakoumakos, B.C. (1988) Chemistry and radiation effects of thorite-group minerals from the Harding pegmatite, Taos County, New-Mexico. American Mineralogist, 73(11-12), 1405-1419.

Mazeina, L., Ushakov, S.V., Navrotsky, A., and Boatner, L.A. (2005) Formation enthalpy of $ThSiO_4$ and enthalpy of the thorite -> huttonite phase transition. Geochimica et Cosmochimica Acta, 69, 4675-4683.

McCullough, J.D., and Trueblood, K.N. (1959) The crystal structure of baddeleyite (monoclinic ZrO2). Acta Crystallographica, 12(7), 507-511.

Meis, C., and Gale, J.D. (1998) Computational study of tetravalent uranium and plutonium lattice diffusion in zircon. Materials Science and Engineering B-Solid State Materials for Advanced Technology, 57(1), 52-61.

Meldrum, A., Zinkle, S.J., Boatner, L.A., and Ewing, R.C. (1998) A transient liquid-like phase in the displacement cascades of zircon, hafnon and thorite. Nature, 395, 56-58.

-. (1999) Heavy-ion irradiation effects in the ABO_4 orthosilicates: decomposition, amorphization, and recrystallization. Physical Review B, 59, 3981-3992.

Mumpton, F.A., and Roy, R. (1961) Hydrothermal stability studies of the zircon-thorite group. Geochimica et Cosmochimica Acta, 21(3-4), 217-238.

Myers, E.R. (1998) A statistical-mechanics model of ordering in aluminosilicate solid solutions. Physics and Chemistry of Minerals, 25, 465-468.

Naher, S., and Haseeb, A. (2008) Production and purification of zircon opacifier from zircon found in the coastal area of Bangladesh. Journal of Materials Processing Technology, 205(1-3), 203-206.

Pepin, J.G., Vance, E.R., and McCarthy, G.J. (1981) The crystal-chemistry of cerium in the monazite structure-type phase of tailored-ceramic nuclear waste forms. Materials Research Bulletin, 16(6), 627-633.

Pointeau, V., Deditius, A.P., Miserque, F., Renock, D., Becker, U., Zhang, J., Clavier, N., Dacheux, N., Poinssot, C., and Ewing, R.C. (2009) Synthesis and characterization of coffinite. Journal of Nuclear Materials, submitted.

Pollok, K., Jamtveit, B., and Putnis, A. (2001) Analytical transmission electron microscopy of oscillatory zoned grandite garnets. Contributions to Mineralogy and Petrology, 141, 358-366.

Ramakrishnan, S.S., Gokhale, K.V.G., and Subbarao, E.C. (1969) Solid solubility in system zircon - hafnon. Materials Research Bulletin, 4(5), 323-328.

Robertson, J. (2000) Band offsets of wide-band-gap oxides and implications for future electronic devices. Journal of Vacuum Science & Technology B, 18(3), 1785-1791.

Robinson, K., Gibbs, G.V., and Ribbe, P.H. (1971) The structure of zircon: a comparison with garnet. American Mineralogist, 56, 782-790.

Scherer, E.E., Whitehouse, M.J., and Munker, C. (2007) Zircon as a monitor of crustal growth. Elements, 3(1), 19-24.

Shannon, R.D. (1976) Revised effective ionic-radii and systematic studies of interatomic distances in halides and chalcogenides. Acta Crystallographica Section A, 32(SEP1), 751-767.

Shein, I.R., Shein, K.I., and Ivanovskii, A.L. (2006) Thorite versus huttonite: stability, electronic properties and X-ray emission spectra from first-principle calculations. Physics and Chemistry of Minerals, 33(8-9), 545-552.

Sirdeshmukh, D.B., and Subhadra, K.G. (1975) Elastic properties of zircon. Journal of Applied Physics, 46(8), 3681-3682.

Skakle, J.M.S., Dickson, C.L., and Glasser, F.P. (2000) The crystal structures of $CeSiO_4$ and $Ca_2Ce_8(SiO_4)_6O_2$. Powder Diffraction, 15(4), 234-238.

Speer, J.A. (1982a) The actinide orthosilicates. In P.H. Ribbe, Ed. Orthosilicates, 5. Mineralogical Society of America, Washington, D.C.

-. (1982b) Zircon. In P.H. Ribbe, Ed. Orthosilicates, 5. Mineralogical Society of America, Washington, D.C.

Speer, J.A., and Cooper, B.J. (1982) Crystal-structure of synthetic hafnon, $HfSiO_4$, comparison with zircon and the actinide orthosilicates. American Mineralogist, 67(7-8), 804-808.

Subbarao, E.C. (1990) Thermal-expansion of compounds of zircon structure. Journal of the American Ceramic Society, 73(5), 1246-1252.

Taylor, M., and Ewing, R.C. (1978) Crystal-structures of ThSiO4 polymorphs - huttonite and thorite. Acta Crystallographica Section B-Structural Science, 34(APR), 1074-1079.

Ushakov, S.V., Burakov, B.E., Garbuzov, V.M., Anderson, E.B., Strykanova, E.E., Yagovkina, M.M., Helean, K.B., Guo, Y.X., Ewing, R.C., and Lutze, W. (1998) Synthesis of Ce-doped zircon by a sol-gel process. Scientific Basis for Nuclear Waste Management XXI, 506, 281-288. [this does not sound like a technique that will attain equilibrium.]

Ushakov, S.V., Gong, W., Yagovkina, M.M., Helean, K.B., Lutze, W., and Ewing, R.C. (1999) Solid solutions of Ce, U, and Th in zircon. Environmental Issues and

Waste Management Technologies in the Ceramic and Nuclear Industries IV, 93, 357-363.

Vance, E.R. (1994) Synroc - a suitable waste form for actinides. Mrs Bulletin, 19(12), 28-32.

Vettraino, F., Magnani, G., La Torretta, T., Marmo, E., Coelli, S., Luzzi, L., Ossi, P., and Zappa, G. (1999) Preliminary fabrication and characterisation of inert matrix and thoria fuels for plutonium disposition in light water reactors. Journal of Nuclear Materials, 274(1-2), 23-33.

Vinograd, V.L., Sluiter, M.H.F., Winkler, B., Putnis, A., Halenius, U., Gale, J.D., and Becker, U. (2004) Thermodynamics of mixing and ordering in pyrope-grossular solid solution. Mineralogical Magazine, 68(1), 101-121.

Warren, M.C., Dove, M.T., Myers, E.R., Bosenick, A., Palin, E.J., Sainz-Diaz, C.I., Guiton, B.S., and Redfern, S.A.T. (2001) Monte Carlo methods for the study of cation ordering in minerals. Mineralogical Magazine, 65(2), 221-248.

Weber, W.J. (1991) Self-radiation damage and recovery in Pu-doped zircon, 115(4), 341-349.

Weber, W.J., Ewing, R.C., Catlow, C.R.A., de la Rubia, T.D., Hobbs, L.W., Kinoshita, C., Matzke, H., Motta, A.T., Nastasi, M., Salje, E.K.H., Vance, E.R., and Zinkle, S.J. (1998) Radiation effects in crystalline ceramics for the immobilization of high-level nuclear waste and plutonium. Journal of Materials Research, 13, 1434-1484.

Weber, W.J., Ewing, R.C., and Lutze, W. (1996) Performance assessment of zircon as a waste form for excess weapons plutonium under deep borehole burial conditions. Scientific Basis for Nuclear Waste Management XIX, 412, 25-32.

Wilk, G.D., and Wallace, R.M. (1999) Electrical properties of hafnium silicate gate dielectrics deposited directly on silicon. Applied Physics Letters, 74, 2854-2856.

Wilk, G.D., Wallace, R.M., and Anthony, J.M. (2000) Hafnium and zirconium silicates for advanced gate dielectrics. Journal of Applied Physics, 87, 484-492.

Williamson, M.A., Huang, J.C., and Putnam, R.L. (2000) Fundamental Thermodynamics of Actinide-Bearing Mineral Waste Forms, p. 20. Lawrence Livermore National Laboratory, U.S. Department of Energy.

Williford, R.E., Begg, B.D., Weber, W.J., and Hess, N.J. (2000) Computer simulation of Pu^{3+} and Pu^{4+} substitutions in zircon. Journal of Nuclear Materials, 278(2-3), 207-211.

Wyckoff, R.W.G. (1963) Crystal Structures 1. Interscience Publishers, New York, New York.

Xu, H., and Wang, Y. (2000) Prediction of thermodynamic property of Pu-zircon and Pu-pyrochlore. Plutonium Futures - - the Science: Topical Conference on Plutonium and Actinides., 532, p. 363.

Xu, H.F., and Wang, Y.F. (1999) Electron energy-loss spectroscopy (EELS) study of oxidation states of Ce and U in pyrochlore and uraninite - natural analogues for Pu- and U-bearing waste forms. Journal of Nuclear Materials, 265(1-2), 117-123.

Yeomans, J.M. (1992) Statistical mechanics of phase transitions. 164 p. Oxford Science Publications, Clarendon Press, Oxford.

CHAPTER 4.

COMPUTATIONAL STUDY OF THE EFFECT OF PRESSURE ON THE TI-IN-ZIRCON GEOTHERMOMETER

4.1. Abstract

Understanding how Ti partitions between the Si and Zr sites in zircon is crucial for developing the Ti-in-zircon geothermometer. Energies calculated using quantum mechanical methods (*VASP, CASTEP*, *Dmol*^{3}, *Crystal*) were used to compare the relative favorability of substitution into each site at pressures ranging from 0 to 10 GPa. The results of these quantum-mechanical calculations were used in Monte-Carlo calculations to derive the excess enthalpy of mixing (ΔH_{excess}), entropy of mixing (ΔS_{excess}), and free energy of mixing (ΔG_{excess}) for the binaries $ZrSiO_4$-$ZrTiO_4$ and $ZrSiO_4$-$TiSiO_4$ (assuming that all compositions have zircon structure) at temperatures ranging from 333 K to 3000 K, and estimates are made of the maximum amount of Ti that may be incorporated into each site as a function of temperature and pressure. The results are considered in thermodynamic reference to other oxides, such as SiO_2, ZrO_2, and TiO_2, that are involved in substitution reactions. At pressures below about 3.5 GPa, substitution into the Si site is more thermodynamically favorable and thus dominates, whereas at higher pressures, substitution into the Zr site becomes more important in zircon. The latter result suggests that the reaction

$TiO_{2(rutile)}$ + $ZrSiO_{4(zircon)}$ ↔ $TiSiO_{4(zircon)}$ + $ZrO_{2\ (baddeleyite)}$ becomes predominant for the substitution of Ti in zircon for ultra-high pressure assemblages. The molar volume of the theoretical zircon-structured compound $ZrTiO_4$ was calculated using quantum mechanics (*VASP*, *CASTEP*, *Dmol*^{3}) and determined to be 44.21 ± 0.45 cm^3/mol. The resulting ΔV for the reaction $ZrSiO_{4(zircon)}$ + $TiO_{2\ (rutile)}$ = $ZrTiO_{4\ (zircon)}$ + $SiO_{2\ (quartz)}$ is doubled. The Clapeyron slope (dP/dT) of the reaction is halved, and the pressure correction to the Ti-in-zircon thermometer is twice as large as a previous estimate.

4.2. Introduction

The Ti content of a zircon grain has been suggested to give a direct indication of the temperature of crystallization (or metamorphic growth), providing insight into the major geologic conditions and processes operating during Earth's distant past (Watson and Harrison, 2005; Watson et al., 2006; Ferry and Watson, 2007). However, a recent application of the thermometer reports temperatures lower than expected for natural zircons, and the factors controlling Ti concentration in zircon are not well understood (Fu *et al.*, 2007). Understanding the substitution mechanism of Ti in zircon is a crucial first step. Substitution into vacancies, for instance in the voids between the SiO_4 and ZrO_8 polyhedra or the open channels parallel to [001] (Figure 4.1), is assumed to be negligible because impurities usually substitute in the IV or VIII sites of zircon (Finch and Hanchar, 2003), leading to the following two general possibilities:

$$X\ TiO_2 + ZrSiO_{4(zircon)} \leftrightarrow Zr(Ti_xSi_{1-x})O_{4(zircon)} + X\ SiO_2, \quad (4.1)$$

$$X\ TiO_2 + ZrSiO_{4(zircon)} \leftrightarrow (Zr_{1-x}Ti_x)SiO_{4(zircon)} + X\ ZrO_2. \quad (4.2)$$

Equations (4.1) and (4.2) may also be written in terms of end-member components (X=1):

$$TiO_2 + ZrSiO_{4(zircon)} \leftrightarrow ZrTiO_{4(zircon)} + SiO_2, \quad (4.3)$$

$$TiO_2 + ZrSiO_{4(zircon)} \leftrightarrow TiSiO_{4(zircon)} + ZrO_2. \quad (4.4)$$

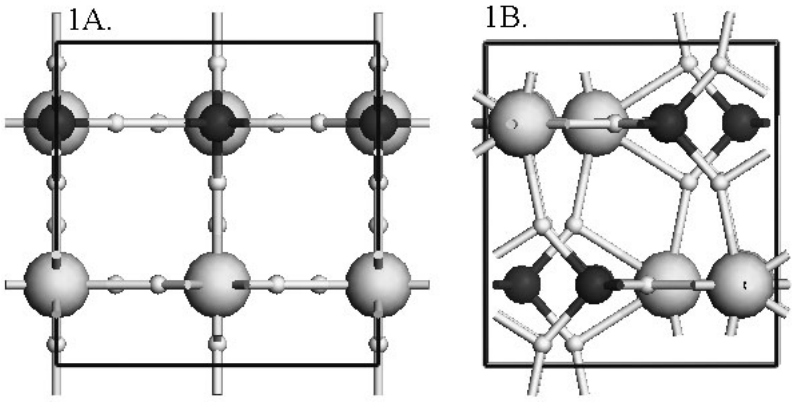

Figure 4.1. Ball-and-stick models of the zircon conventional cell (space group *$I4_1/amd$*) used in quantum mechanical calculations of the solid solutions $ZrSi_xTi_{(1-x)}O_4$ and $Zr_xTi_{(1-x)}SiO_4$ at x=0, 0.25, 0.5, 0.75, and 1. Very small balls are O, large balls are Zr, and dark balls are Si. Figure 1A is projected on [001], showing channels that may contain interstitial atoms, and Figure 1B is projected on [100].

The structure of the oxides (*e.g.* $SiO_{2\ (quartz)}$ vs. $SiO_{2\ (coesite)}$) will depend on the pressure and temperature conditions under consideration. Baddeleyite, ZrO_2, is rare in most crustal rocks as it reacts with SiO_2 to form zircon and may also react with TiO_2 to form srilankite or $TiZrO_4$ (Troitzsche and Ellis, 2005). The equation describing subsitution into the Zr site may also be considered as

$$TiO_2 + SiO_2 \leftrightarrow TiSiO_{4(zircon)}. \quad (4.5)$$

Because Ti concentrations in natural zircon are typically below 20 ppm (Fu *et al.*, 2008) and reach a maximum of about 100 ppm (Harley and Kelly, 2007), electron microprobe analysis is difficult to apply. In some instances, electron energy loss spectroscopy might be used, but again, due to the very low concentration of Ti, this

technique has not yet been successfully used in identifying the Ti site in zircon. Ti is typically in octahedral coordination (Stoyanov *et al.*, 2007). Based on tabulations of ionic radii (*e.g.*, Shannon, 1976) there is no clear preference of Ti for the IV-coordinated Si site as compared with the VIII-coordinated Zr site. The ionic radius of VIII-coordinated Zr^{4+} (0.098 nm) is somewhat closer to that of VIII-coordinated Ti^{4+} (0.088 nm) as compared with the IV-coordinated Si^{4+} (0.040 nm) to that of IV-coordinated Ti^{4+} (0.056 nm) (Shannon, 1976). Recent experiments involving zircon crystallization in the presence of SiO_2 and TiO_2 indirectly suggest that substitution of Ti into the Si site dominates (Harrison et al., 2005; Ferry and Watson, 2007).

In this study the free energy changes (ΔG) of the two equations (4.3) and (4.4) were calculated using quantum-mechanical techniques at 0 K and pressures ranging from 0 to 10 GPa. Particular emphasis was placed on determining an accurate molar volume of the end-member $ZrTiO_{4(zircon)}$ for use in pressure corrections to the Ti-in-zircon thermometer. To gain a more complete understanding of the system, the two binaries, $ZrSiO_4$ – $ZrTiO_4$ and $ZrSiO_4$ – $TiSiO_4$ are compared, with each binary treated as a zircon-structured solid solution without a phase transition whose end-members are the components of equations (4.3) and (4.4). This is justified by the fact that incorporated Ti concentrations are small with no phase change involved. Quantum-mechanical simulations were used to estimate the structures and internal energies of the binaries, and this work, coupled with Monte-Carlo calculations, was employed to gain a better understanding of the two solid-solution systems. The combination of these computational approaches allows evaluation of the excess properties enthalpy, Gibbs free energy, and entropy of mixing (ΔH_{excess}, ΔG_{excess}, and

ΔS_{excess}), as well as volume and lattice parameter changes as a function of pressure and composition.

4.3. Computational Methods

4.3a. Quantum-mechanical total-energy calculations

In experiment-based thermodynamics, the change in free energy for a given chemical equation, a measure of the thermodynamic favorability of the products versus the reactants, at constant temperature is taken as

$$\Delta G(T,P) = \Delta H(T,1\,bar) - T\Delta S(T,1\,bar) + \int_{1\,bar}^{P} \Delta V dP\,. \tag{4.6}$$

This equation allows the calculation of ΔG for a reaction at pressure without the need to measure ΔH and ΔS at the pressure of interest. In quantum mechanical calculations, applying an external pressure is relatively straightforward and involves the addition of the pressure of interest to the stress tensor applied to the system. At a temperature of 0 K, $\Delta G(T,P)$ then becomes

$$\Delta G(T,P) = \Delta H(T,P)_{calculated}. \tag{4.7}$$

There is a wide variety of methods for solving the Schrödinger equation. The bulk of the calculations described in this paper uses density functional theory (DFT) (Hohenberg and Kohn, 1964; Kohn and Sham, 1965) with either the simple local density approximation (LDA) or the density functional of Perdew & Wang (1991) within the general gradient approximation (GGA). Ultra-soft pseudopotentials (Payne *et al.*, 1992) are used in all cases, although these differ somewhat between software

packages such as CASTEP (CAmbridge Serial Total Energy Package) and VASP (Vienna Ab-initio Simulation Package). GGA rather than LDA was used to calculate the enthalpy of all phases in equations (4.3) and (4.4) at pressures between 0 and 10 GPa because the phase transitions in SiO_2 at higher pressures (from quartz to coesite and then to stishovite) are modeled more accurately using GGA than LDA (Hamann, 1996). These calculations were carried out using the software package CASTEP, using 0.07 $Å^{-1}$ k-point spacing and 700 eV planewave cut-off energy. The error in the calculated pressure (known as the Pulay stress) is approximately 0.1 GPa.

4.3b. Evaluation of solid-solution mixing properties

Calculating the thermodynamic properties of a solid solution was performed in three steps (Bosenick *et al.*, 2001): (1) the quantum mechanical treatment of the end-members and a small number (5-10) of different configurations and compositions, (2) the derivation of cation-cation exchange parameters for rapid computation in (3) Monte-Carlo simulations to obtain $\Delta H_{excess}(T,X)$, and subsequent Bogoliubov integration for the calculation of $\Delta G_{excess}(T,X)$ and $\Delta S_{excess}(T,X)$ (Yeomans, 1992).

4.3c. Quantum mechanical treatment of representative compositions

The two solid solutions or interest are $ZrSiO_4$-$ZrTiO_4$ (representing Ti substitution into the Si site) and $ZrSiO_4$ – $TiSiO_4$ (representing Ti substitution into the Zr site). The intermediate compositions may be represented by $ZrSi_xTi_{(1-x)}O_4$ and $Zr_xTi_{(1-x)}O_4$, with X varying between 0 and 1. DFT with LDA as implemented by VASP was used to calculate the structures and enthalpies of 5 to 10 representative members of these two zircon-structured solid solutions at external pressures of 0, 1, 2,

and 10 GPa. VASP with LDA was chosen for the derivation of cation-cation exchange parameters based on agreement with experimental observations of zircon lattice parameters (Table 4.1). These calculations determine the excess energy (ΔE_{excess}) for a given configuration of cations, which is the difference between the total energy of a solid solution and the combined total energies of a compositionally equivalent mixture of end-members.

Table 4.1. Zircon lattice parameters calculated using different quantum mechanical approaches

Method	a=b (Å)	Deviation a,b (%)	c (Å)	Deviation c (%)	% volume error
synthetic zircon (Robinson *et al.*, 1971)	6.607	-	5.982	-	-
VASP (LDA)	6.609	0.030	5.955	-0.457	-0.40
CASTEP (GGA)	6.614	0.107	5.936	-0.763	-0.55
CASTEP (GGA, PBE pseudopotential)	6.656	0.740	6.003	0.342	-0.58
Crystal (GGA, LANL basis set)	6.575	-0.490	6.157	2.923	1.92
VASP (GGA)	6.669	0.932	6.037	0.914	2.80
CASTEP (LDA)	6.540	-1.012	5.901	-1.355	-3.34
Dmol^3 (GGA)	6.720	1.710	6.050	1.137	4.63
Crystal (GGA, sbk basis set)	6.036	-8.647	5.999	0.289	-16.31

4.3d. Calculation of cation-cation interaction parameters for solid solutions

Because quantum-mechanical calculations are computationally expensive, they cannot be used to evaluate the energies of more than a few configurations. In order to evaluate more configurations, cation-cation interaction parameters (*J*'s) are fitted to quantum-mechanically obtained energies of mixing for specific members of the solid solutions (ΔE_{excess} computed above). These *J*'s can then be used to quickly determine the energy of any configuration within that solid solution in a much larger supercell. This allows the evaluation of millions of configurations for unit cells of thousands of atoms to determine ΔH_{excess} and ultimately ΔG_{excess} and ΔS_{excess} at a given temperature. The energy of mixing (E_{mixing}) for any member of a solid solution is approximated by the sum over all exchangeable cation interactions of the number *n* of *i*-type interactions for each cation pair multiplied by an interaction parameter *J* that describes the energy of the cation-cation interaction. Here, the *n*'s are specific for each cation configuration generated, while the *i*'s in *i*-type interaction denote that,

e.g., first nearest-neighbor interaction (*i*=1), second nearest-neighbor interaction etc. are included. Thus, the mixing energy for any solid solution may be represented as:

$$E_{mixing} = \sum_i \left(n^i J^i\right) \xrightarrow{\text{fitted to}} E_{excess}\,(q.m.). \tag{4.8}$$

The different interaction types *i* are defined for each solid solution by the geometric relationships between the exchangeable cations (Table 4.2). *J* in this case is defined by the following equation:

$$J = E_{YZ} - \frac{1}{2}\left(E_{YY} + E_{ZZ}\right), \tag{4.9}$$

where E is the bond energy between two of the exchangeable cations Y and Z. These *J* values may be fitted for a given solid solution series using the excess energies calculated previously. For any given interaction type *i*, a positive J value indicates that homocationic interactions (*e.g.*, Si-Si, Zr-Zr, or Ti-Ti) are more favorable, while a negative J means that heterocationic interactions (*e.g.*, Zi-Ti or Si-Ti) are preferable. In this study, interaction parameters are fitted for the interaction types representing the two nearest cation neighbors. A Margules function is included to describe the asymmetry and the configuration-independent but concentration-dependent energy (often referred to as E_o) of the disordered system:

$$\text{Margules energy term} = E_o = X\cdot(1\text{-}X)\cdot(A\cdot X + B\cdot(1\text{-}X)), \tag{4.10}$$

$$\text{Energy of the total system} = \sum_i \left(n^i J^i\right) + E_0\,. \tag{4.11}$$

Because the interaction parameters are highly dependent on the Margules term (E_o), A and B were fitted along with the *J*'s for each binary to give the greatest correlation

between *ab-initio* and calculated energies using the *J* formalism. These fits are generated separately for each solid solution (Table 4.3). As an example, the fitted excess energies of the $ZrSiO_4$-$TiSiO_4$ solid solution at 0 GPa are compared to the excess energies calculated using VASP (Figure 4.2).

Table 4.2. Cation-cation interaction types *i* as defined by the cation-cation distances and absolute values of Δx (|| to (100)), Δy (|| to (010)), and Δz (|| to (001)) in the zircon and srilankite-type structures.

Label i	Distance (Å)	Δx (Å)	Δy (Å)	Δz (Å)
1	3.63	0.00	3.30	1.50
2	5.55	3.30	3.30	2.99
3	5.57	0.00	3.30	4.49
4	5.98	0.00	6.61	5.98

Table 4.3. Fitted interaction parameters (*J*) in kJ/mol and Margules parameters (Marg A and B) defined for the first two nearest cation neighbors in both zircon-structured solid solutions at three different pressures (P). The goodness of fit between the fitted and original calculated energies is represented by the correlation coefficient r^2.

	Si-Ti (zircon)	Si-Ti (zircon)	Si-Ti (zircon)	Zr-Ti (zircon)	Zr-Ti (zircon)	Zr-Ti (zircon)
P (GPa)	0	2	10	0	2	10
compositions	10	5	5	9	5	5
Marg A	25.4	25.4	25.4	31.6	31.6	31.6
Marg B	33.4	33.4	33.4	21.8	21.8	21.8
J i=1	-0.0237	-0.0196	-0.0142	0.130	0.133	0.143
J i=2	-0.0290	-0.0290	-0.0301	0.0391	0.0399	0.0429
correlation coefficient	0.98288	0.99903	0.99985	0.99981	0.99997	0.99999

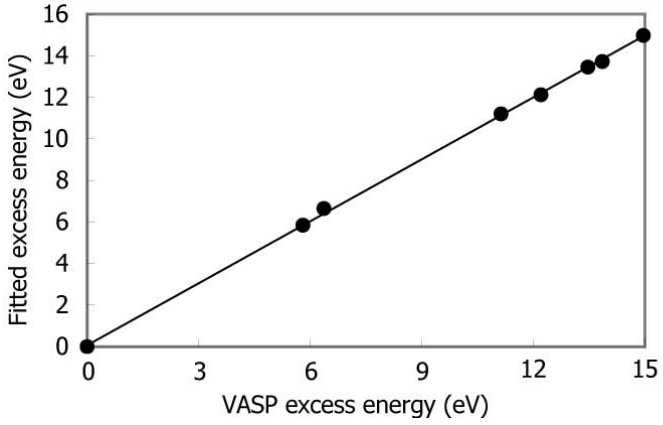

Figure 4.2. Excess energies of $ZrSiO_4$-$TiSiO_4$ binary calculated using fitted interaction parameters as a function of excess energies calculated using the quantum mechanical code VASP. The points form a straight line (1:1 line shown) with a correlation coefficient of 0.99981. Correlation coefficients for all fitted solid solution series are listed in Table 4.3.

4.3e. Monte-Carlo simulation: determination of thermodynamic properties

Once the interaction parameters have been fitted successfully, they may be used to rapidly evaluate millions of configurations within each binary using the Monte Carlo method ((Myers, 1998) for a more complete description of the method). For each binary, 8×8×8 supercells, each containing 2,048 exchangeable cations, were constructed. A Monte-Carlo simulation code (Becker *et al.*, 2000) randomly swaps the positions of the two exchangeable cations and determines the favorability of a new configuration relative to the previous one. The switch has a probability of occurrence of one if the resulting change in lattice energy (ΔE) is negative. If ΔE is positive, the switch is assigned a probability P based on the Boltzmann distribution:

$$P = \exp\left(\frac{-\Delta E_{swap}}{k_B T}\right), \tag{4.12}$$

where k_B is 1.3807×10^{-23} J K^{-1} and T is temperature in K. The excess enthalpy of mixing (ΔH_{excess}) for each composition is calculated by averaging over the last 100,000 successful swaps (after an equilibration time of another 100,000 successful swaps) at a given temperature. Calculations were made for the following temperatures: 3000, 1500, 1000, 750, 600, 500, 429, 375 and 333 K. The excess entropy and free energy of mixing (ΔS_{excess} and ΔG_{excess}) are then be calculated using a Bogoliubov integration scheme (Yeomans, 1992; Myers, 1998).

4.4. Results

4.4a. Free energy comparison

Table 4.4 and Table 4.5 show the calculated enthalpies of phases relevant to equations (4.3) and (4.4) as a function of pressure. Because the calculations assume a temperature of 0 K, TiO_2(II), rather than rutile, is the lowest-energy polymorph of TiO_2. This observation is in general agreement with experiments (Withers *et al.*, 2003). Experiments suggest that the quartz to coesite transition should take place at around 2 GPa at 0 K (Hemingway *et al.*, 1998), and the general trend in stabilities of SiO_2 phases are in agreement with experiments.

Table 4.6 compares the calculated ΔG of the two equations and shows that at pressures below 3.5 GPa, equation (4.3) is less unfavorable than equation (4.4), suggesting substitution into the Si site. However, at higher pressures, the calculated ΔG values of equation (4.3) are higher than those of equation (4.4), suggesting substitution into the Zr site. This trend is constant even when the coesite to quartz transition is assumed to take place at 1 or 2 GPa. Rutile, the dominant high temperature phase, is used for all calculations presented, although using TiO_2(II), the

stable phase at 0 K, yields the same trends. When equation (4.5) is considered instead of equation (4.4), the change from substitution into the Si site to the Zr site is predicted to occur between 1 and 2 GPa.

Table 4.4. Enthalpies in kJ/mol calculated using CASTEP and DFT with GGA of phases relevant to comparing Ti substitution into the Si versus the Zr site of zircon.

GPa	zircon	$ZrTiO_4$	$TiSiO_4$	ZrO_2 baddeleyite
0	-303851.00	-448232.54	-334720.64	-208657.37
1	-303811.06	-448187.50	-334685.12	-208635.74
2	-303771.31	-448142.69	-334649.75	-208614.39
3	-303731.68	-448098.19	-334614.54	-208592.80
3.25	-303721.81	-448087.08	-334605.77	-208587.61
3.5	-303711.96	-448075.99	-334597.00	-208582.20
4	-303692.31	-448053.84	-334579.48	-208571.47
6	-303614.07	-447965.78	-334509.80	-208529.36
10	-303459.56	-447792.05	-334372.10	-208445.57

Table 4.5. Enthalpies in kJ/mol calculated using CASTEP and DFT with GGA of SiO_2 and TiO_2.

GPa	SiO_2 quartz	SiO_2 coesite	SiO_2 stishovite	TiO_2 rutile	TiO_2(II)	favored SiO_2 phase
0	-95184.37	-95175.20	-95123.32	-239612.45	-239614.06	quartz
1	-95160.35	-95153.98	-95109.00	-239593.30	-239595.24	quartz
2	-95136.92	-95133.13	-95094.73	-239574.24	-239576.50	quartz
3	-95114.18	-95112.42	-95080.52	-239555.27	-239557.84	quartz
3.25	-95108.60	-95107.27	-95076.97	-239550.54	-239553.21	quartz
3.5	-95103.04	-95102.14	-95073.43	-239545.81	-239548.56	quartz
4	-95091.99	-95091.88	-95066.35	-239536.38	-239539.28	quartz
6	-95048.94	-95051.47	-95038.17	-239498.85	-239502.40	Coesite
10	-94967.04	-94972.47	-94982.37	-239424.73	-239429.58	Stishovite

Table 4.6. Calculated change in enthalpy (ΔH) of equations (4.3), (4.4), and (4.5) as a function of pressure at 0 K calculated with DFT (GGA) using CASTEP. The ZrO_2 polymorph is baddeleyite, and the TiO_2 polymorph is rutile in all cases shown. Predicted Ti site preferences are based on a comparison of equations (4.3) and (4.4).

Pressure (GPa)	SiO_2 polymorph	$\Delta G_{(4.3)}$ (kJ/mol)	$\Delta G_{(4.4)}$ (kJ/mol)	$\Delta G_{(4.5)}$ (kJ/mol)	Ti substitution site
0	quartz	46.53	85.44	76.18	Si
1	quartz	56.51	83.50	68.53	Si
2	quartz	65.94	81.41	61.41	Si
3	quartz	74.57	79.60	54.91	Si
3.25	quartz	76.67	78.98	53.37	Si
3.5	quartz	78.74	78.57	51.85	Zr
4	quartz	82.86	77.74	48.89	Zr
6	coesite	95.68	73.76	40.52	Zr
10	stishovite	109.89	66.62	35.00	Zr

4.4b. Solid solutions

Quantum mechanics and Monte-Carlo simulations were used to determine the changes in geometry and thermodynamic mixing properties of the two solid solutions $ZrSiO_4$-$ZrTiO_4$ and $ZrSiO_4$-$TiSiO_4$. When Ti is substituted for Zr, calculated volume and lattice parameters decrease, whereas the molar volume and individual lattice parameters increase when Ti is substituted for Si (Figure 4.3).

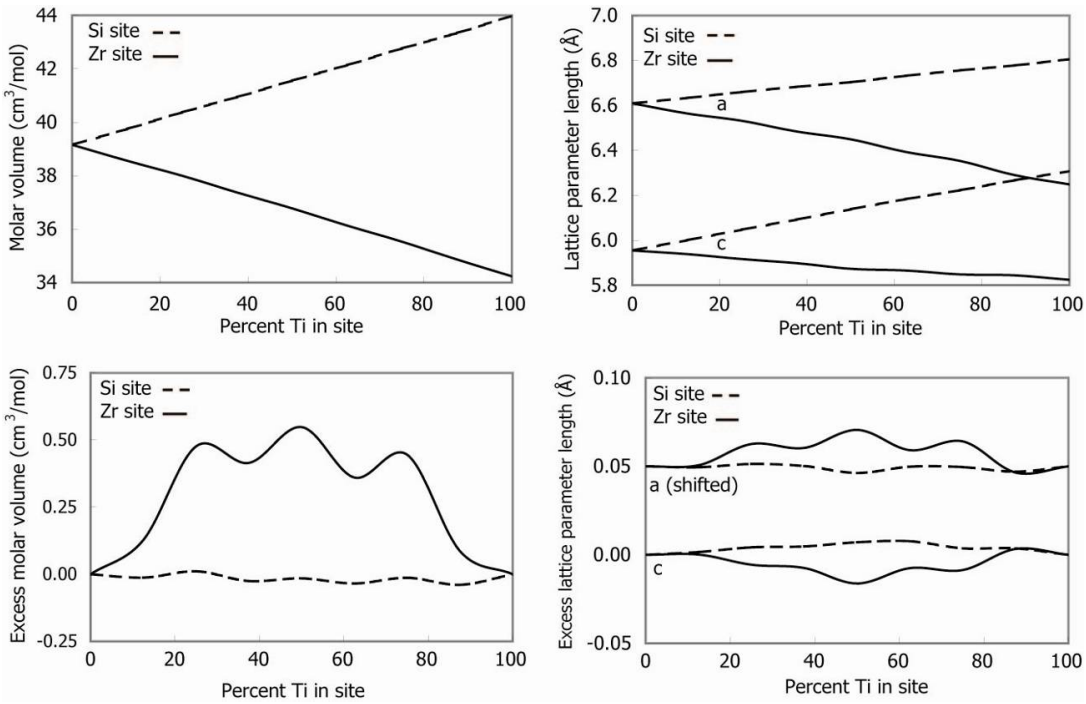

Figure 4.3. Changes in volume and lattice parameters of zircon calculated using VASP as a function of Ti concentration in the Zr and Si sites at 0 GPa.

4.4c. Enthalpy of mixing in zircon

Figure 4.4 shows the excess enthalpy of mixing (ΔH_{excess}) for both solid solutions. At all calculated values, including the minimum at X ≈ 0.065, and all temperatures, substitution into the Si site has much lower excess enthalpy than substitution into the Zr site. The differences between sites do not change appreciably with increasing pressure. Raising the pressure from 0 to 10 GPa may result in typical change of only about 0.2 kJ/mol while the difference between the sites remains much larger, roughly a factor of three.

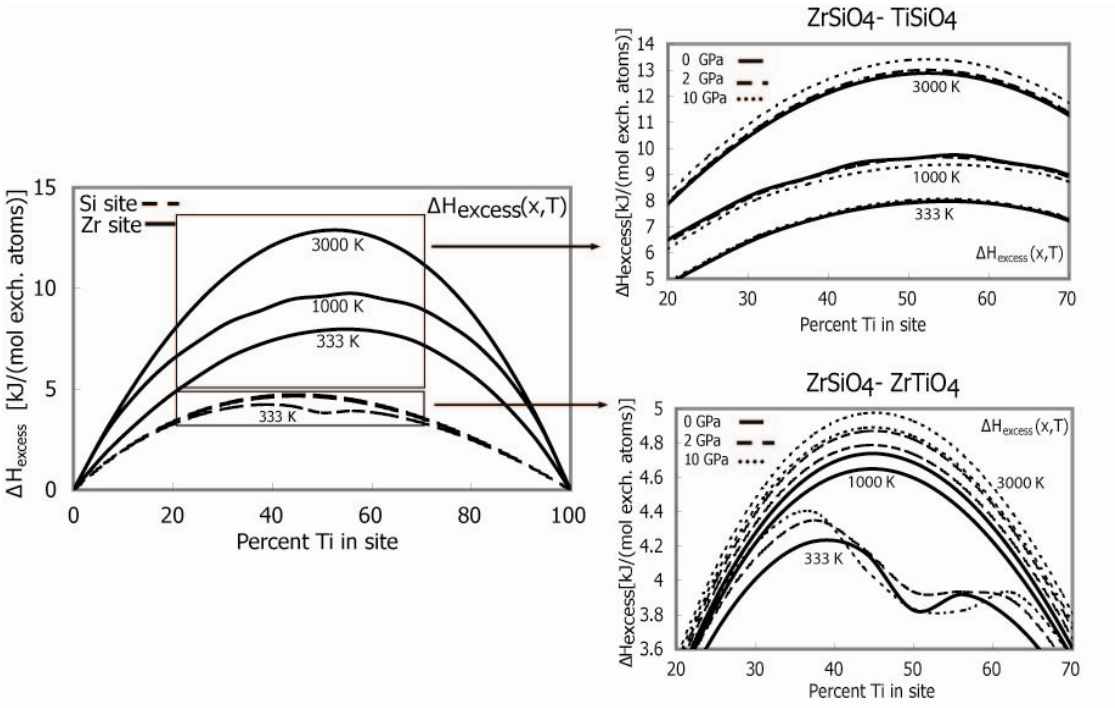

Figure 4.4. Excess enthalpy of mixing (ΔHexcess) for zircon-structured solid solutions at three different temperatures. The boxed areas on the main graph are shown at a larger scale with calculated ΔHexcess as a function of pressure as well as temperature.

4.4d. Gibbs free energy of mixing in zircon

A Bogoliubov integration scheme was applied to the data obtained using the Monte Carlo method in order to determine the excess free energy of mixing (ΔG_{excess}) (Figure 4.5). For both binaries, all intermediate compositions that were calculated directly were less favorable than a mechanical mixture of the end-members. However, at very low concentrations of the impurity, the entropy term will dominate. One approach for obtaining the ΔG_{excess} values for low concentrations is the cluster expansion method (Sanchez et al., 1984; Burton et al., 2006). Here the ΔG_{excess} values are estimated near X=0, where X is the mole fraction of Ti in the site, by approximating values of dH and dS:

$$\Delta G_{excess} = \Delta H_{excess} - T(A * \Delta S_{pt}). \tag{4.13}$$

This approach assumes that at very low x, the change in enthalpy is approximately linear and

$$\Delta H_x = \frac{\Delta H_1}{X_1} X, \tag{4.14}$$

where x_1 is the lowest value of X calculated using the Monte-Carlo method (0.0625 here), ΔH_1 is the calculated excess enthalpy at X_1 for the temperature and pressure of interest. The entropy change is assumed to be some constant A multiplied by the point entropy (because there is no specific ordering of Ti sites at very low concentrations)

$$\Delta S_{pt}(X \approx 0) = -AR[X \ln X + (1-X)\ln(1-X)], \tag{4.15}$$

where R is the gas constant 8.3145 J/(mol K). A, a constant that takes into account some system-specific lowering of the entropy, is determined for each pressure and temperature at X_1 (the lowest concentration used in the Monte-Carlo simulations) and assumed to be constant at low X values. The results of these approximations are shown in Figure 4.6.

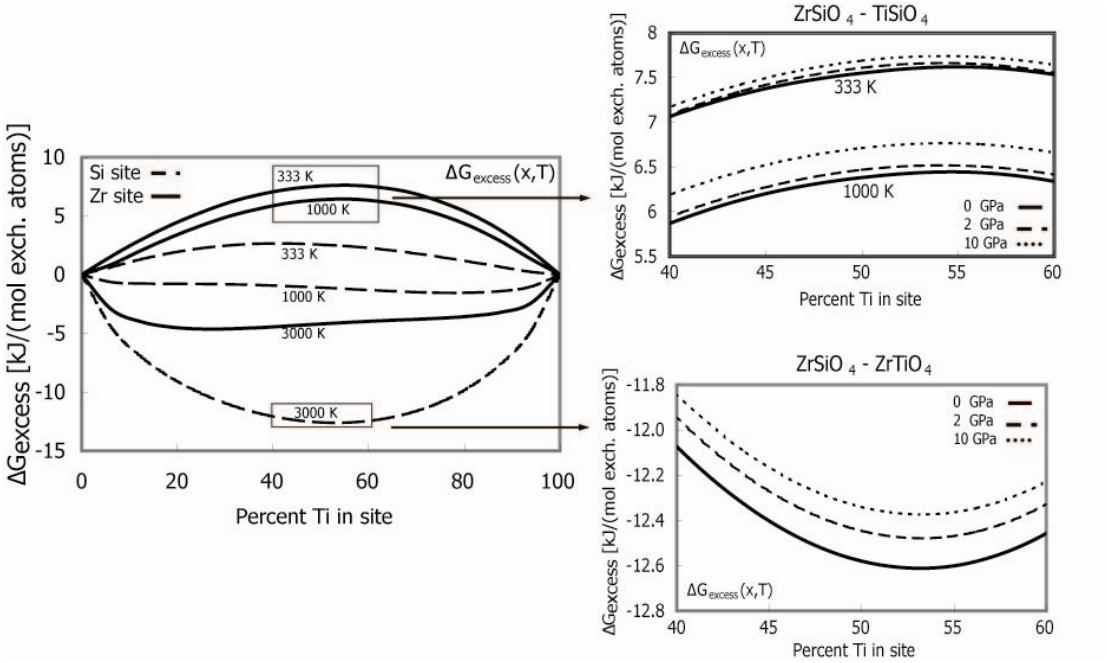

Figure 4.5. Excess free energy of mixing (ΔG_{excess}) for both zircon-structured solid solutions at three different temperatures. The boxed areas on the main graph are shown at a larger scale with calculated ΔG_{excess} as a function of pressure as well as temperature.

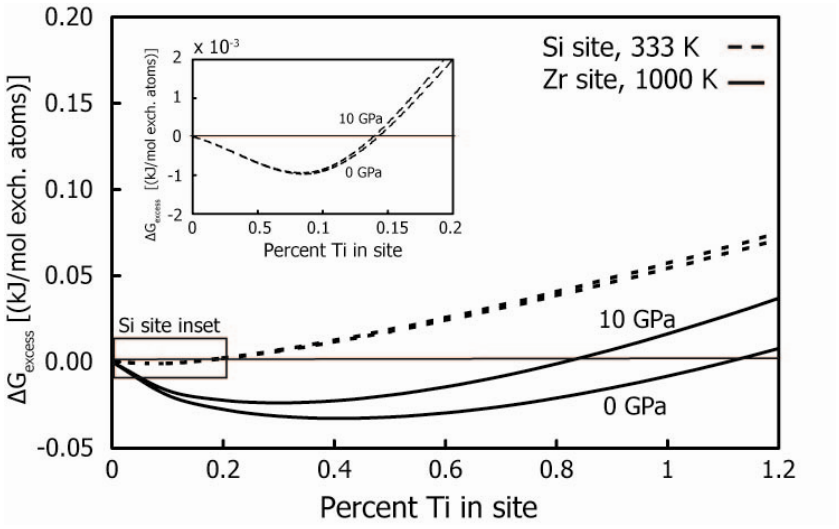

Figure 4.6. Estimated excess free energy of mixing (ΔG_{excess}) for both zircon-structured solid solutions with small amount of Ti showing the area where free energy becomes negative. Estimates are based on point entropies and values of excess free energy and enthalpy of mixing with 6.25% Ti. The boxed area on the main graph is shown at a larger scale with calculated ΔG_{excess} for Ti incorporation in the Si site at 333 K. Substitution into the Zr site at 333 K was not shown here because the percentages of Ti at which the substitution occurs are extremely low.

4.4e. Configurational entropy and ordering in zircon

Applying the relationship $\Delta G = \Delta H - T\Delta S$ yields the excess entropy of mixing (ΔS_{excess}) for each system (Figure 4.7). There is evidence for ordering at X=0.5 in the solid solution $ZrSiO_4 - ZrTiO_4$ at an equilibration temperature of 333 K (Figure 4.8), but this structure is still unfavorable relative to the end-members. The ordered solid solution was the more favorable of the two configurations of $ZrSi_{0.5}Ti_{0.5}O_{4(zircon)}$ included in the initial *ab-initio* calculations.

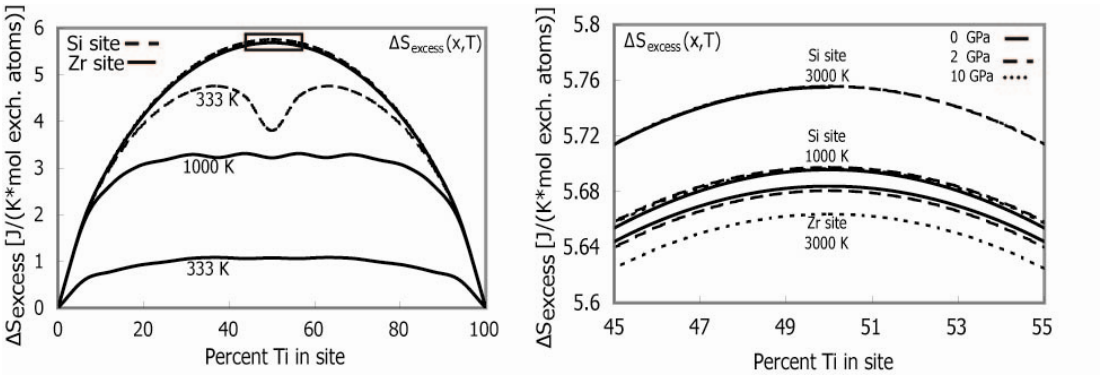

Figure 4.7. Excess entropy of mixing ΔSexcess (x,T,P) for both zircon-structured solid solutions at three different temperatures. The boxed area of 7A is shown at a larger scale in 7B with calculated ΔSexcess as a function of pressure as well as temperature.

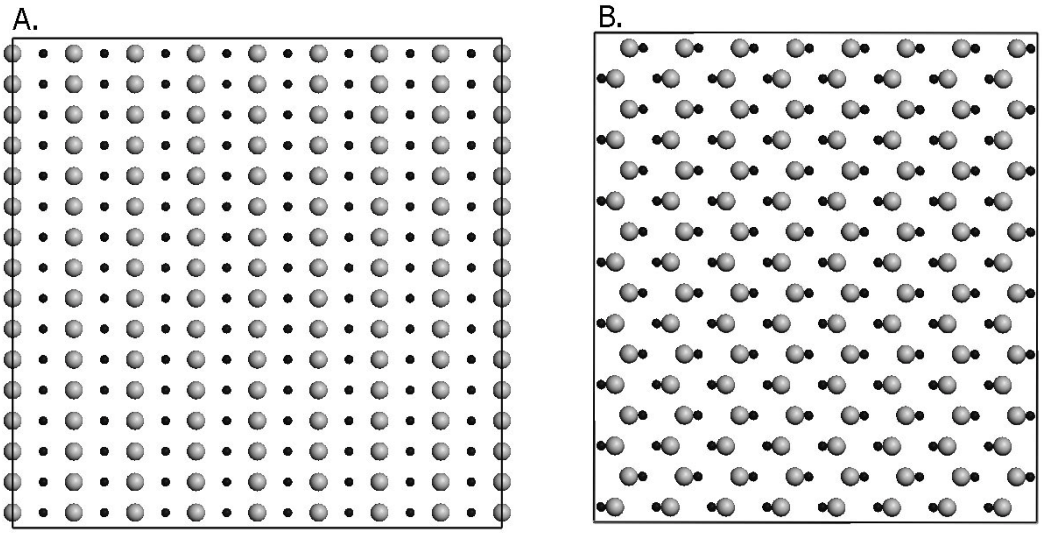

Figure 4.8. Preferred ordering scheme for the composition x=0.5 in the solid solution $ZrSi_xTi_{(1-x)}O_4$. Small dark balls represent Si, and larger balls represent Ti. Zr and O are not shown. Figure 8A is projected on [001] and 8B is projected on [100].

4.5. Discussion

4.5a. Favorability of Ti substitution into Si or Zr site

The excess free energies curves presented in Figure 4.8 do not vary significantly with pressure. However, a more accurate depiction of the excess free energy for these systems includes a measure of the stability of the solid solution end-members relative to a mixture of their constituting oxides, specifically SiO_2 as quartz, coesite, or stishovite, TiO_2(II) or rutile, and $ZrO_{2\ (baddeleyite)}$. This is done by offsetting the end-members from the zero line by an amount equal to difference in energy between the end-members and their constituent oxides, (Figure 4.9). The calculated energy differences between the solid-solution end-members and the oxides are both much larger than the excess energies of the solid solutions considered alone and change dramatically with pressure. Both this comparison and the energy differences calculated directly for equations (4.3) and (4.4) (shown in Table 4.6) demonstrate a

clear preference for substitution of Ti into the Si site at relatively low pressures (0-3.5 GPa) relevant for most crustal applications, but a preference for substitution into the Zr site at pressures above about 3.5 GPa. The pressure-temperature relationship of this transition is difficult to quantify without estimates of the entropy of the phases $ZrTiO_4$ and $SiTiO_4$.

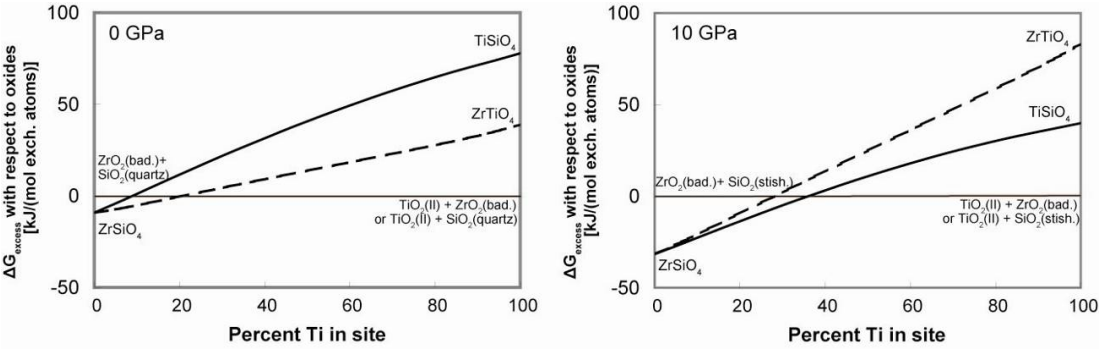

Figure 4.9. Excess free energy of both zircon-structured solid solutions modified by energy differences between end members and the oxides TiO_2(II), SiO_2 as either quartz or stishovite (stish), and ZrO_2 as baddeleyite (bad) calculated at 0 K (Table 4.4 and Table 4.5). At pressures below about 3.5 GPa, substitution of Ti into the Si site is expected to dominate, while at higher pressures, substitution into the Zr site is expected to dominate. The same general trend in end-points for this graph appear when using rutile as the TiO_2 phase, but the change from Si site to Zr site occurs between 3.5 and 4 GPa.

4.5b. Maximum amount Ti in Si and Zr sites of zircon

Because interactions are examined only between the first and second-nearest cation neighbors at relatively high concentrations of Ti, the accuracy of these calculations may have limitations for determining the exact amount of Ti that will enter the system under particular P-T conditions without applying cluster expansion methods (Burton et al., 2006; Sanchez et al., 1984). In previous work, incorporation estimates have been made based on a relationship between end-member volume differences and the activity coefficients and mole fractions of the impurity (Spera *et al.*, 2006). In this study, the Gibbs free energy curve is estimated near x=0, where X

is the mole fraction of Ti in the site. The maximum amount of Ti that will enter either site is approximately the value of X (defined as X_{inc}) for which the chemical potential is equal to 0:

$$\frac{\partial G}{\partial X} = \frac{\partial H}{\partial X} - T\frac{\partial S}{\partial X} = 0. \tag{4.16}$$

Assuming the enthalpy curve is linear at low values of X and considering the presence of oxides such as SiO_2, the change in enthalpy with respect to X is:

$$\frac{\partial H}{\partial X} = \frac{\Delta H_1}{X_1} + (slope), \tag{4.17}$$

where 'slope' represents the slope of the line connecting the most favorable end-member energies for X = 0 $(H_{SiO_2} + H_{ZrO_2} - H_{ZrSiO_4})$ with either $(H_{SiO_2} + H_{TiO_2(II)} - H_{TiSiO_4})$ for substitution into the Zr site or $(H_{TiO_2(II)} + H_{ZrO_2} - H_{ZrTiO_4})$ for substitution into the Si site (see Figure 4.9 and discussion above). The entropy change at high temperatures may be approximated by the point entropy (eq. (4.15)) (Becker et al., 2000). Taking the derivative of the entropy, substituting, and solving for $X_{\text{inc, }\partial G/\partial X=0}$ in equation (4.16) gives:

$$X_{inc} = \frac{e^{\left(\frac{\Delta H_1}{X_1} + (slope)\right)\left(\frac{1}{RT}\right)}}{1 + e^{\left(\frac{\Delta H_1}{X_1} + (slope)\right)\left(\frac{1}{RT}\right)}}. \tag{4.18}$$

Estimates of the maximum amount of Ti that can be incorporated into each site as a function of temperature and pressure are shown inFigure 4.10. As shown in the graph of excess energies (Figure 4.9) at 0 GPa substitution of Ti into the Si site is expected to dominate, whereas at 10 GPa, substitution into the Zr site is calculated to

dominate. The amount of Ti incorporated at temperatures below about 1000 K is extremely low in all cases, which is in general agreement with experiments (Harley and Kelly, 2007).

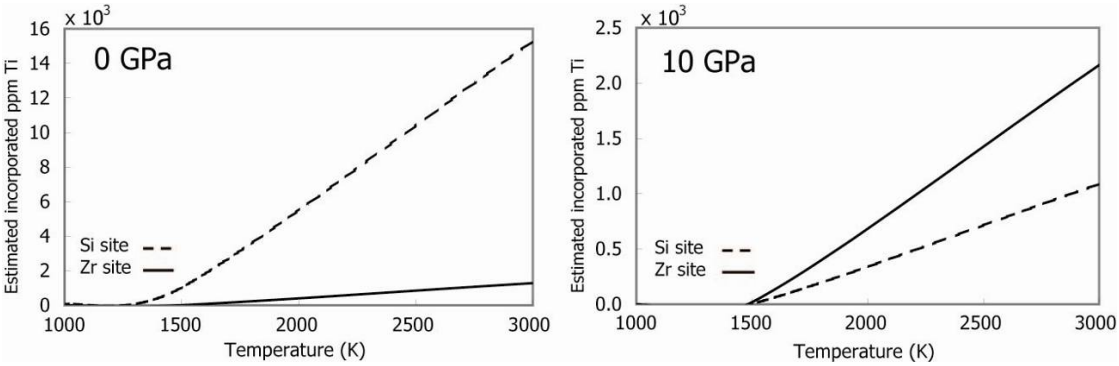

Figure 4.10. Estimated maximum amount of Ti allowed in Si or Zr site of zircon as a function of temperature and pressure. At 0 GPa substitution of Ti into the Si site is expected to dominate, while at 10 GPa substitution into the Zr site is expected to dominate. As pressure increases, less Ti may be substituted into either site (note scale change). Incorporated Ti at temperatures below about 1000 K is extremely low in all cases.

4.5c. Pressure correction to Ti-in-zircon thermometer at low pressures

Assuming that the zircon was formed at pressures low enough for substitution into the Si site to dominate, the effect of changing pressure (P) and temperature (T) on Ti concentration is related to the Clapeyron slope of equation (4.3):

$$\frac{dP}{dT} = \frac{\Delta S}{\Delta \mathrm{V}}, \tag{4.19}$$

where ΔV and ΔS are the volume and entropy changes between the products and the reactant assemblages. Ionic radii arguments suggest that $\Delta V_{(4.3)}$ will be positive, and therefore that the proposed thermometer records only minimum temperatures for zircons formed at high pressures (Page *et al.*, 2008).

The $\Delta V_{(4.3)}$ was previously calculated with volume data for the zirconium titanate $ZrTiO_4$ in the srilankite-related structure (space group *Pbcn*), assuming a linear variation in volume for $ZrSiO_4$ the $ZrTiO_4$ binary. This volume was used to estimate a pressure correction of 50 ºC/GPa at 750 °C (Ferry and Watson, 2007). However, because the actual $ZrTiO_4$ component of equation (4.3) must necessarily share the same structure as zircon (space group $I4_1/amd$), that pressure correction is questionable. To determine the most accurate $\Delta V_{(4.3)}$ possible, quantum-mechanical calculations were used first to confirm the volume of $ZrTiO_4$ in space group *Pbcn*, and then to simulate $ZrTiO_4$ in the zircon structure. Determining the volume of $ZrTiO_4$ in srilankite-like structure is not straightforward because the Zr and Ti sites are disordered. Two possible configurations calculated with DFT using CASTEP have an average volume of 39.73 cm^3/mol, which is close to 39.63 cm^3/mol measured experimentally by Troitzsch & Ellis (2004).

The molar volume of $ZrTiO_4$ in the zircon structure was calculated using five different quantum mechanical methods at 0 GPa and 0 K (Table 4.7). Each approach has an associated error. For instance, DFT with LDA tends to overestimate the strength of bonds, resulting in volumes that are too small, while DFT with GGA tends to underestimate the bonding, resulting in volumes that are too large. To estimate the systematic error (bias) and random error (variance) of each method, the calculated molar volumes of zircon, rutile, and quartz are compared with those of the experimental values, which are assumed to have negligible error. For consistency with previous estimates, TiO_2 is assumed to be in the rutile structure and SiO_2 in the quartz structure (Ferry and Watson, 2007). With four degrees of freedom, the molar

volume of $ZrTiO_{4(zircon)}$ can be estimated with 95% confidence as 44.21 ± 0.45 cm^3/mol with a resulting ΔV for reaction (4.3) of 9.09 ± 0.45 cm^3/mol.

Table 4.7. Molar volumes in cm^3/mol of $ZrTiO_4$ and $TiSiO_4$ in the zircon structure calculated using several density-functional theory approaches.

Method	$ZrTiO_{4(zircon)}$	zircon	rutile	quartz	estimated bias	variance of unbiased $ZrTiO_4$	Weight
Experimental	-	39.26	18.82	22.96	-	-	-
VASP (LDA)	43.98	39.16	18.41	22.58	-0.30	0.04	0.68
CASTEP (LDA)	42.97	38.01	18.21	22.15	-0.89	0.14	0.19
VASP (GGA)	45.58	40.42	19.05	24.43	0.95	0.56	0.05
CASTEP (GGA)	45.16	40.03	19.19	24.36	0.85	0.36	0.07
Dmol^3 (GGA)	41.89	38.00	17.88	19.66	-1.83	2.19	0.01

The calculated value for ΔV of reaction (3) is approximately twice as large as the previously estimated value of 4.51 cm^3/mol (Ferry and Watson, 2007), with a resulting two-fold increase in the pressure correction of the thermometer. The pressure correction at 750 °C and 1 bar is therefore predicted to be 100 ºC/GPa relative to the previous estimate of 50 ºC/GPa (Ferry & Watson, 2007). The exact slope and pressure correction will vary with pressure and temperature, and calculated temperatures may be misleading at pressures above 2 GPa where substitution into the Zr site becomes more important. As a result of the potentially large correction factor and assumptions made about activities in constructing the Ti-in-zircon thermometer, much caution should be taken during applications especially for ultra-high pressure rocks. Moreover, when attempting to determine zircon crystallization temperatures involving granitic intrusions (Baldwin *et al.*, 2007; Harrison *et al.*, 2007), the required pressure correction is much larger than previously thought.

4.6. Conclusions

Quantum mechanical calculations and, where necessary, subsequent Monte-Carlo calculations were performed to calculate the differences in energy between two possible mechanisms for Ti substitution into zircon, the thermodynamic mixing properties of the $ZrSiO_4$ – $ZrTiO_4$ and $ZrSiO_4$-$TiSiO_4$ binaries, and the changes in volume and lattice parameters for these systems. The calculated volume of 44.21 ± 0.45 cm^3/mol for $ZrTiO_4$ in the zircon structure and resulting change in the calculated ΔV of the reaction for Ti substitution into the Si site indicate a response to pressure twice as large as was previously considered (100 °C/GPa difference rather than 50 °C/GPa near 750 °C). Cluster expansion models (Sanchez *et al.*, 1984) may provide more detailed phase diagrams for the systems, as would an analysis of the importance of the srilankite structure in the binary $ZrSiO_4$-$TiSiO_4$. The results lend further support to the idea that at pressures of 1 GPa and below, Ti substitution in zircon occurs in the Si site rather than in the Zr site. Above 1 GPa, substitution into the Zr site may be more important, and the Ti-in-zircon thermometer should be re-calibrated for higher pressures.

4.7. References

Baldwin, J.A., Brown, M., and Schmitz, M.D. (2007) First application of titanium-in-zircon thermometry to ultrahigh-temperature metamorphism. Geology, 35, 295-298.

Becker, U., Fernandez-Gonzalez, A., Prieto, M., Harrison, R., and Putnis, A. (2000) Direct calculation of thermodynamic properties of the barite/celestite solid solution from molecular principles. Physics and Chemistry of Minerals, 27, 291-300.

Bosenick, A., Dove, M.T., Myers, E.R., Palin, E.J., Sainz-Diaz, C.I., Guiton, B.S., Warren, M.C., Craig, M.S., and Redfern, S.A.T. (2001) Computational methods for the study of energies of cation distributions: applications to cation-ordering phase transitions and solid solutions. Mineralogical Magazine, 65, 193-219.

Burton, B.P., van de Walle, A., and Kattner, U. (2006) First principles phase diagram calculations for the wurtzite-structure systems AlN-GaN, GaN-InN, and AlN-InN. Journal of Applied Physics, 100, #113528.

Ferry, J.M., and Watson, E.B. (2007) New thermodynamic models and revised calibrations for the Ti-in-zircon and Zr-in-rutile thermometers. Contributions to Mineralogy and Petrology, 154, 429-437.

Finch, R.J., and Hanchar, J.M. (2003) Structure and chemistry of zircon and zircon-group minerals. In J.M. Hanchar, and P.W.O. Hoskin, Eds. Zircon. Reviews in Mineralogy & Geochemistry, 53, 1-25.

Fu, B., Page, F.Z., Cavosie, A.J., Fournelle, J., Kita, N.T., Lackey, J.S., Wilde, S.A., and Valley, J.W. (2008) Ti-in-zircon thermometry: applications and limitations. Contributions to Mineralogy and Petrology, 156, 197-215.

Hamann, D.R. (1996) Generalized gradient theory for silica phase transitions. Physical Review Letters, 76, 660-663.

Harley, S.L., and Kelly, N.M. (2007) Zircon - tiny but timely. Elements, 3, 13-18.

Harrison, T.M., Watson, E.B., and Aikman, A.B. (2007) Temperature spectra of zircon crystallization in plutonic rocks. Geology, 35, 635-638.

Hemingway, B.S., Bohlen, S.R., Hankins, W.B., Westrum, E.F., and Kuskov, O.L. (1998) Heat capacity and thermodynamic properties for coesite and jadeite, reexamination of the quartz-coesite equilibrium boundary. American Mineralogist, 83, 409-418.

Hohenberg, P., and Kohn, W. (1964) Inhomogeneous electron gas. Physical Review B, 136, B864-B871.

Kohn, W., and Sham, L.J. (1965) Self-consistent equations Including exchange and correlation effects. Physical Review, 140(4A), 1133-&.

Myers, E.R. (1998) A statistical-mechanics model of ordering in aluminosilicate solid solutions. Physics and Chemistry of Minerals, 25, 465-468.

Page, Z.F., Fu, B., Kita, N.T., Fournelle, J., Spicuzza, M.J., Schultze, D.J., Viljoen, F., Basei, M.A.S., and Valley, J.W. (2008) Zircons from kimberlite: new insights from oxygen isotopes, trace elements, and Ti in zircon thermometry. Geochimica et Cosmochimica Acta, 71, 3887-3903.

Robinson, K., Gibbs, G.V., and Ribbe, P.H. (1971) The structure of zircon: a comparison with garnet. American Mineralogist, 56, 782-790.

Sanchez, J.M., Ducastelle, F., and Gratias, D. (1984) Generalized cluster description of multicomponent systems. Physica A, 128, 334-350.

Shannon, R.D. (1976) Revised effective ionic-radii and systematic studies of interatomic distances in halides and chalcogenides. Acta Crystallographica Section A, 32, 751-767.

Spera, F.J., Yuen, D.A., and Giles, G. (2006) Tradeoffs in chemical and thermal variations in the post-perovskite phase transition: mixed phase regions in the deep lower mantle? Physics of the Earth and Planetary Interiors, 159, 234-246.

Stoyanov, E., Langenhorst, F., and Steinle-Neumann, G. (2007) The effect of valence state and site geometry on Ti L-3,L-2 and OK electron energy-loss spectra of Ti_xO_y phases. American Mineralogist, 92, 577-586.

Watson, E.B., and Harrison, T.M. (2005) Zircon thermometer reveals minimum melting conditions on earliest Earth. Science, 308, 841-844.

Watson, E.B., Wark, D.A., and Thomas, J.B. (2006) Crystallization thermometers for zircon and rutile. Contributions to Mineralogy and Petrology, 151, 413-433.

Withers, A.C., Essene, E.J., and Zhang, Y.X. (2003) Rutile/TiO_2II phase equilibria. Contributions to Mineralogy and Petrology, 145, 199-204.

Yeomans, J.M. (1992) Statistical mechanics of phase transitions. 164 p. Oxford Science Publications, Clarendon Press, Oxford.

CHAPTER 5.

SUMMARY OF MAJOR CONCLUSIONS

The three most important contributions of this dissertation to the study of actinide-bearing materials are as follows: (1) the development of a new conceptual model for spent nuclear fuel corrosion in an iron waste canister, (2) determination of the maximum amount of Pu, U, Th, Ce, or Hf that may be incorporated into zircon, a common mineral and proposed waste form for Pu, and (3) determination of a pressure correction for the Ti-in-zircon geothermometer. These results are complemented by an optimized version of the ferrozine method for determining Fe(II)/Fe(III) ratios in solids and a comparison of the behavior of Tc to its chemical analogue Re.

The study of synthetic UO_2 corrosion in miniature waste packages in Chapter 2 demonstrates that oxidation of UO_2, the major component of spent nuclear fuel (SNF), is minimal in the presence of a relatively large amount of corroding steel over laboratory time-scales. The miniature waste package with greater access to outside air contained a larger amount of dissolved U. Redox estimates inside the package based on Fe(II)/Fe(III) ratios showed a decrease in Eh (or pe) over two years. This decrease in oxygen content resulted in kinetic inhibition of UO_2 corrosion. Based on these results, the oxidative dissolution of spent nuclear fuel in an oxidizing repository with a steel canister may be broken into three phases: (1) prior to breach, when no water is

available and the corrosion rate is negligible, (2) immediately after breach, when the steel begins to corrode, conditions inside of the canister are more reducing, and SNF does not corrode significantly, and (3) long after breach, SNF is exposed to the open air and oxidized. This work will serve as a basis for future experiments on SNF corrosion in oxidizing environments. Future goals of particular importance include understanding the effect of, *e.g.*, different steel types, temperature, redox potentials, and solution composition, as well as estimating time scales for each stage of corrosion in a nuclear waste repository.

Chapter 3 considers the common accessory mineral zircon ($ZrSiO_4$) as a host phase for Pu and other elements, particularly actinides and neutron absorbers such as Hf. Quantum-mechanical and Monte-Carlo simulation results show that while hafnon ($HfSiO_4$) and zircon form a nearly ideal solid solution, the amount of Pu, U, Th, and Ce that can be incorporated into zircon at thermodynamic equilibrium is extremely limited, with exsolution occurring perpendicular to [001] when the solubility limits are exceeded. Binaries with the zircon structure are ranked by extent of miscibility: $(Zr,Hf)SiO_4$ > $(Th,U)SiO_4$ > $(Zr,Ce)SiO_4$ > $(Zr,Pu)SiO_4$ > $(Hf,Pu)SiO_4$ > $(Zr,U)SiO_4$ > $(Zr,Th)SiO_4$. Three of these end-members, $PuSiO_4$, $USiO_4$ and $CeSiO_4$, are determined to be unstable relative to a mixture of their respective oxides (e.g., PuO_2 and $SiO_{2(quartz)}$). The tetragonal polymorph of $ThSiO_4$ is calculated to be marginally stable, but its monoclinic polymorph huttonite is determined to be marginally unstable. Incorporation of Pu, U, Th, or Ce into zircon above about 2 mol % is predicted to be either the result of a persistent metastable state or a heterogeneous mixture of nanoscale phases. These results are valuable for comparing potential

nuclear waste forms and may also lead to refinements of current methods of U/Th/Pb age-dating and unraveling magmatic histories based on rare earth and Hf distributions in zircon.

Chapter 4 explores another geologic application for zircon, the proposed Ti-in-zircon geothermometer (Watson et al., 2006), in more detail. Quantum mechanical calculations confirm that Ti prefers to occupy the Si site at pressures below 1 GPa. However, at higher pressures, particularly above 3.5 GPa, substitution into the Zr site is preferred. Five different quantum mechanical methods were used to determine that tetragonal $ZrTiO_4$, which is unstable relative to $ZrO_{2(baddeleyite)}$ and $TiO_{2(rutile)}$, has a molar volume of 44.21 ± 0.45 cm^3/mol. That result was used to determine the volume change and Clapeyron slope of the reaction $TiO_2 + ZrSiO_4 \leftrightarrow ZrTiO_4 + SiO_2$. These results suggest a pressure correction to the thermometer of 100 °C/GPa at 750 °C, twice as large as a previous estimate. In order to determine a more exact value for the pressure correction, the Ti content of zircon must be measured experimentally as a function of pressures higher than 1 or 2 GPa. The Ti-in-zircon geothermometer is not calibrated above 2 GPa and should not be used on ultra-high pressure samples (*e.g.,* (Baldwin et al., 2007)).

The results presented in this thesis demonstrate the importance of corrosion and substitution processes in determining the usefulness of UO_2 and zircon in nuclear and geological science applications. While these effects are most immediately applicable to studies of nuclear waste forms and thermobarometry, they are also relevant to studies of steel corrosion, the effect of lowered redox conditions, the pressure dependence of solid-state miscibility, methods for comparing miscibility

gaps, and the usefulness of chemical analogs (*e.g.*, UO_2 for spent nuclear fuel in Chapter 2, Ce for Pu in Chapter 3, and Re for Tc in Appendix B). The method developed in Chapters 3 and 4 for estimating incorporation limits in highly-unfavorable solid solutions may be particularly useful, as it can be applied to any system in which some intermediate compositions can be successfully simulated using empirical or quantum-mechanical calculations in combination with Monte-Carlo methods.

5.1. References

Baldwin, J.A., Brown, M., and Schmitz, M.D. (2007) First application of titanium-in-zircon thermometry to ultrahigh-temperature metamorphism. Geology, 35, 295-298.

Watson, E.B., Wark, D.A., and Thomas, J.B. (2006) Crystallization thermometers for zircon and rutile. Contributions to Mineralogy and Petrology, 151, 413-433.

APPENDICES

APPENDIX A.

OPTIMIZED FERROZINE METHOD FOR DETERMINATION OF FERROUS AND FERRIC IRON IN MINERALS

Abstract

An optimized version of the ferrozine wet chemical method for determining iron content and speciation in solids is presented. The ferrozine micro-method begins with sample digestion similar to that used in the Platt method followed by spectrophotometric analysis using the complexing agent ferrozine. This method was tested for 21 rock standards weighing between 5-14 mg and containing 0.37-5.45 mg total Fe and more than 0.29 mg Fe(II), and was determined to be accurate to within 0.23 weight percent FeO and 0.34 weight percent total Fe. The accuracy and precision of this method compare favorably to other wet chemical methods.

Introduction

Accurate determination of the amount and speciation of Fe in silicate solids is important in soil science, and wet chemical techniques are often used because of their convenience and ability to determine bulk Fe(II) and Fe(III) concentrations even when the sample contains more than one mineral species or if the structure of the phase or phases is unknown (e.g., (Stucki and Roth, 1977; Phillips and Lovley, 1987; Stucki et al., 1987; Wu et al., 1988; Khaled and Stucki, 1991; Gao et al., 2002; Rakshit et al., 2008). Much has been written comparing the various wet chemical

methods (Schafer, 1966; Lalonde et al., 1998), and identifying the optimal procedure continues to be an area of active research (Anastácio et al., 2008).

Several other colorimetric methods have been used, but the ferrozine method remains superior for its accuracy and low detection limit. For instance, the colorimetric Wilson method (Wilson, 1960) for Fe(II) and FeT involves the addition of excess vanadium to keep the Fe(II) reduced during acid digestion, followed by back-titration with bipyridyl indicator to determine the amount of Fe(II). However, in at least one study (Lalonde et al., 1998), the Wilson method has been found to yield inaccurate results. In contrast, for acid mine waters, ferrozine has been shown to provide reliable, precise, and sensitive Fe(II) measurements and FeT measurements more accurate than those produced using direct-current plasma atomic-emission spectrometry, flame atomic-absorption spectrometry, graphite furnace atomic emissions spectrometry, or inductively coupled plasma atomic-emission spectrometry (Ball and Nordstrom, 1994).

Another colorimetric method commonly used in solids determination utilizes 1,10-phenanthroline as a spectrophotometric reagent absorbing at 510 nm (Stucki, 1981). This technique, which was developed specifically for use in silicate rocks, has been presented as superior to the traditional ferrozine method applied to solids as presented in Lovley and Phillips, (1986) because of 1) ease of procedural setup, 2) reliable completion of sample digestion, and 3) relative invulnerability to photochemical reduction after a period of four hours (Anastácio et al., 2008). However, the large molar absorptivity of ferrozine (27,900 $M^{-1}cm^{-1}$) compared to that of 1,10-phenanthroline (11,100 $M^{-1}cm^{-1}$) results in a detection limit 2.5 times lower

for ferrozine than for 1,10-phenanthroline (Stookey, 1970). Therefore ferrozine continues to be the spectrophotometric agent of choice in very small samples. The procedure described here is an optimized version of the ferrozine method, suitable for determining both Fe(II) and Fe(III) in samples containing 0.37-5.45 mg total Fe and more than 0.29 mg Fe(II).

Methods

Description of method

The ferrozine micro-method (FMM) is based on a combination of sample dissolution using the acids H_2SO_4 and HF (a digestion procedure that has been well established for silicates for over a century (Pratt, 1894) and the ferrozine spectrophotometric technique originally developed for aqueous samples (Stookey, 1970). The traditional Pratt approach to digestion is modified by replacing platinum crucibles with cost effective Teflon® beakers to minimize physical sample loss (e.g. spatter) in boiling. Also, the possibility of oxidation is further reduced by the use of two hot plates at different temperatures. The samples in covered beakers are first warmed in H_2SO_4 to near-boiling on a low-temperature hotplate. Hydrofluoric acid is added and the samples are placed on a higher temperature hotplate to induce immediate boiling. Practice is necessary to obtain optimum hot plate settings. As in most sample digestion approaches, there are potential health hazards, especially when working with H_2SO_4 and HF. Beakers containing HF should never be removed from the fume hood prior to the addition of H_3BO_3, and safety goggles as well as special gloves are required, as samples may splatter if overheated.

In a 50 mL Teflon® beaker, 4.0 mL of 1:1 H_2SO_4 is added to a previously weighed and slightly moistened sample. The sample in the H_2SO_4 is heated to near-boiling on a hot plate before the addition of 2.0 ml of 47% HF. The beaker is covered by a Teflon® watch cover immediately after HF addition and transferred to a second hotplate that is set on a sufficiently high setting to initiate immediate boiling. After 10 minutes of rapid boiling, the sample, which should be completely dissolved, is removed from the hotplate and allowed to cool slightly to end boiling and allow handling. The beaker cover is carefully slid over just far enough to add 10mL saturated boric acid (7.2 g H_3BO_3 in 120 mL H_2O). The H_3BO_3 complexes the HF, thereby preventing oxidation of Fe(II), reducing the hazard due to HF, and preventing the reaction of HF with glass later in the procedure. After the acid digestion, 5.00 mL of ammonium acetate/acetic acid buffer solution (40g $NH_4C_2H_3O_2$, 24 mL H_2O, and 112 mL glacial $HC_2H_3O_3$) are added to increase the pH to within working pH range of approximately 3.5-9. for ferrozine. The solution is transferred to a 50 mL volumetric flask, rinsing the lid and beaker several times with H_2O to ensure quantitative transfer, and the solution is allowed to cool and then diluted to 50 mL.

The Fe(II) and FeT may be determined on separate 2.0 mL aliquots of the 50 mL sample solution by complexation of the Fe(II) with ferrozine and subsequent spectrophotometry, with the important difference that the Fe(III) in the aliquot being used to determine total iron must first be reduced to Fe(II). The 2 ml aliquots are transferred to 50 ml volumetric flasks, and the FeT sample is treated with 2.0 mL of 3% filtered hydroxylamine hydrochloride, a reducing agent, to reduce all Fe(III) to Fe(II). Then, 1 mL of a filtered mixture of 5 g/L ferrozine and 0.01 molar 2-(4-

morpholino)ethanesulfonic acid (MES, an additional pH buffer) is added to each sample. The aliquot is diluted to 50 mL with H_2O and allowed to react with the ferrozine for at least 30 minutes prior to measurement. This extended time for complete color development is particularly important below pH 4.0. The colored complex is stable for at least two hours. The absorbance in our studies was measured with a computer-operated Beckman/Coulter DU 800 spectrophotometer with a 1 cm cell and was then compared to a standard calibration curve prepared with ferrous ammonium sulfate (FAS). The FAS is standardized on the day of use by titrating against standard $K_2Cr_2O_7$. The calibration curve, which should correspond to approximately 2.2 mg/L Fe(II) for each absorbance unit (absorbance = 0.454*concentration in mg/L), is reliable in the range of 0 to 4 mg/L. Larger concentrations of Fe in samples can be measured using dilutions, and for very low levels of Fe (less than 0.05 mg) larger aliquots may be taken from the original 50 mL flasks. Reagent disposal requires no special precautions.

Evaluating the method

To test the accuracy of FMM, eight rock standards from the National Institute of Standards and Technology (NIST), GEOSTANDARDS international working group (IWG), and U.S. Geological Survey (USGS) were analyzed 2 to 4 times, and the values obtained were compared to those established. The standards used included a banded iron formation (IWG-IF-G), gabbro (IWG-MRG-1), biotite (IWG-Mica-Fe), phlogopite (IWG-Mica-Mg), diorite (IWG-DRN), and three basalts (NIST-688, IWG-BR, and USGS BCR-1). Samples ranged in mass between 5 and 14 mg, with most between 8-10 mg. FeO weight percentages ranged between 5.40 and 18.91.

Results and discussion

Accuracy and precision of method

Results are reported in Table A.1 and compared with literature values in Figure A.1 and Figure A.2 (Govindaraju, 1994). Precision was evaluated by determining the residual (random) error. This was accomplished by forcing straight-line fits through the origin in both sets of data shown in Figure A.1 and Figure A.2. Deviations of the data from that straight line were binned and are shown in Figure A.3 and Figure A.4. Random error standard deviations of 0.23 and 0.34 for wt % FeO and wt % FeT respectively, compare favorably to precision values obtained for other wet chemical methods such as the original Pratt method, which was measured to have a precision of 1.2 wt % FeO (Lalonde et al., 1998). In all cases but one, the FeT for IF-G, the measured values are within the uncertainty in the values as reported in the literature.

Sources of error

Sample preparation for FMM requires the use of optimal grinding conditions and careful consideration of the sample mass, size distribution, and homogeneity. To prevent contamination during the initial sample crushing, only Fe-free pulverizing equipment such as agate, mullite, or preferably alumina (e.g. Diamonite™) should be used. The grains should be crushed only to the extent that they can be readily dissolved. This minimizes any contamination and changes in water content (Hillebrand and Lundell, 1958; Wilson, 1960). While oxidation during grinding is also a concern, neither crushing and dissolution, brief grinding for 15 to 30 minutes in

air, nor longer periods of grinding in alcohol have been found to cause marked oxidation in a wide variety of rock types (Hillebrand and Lundell, 1958). Samples with low weight (below about 10 mg) may give results that are not representative of the original sample, if the sample is not homogeneous. Rigorous treatment of these criteria is beyond the scope of this paper and can be found in analytical chemistry textbooks and the literature (Hillebrand and Lundell, 1958; Kolthoff and Elving, 1978; Ingamells and Pitard, 1986; Kane, 1997).

Table A.1 Results of ferrozine micro-method tests in weight % FeO and weight % total iron (FeT) for selected silicate standards.

Standard	688	BCR-1	BR	DRN	IF-G	Mica-Mg	Mica-Fe	MRG-1
FeO measurement	7.49	8.75	6.56	5.14	16.3	6.81	18.6	8.83
	7.6	9.1	6.61	5.24	16.6	6.6	19.3	8.87
	7.62				16.75			8.7
	7.35							9.09
FeT measurement	9.68	12.76	12.35	9.21	52.75	8.54	23.41	16.91
	9.59	12.88	12.18	8.80	54.00	8.72	24.08	16.99
	9.38				53.95			17.17
	9.12							17.38
Average FeO	7.52	8.92	6.58	5.19	16.6	6.70	19.0	8.87
Average FeT	9.44	12.82	12.27	9.01	53.57	8.63	23.75	17.11
Literature Value FeO[a]	7.64	8.88	6.57	5.40	16.78	6.73	18.91	8.66
Literature Value FeT[a]	9.50	12.47	12.15	9.10	53.98	8.71	23.55	17.02
Lit. FeO Uncertainty[a]		0.28	0.15		0.3	0.44	0.41	
Lit. FeT Uncertainty[a]		0.36	0.15		0.22	0.18	0.27	

[a](Govindaraju, 1994)

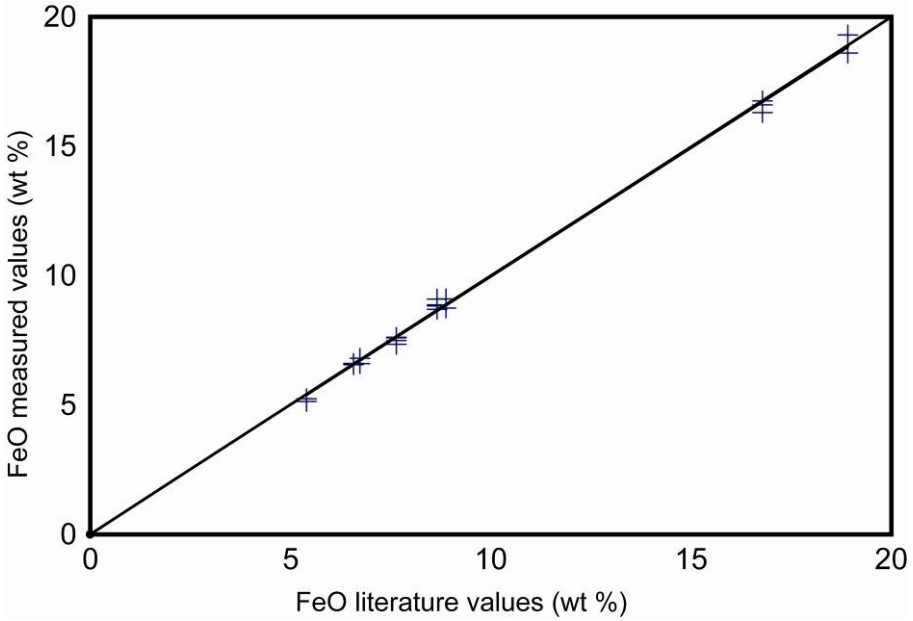

Figure A.1 Fe(II) as wt % FeO obtained using ferrozine micro-method as a function of the accepted literature values compared to a 1:1 line.

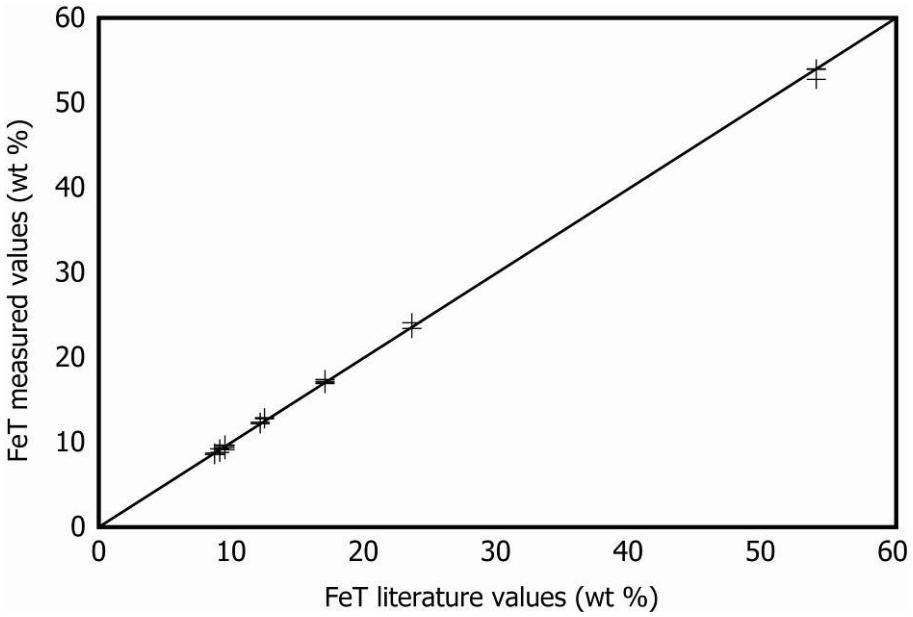

Figure A.2 Weight percent total iron (FeT) obtained using ferrozine micro-method as a function of literature values compared to a 1:1 line.

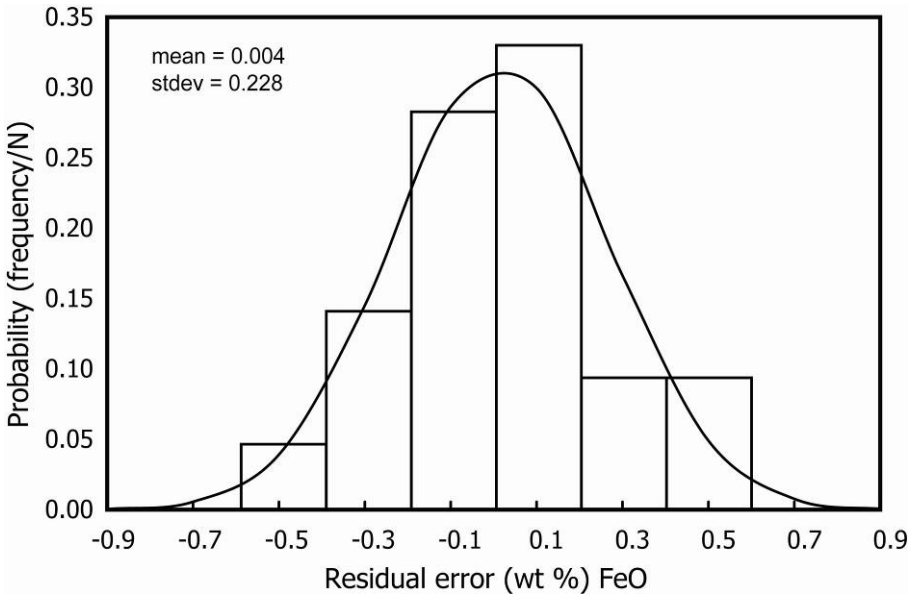

Figure A.3 Relative-frequency histogram for FeO wt % obtained using the ferrozine micro-method relative to the best-fit line from the comparison of measured and accepted values (Table A.1). The mean is 0.004, the standard deviation is 0.23, and N, the total number of measurements, is 21.

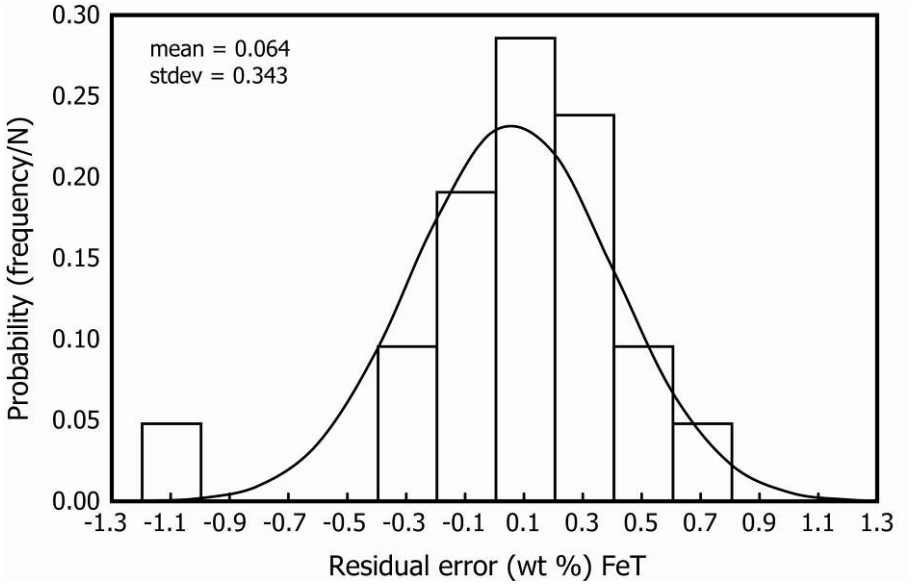

Figure A.4 Probability histogram for weight percent FeT obtained using the ferrozine micro-method relative to the best-fit line from the comparison of measured and accepted values (Figure A.2). The mean is 0.064, the standard deviation is 0.34, and N, the total number of measurements, is 21.

Conclusions

The ferrozine micro-method is a useful tool in the quantitative determination of ferrous and total iron. The importance of FMM has been demonstrated both in studies of iron-rich amphiboles and biotites involved in volcanic processes (Underwood et al., 2009) and in the characterization of steel corrosion products (Ferriss et al., 2008a). This method was tested for 21 samples between 5-14 mg containing between 5 and 19 weight percent FeO and between 8 and 54 weight percent total Fe and determined to be accurate to within 0.23 weight percent FeO and 0.34 weight percent total Fe.

References

Anastácio, A.S., Harris, B., Yoo, H.-I., Fabris, J.D., and Stucki, J.W. (2008) Limitations of the ferrozine method for quantitative assay of mineral systems for ferrous and total iron. Geochimica et Cosmochimica Acta, 72, 5001-5008.

Ball, J.W., and Nordstrom, D.K. (1994) A comparison of simultaneous plasma, atomic absorption,and colorimetric determinations of major and minor constituents in acid mine waters. USGS Water Resources Investigations.

Ferriss, E.A., Helean, K.B., Bryan, C.R., Brady, P.V., and Ewing, R.C. (2008) UO_2 Corrosion in an Iron Waste Package. Journal of Nuclear Materials, 384(2), 130-139.

Gao, S., Tanji, K.K., Scardaci, S.C., and Chow, A.T. (2002) Comparison of redox indicators in a paddy soil during rice-growing season. Soil Science Society of America Journal, 66, 805-817.

Govindaraju, K. (1994) Complication of working values and sample description for 383 geostandards. Geostandards Newsletter, 18.

Hillebrand, W.F., and Lundell, G.E.F. (1958) Applied Inorganic Analysis. John Wiley & Sons, New York, 907 p.

Ingamells, C.O., and Pitard, F.F. (1986) Applied Geochemical Analysis. 733 p. Wiley, New York.

Kane, J.S. (1997) Analytical bias: the neglected component of measurement uncertainty. Analyst, 122(11), 1283-1288.

Khaled, E.M., and Stucki, J.W. (1991) Iron oxidation-state effects on cation fixation in smectites. Soil Science Society of America Journal, 55(2), 550-554.

Kolthoff, I.M., and Elving, P.J. (1978) Treatise on Analytical Chemistry, Wiley, New York, 700 p.

Lalonde, A.E., Rancourt, D.G., and Ping, J.Y. (1998) Accuracy of ferric/ferrous determinations in micas: A comparison of Mössbauer spectroscopy and the Pratt and Wilson wet-chemical methods. Hyperfine Interactions, 117, 175-204.

Lovley, D.R., and Phillips, E.J.P. (1986) Organic-matter mineralization with reduction of ferric iron in anaerobic sediments. Applied and Environmental Microbiology, 51(4), 683-689.

Phillips, E.J.P., and Lovley, D.R. (1987) Determination of Fe(III) and Fe(II) in Oxalate Extracts of Sediment. Soil Science Society of America Journal, 51(4), 938-941.

Pratt, J.H. (1894) Determination of Fe(III) and Fe(II) in oxalate extracts of sediment. American Journal of Science, 48, 149.

Rakshit, S., Matocha, C.J., and Coyne, M.S. (2008) Nitrite reduction by siderite. Soil Science Society of America Journal, 72(4), 1070-1077.

Schafer, H.N.S. (1966) Determination of Iron(2) Oxide in Silicate and Refractory Materials .I. A Review. Analyst, 91(1089), 755-762.

Stookey, L.L. (1970) Ferrozine - a new spectrophotometric reagent for iron. Analytical Chemistry, 42(7), 779.

Stucki, J.W. (1981) The quantitative assay of minerals for Fe2+ and Fe3+ using 1,10-phenanthroline .2. a photochemical method. Soil Science Society of America Journal, 45(3), 638-641.

Stucki, J.W., Komadel, P., and Wilkinson, H.T. (1987) Microbial reduction of structural iron(III) in smectites. Soil Science Society of America Journal, 51(6), 1663-1665.

Stucki, J.W., and Roth, C.B. (1977) Oxidation-reduction mechanism for structural Iron in nontronite. Soil Science Society of America Journal, 41(4), 808-814.

Underwood, S., Feeley, T.C., and Clynne, M.A. (2009) Multiple mafic magma injections in shallow silicic magma chambers at Lassen Volcanic Center, California: thermal input and volatile loss record in amphibole and biotite phenocrysts. Journal of Volcanological and Geothermal Research, submitted.

Wilson, A.D. (1960) The micro-determination of ferrous iron in silicate - minerals by a volumetric and colorimetric method. Analyst, 85(1016), 823-827.

Wu, J., Roth, C.B., and Low, P.F. (1988) Biological reduction of structural iron in sodium-nontronite. Soil Science Society of America Journal, 52(1), 295-296.

APPENDIX B.

PERRHENATE AND PERTECHNETATE BEHAVIOR ON IRON AND SULFUR-BEARING COMPOUNDS

Abstract

Investigations of the behavior of the isotope ^{99}Tc frequently use a stable isotope of rhenium as an analogue. This is based on their similar radii, major oxidation states of +7 and +4, and analogous eH-pH diagrams. However, recent studies have shown this analogy to be imperfect (Wharton et al., 2000). Therefore, one goal of this study is to compare the behavior of these elements, with an emphasis on the adsorption of perrhenate (ReO_4^-) and pertechnetate (TcO_4^-) (the major forms of Re and Tc in natural waters) onto mineral surfaces.

Quantum mechanical calculations were performed for the adsorption of perrhenate and pertechnetate anions onto relaxed clusters of the well-characterized sulfide galena (PbS). These provide insight into differences between adsorption behavior, including geometry, adsorption energies, and electronic structure of the two anions. Differences between interactions on terraces and step edges, the effects of co-adsorbates such as Na^+ and Cl^-, and chloride complexation were also explored. The influence of water was calculated using homogeneous dielectric fluids. As a complement to the calculations, batch sorption tests are in progress involving ReO_4^-

/TcO_4^- solution in contact with Fe metal, 10% Fe-doped hydroxyapatite, goethite, hematite, magnetite, pyrite, galena, pyrrhotite and sphalerite.

Introduction

The element Tc is of interest because its radioactivity (^{99}Tc, its most stable isotope, has a half-life of 213,000 years) and high mobility suggest that it will be a major contributor to long-term dose on release from a nuclear waste repository. When Tc is in a reduced oxidation state of 4+, the element tends to form relatively insoluble solids such as TcO_2 and TcS_2. However, oxidized Tc^{7+} forms the pertechnetate ion TcO_4^-, which is highly mobile in natural oxygenated waters because most potentially adsorbent mineral surfaces are also negatively charged. Recent interest has focused on TcO_4^- interactions with iron sulfides that may sorb the ion and possibly reduce the Tc to a less soluble form.

Unfortunately, absorption experiments are often difficult to perform because of the radioactivity associated with Tc. Therefore, Re, which is directly below Tc in the periodic table, is frequently used as a chemical analogue for Tc. This analogy is justified primarily based on the similar radii and major oxidation states of the two ions, as well as the dominance of pertechnetate and the analogous perrhenate (ReO_4^-) over similar ranges of Eh-pH space (Brookins, 1986; Darab and Smith, 1996). However, according to these Eh-pH diagrams, the two elements form different solids under reducing conditions (*e.g.*, TcO_2 and Tc_3O_4 vs. ReO_3 and ReO_2). Furthermore, experimental studies have shown the analogy to be imperfect in the following situations: i) during preparation of pyrochlore and spinel (Muller et al., 1964), ii) in

the presence of Cl^- (Colton, 1962; Volkovich et al., 2002), iii) on mackinawite (FeS) surfaces (Wharton et al., 2000), and iv) in biological systems (Cataldo et al., 1983; Ishii et al., 2004).

In order to make detailed comparisons between Tc and Re and to investigate possible paths for the adsorption and subsequent reduction of pertechnetate and perrhenate on mineral surfaces, quantum mechanical calculations were performed on the adsorption of pertechnetate and perrhenate on the well-understood surface of galena (PbS). A similar technique will be applied to other reducing mineral surfaces such as pyrite and mackinawite, which include the two redox sensitive elements Fe and S, and magnetite, which contains both Fe3+ and Fe2+.

Methods

The quantum mechanical program package Gaussian03 (Frisch et al., 2004) was used to calculate the optimized geometry and electronic stuctures of Tc, Re, and their compounds both alone and on relaxed galena clusters. Clusters were selected over periodic slabs so that charged adsorbates could be calculated alone on the surface. Terraces were modelled using a 4 x 4 x 2 atom cluster, and steps were modelled using 6 x 4 x 2-3 atom clusters (Figure B.1 and Figure B.2). Because the calculations scale roughly to the number of electrons cubed, the total size of the cluster is a limiting factor. The small size may adversely affect the accuracy of the calculations, both because the influences of bulk and outer atoms are not included and through the generation of edge effects (Becker et al., 1997). In order to minimize these problems, cluster atoms far from the adsorbate were held fixed, and atoms along the edges near the adsorbate were only allowed to relax in a direction perpendicular to

the surface. All calculations were made first using the Hartree-Fock (HF) algorithm for solving the Schrödinger equation and the LANL2 small core type pseudopotential (Wadt and Hay, 1985). In some cases, the atoms were optimized a second time both to take electron correlation into account by using a hybrid of HF and density functional theory (B3LYP in Gaussian) and to allow the program to account for electron movement within an atom by including polarization functions (extra basis functions containing no electrons) (Check et al., 2001). Hydration was simulated by imposing a homogeneous dielectric field.

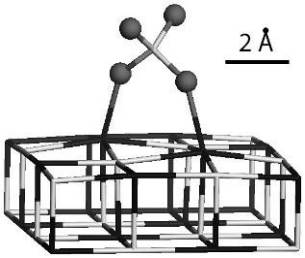

Figure B.1 The most stable geometry for perrhenate and pertechnetate adsorption onto a galena cluster. Light atoms in the slab are S, darker atoms in the slab are Pb, the central atom above is Tc or Re, and the four outer atoms in the adsorbate are O.

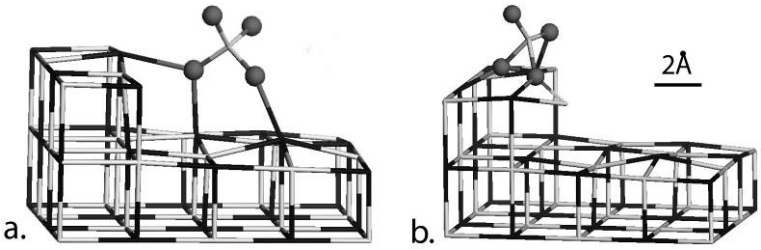

Figure B.2 Two possible final positions for TcO_4^- and ReO_4^- on a cluster representing a galena step. ReO_4^- prefers position a, while TcO_4^- prefers position b.

Results

Initial comparison of Re and Tc and their oxyanions

Pertechnetate and perrhenate have similar binding energies, bond lengths, and hydration spheres. According to the calculations, the binding energy of TcO_4^- is -388.7 eV, and that of ReO_4^- is -371.1 eV. In vacuum, the bond lengths of Tc-O and Re-O are 1.73 Å and 1.74 Å respectively, and the hydration energy is -2.4 eV for TcO_4^- and -2.5 eV for ReO_4^-. These hydration energies are in agreement with those calculated using Born theory as modified by (Rashin and Honig, 1985), in which the molecule is assumed to be spherical with a radius equal to the calculated bond length plus the ionic radius of oxygen.

Adsorption of TcO_4^- and ReO_4^- onto Galena Terraces and Steps

All adsorption energies were calculated with the hydration energies taken into account according to the following general equation:

$$E_{ads.\ hyd.} = E\,(PbS\text{-}TcO_4^-{}_{(vacuum)}) + (X * E_{hydration}\ TcO_4^-) - E\,(PbS_{(s,\ vacuum)}) - E\,(TcO_4^-{}_{(hyd)}) \quad \text{(B.1)}$$

The value of X, an approximation of the amount of hydration energy that is retained, varies with the adsorption geometry. Pertechnetate and perrhenate were adsorbed onto a galena terrace according to the following equations:

$$Pb_{16}S_{16} + TcO_4^- \rightarrow Pb_{16}S_{16}\text{-}TcO_4^- \quad \text{(adsorption energy = - 0.087 eV)} \quad \text{(B.2)}$$

$$Pb_{16}S_{16} + ReO_4^- \rightarrow Pb_{16}S_{16}\text{-}ReO_4^- \quad \text{(adsorption energy = - 0.084 eV)} \quad \text{(B.3)}$$

The adsorption of TcO_4^- is similar to that of ReO_4^-, being only slightly more favorable (0.003 eV) and with a similar geometry. Multiple configurations of the

anions on the terrace were tested, and the most stable for both, in which two oxygen atoms sit above two Pb atoms in the galena, is shown in Figure B.1. After adsorption the Re and Tc both become more positive according to Mulliken charges. Also, the two oxygen atoms closest to the cluster have bond lengths of 1.75Å to the central atom (0.04 Å longer than the bond lengths of the upper oxygens) and more negative Mulliken charges (-0.56 as opposed to -0.52). These shifts in electron density and atomic position show the effects of polarization as the molecule approaches two positively charged Pb atoms in the cluster. Although there are changes within the molecules, both pertechnetate and perrhenate preserve their original total charge, indicating that the interaction is almost entirely ionic.

The same procedure was performed on clusters representing step edges. In this case two potentially stable final geometries were observed (Figure B.2). The first of these is similar to adsorption onto a terrace, but the oxygen nearest the step is also coordinated with a Pb atom at the top of the step. Both anions adsorb to the step edge more strongly than to terraces, with TcO_4^- adsorption ($E_{ads.}$ = -0.21 eV) again more favorable that ReO_4^- adsorption ($E_{ads.}$= -0.14 eV). As on the terraces, Mulliken charges again indicate an exclusively ionic interaction.

However, in the second possible final position, in which the anion sits slightly above a highly distorted step, the Mulliken charges show a reduction of the anions from total charge of -1 to -2, indicating a transfer of one electron from the galena cluster to pertechnetate or perrhenate. This position is favorable for TcO_4^- ($E_{ads.}$ = -1.15 eV as opposed to -0.21 eV in the first position) but unfavorable for ReO_4^- ($E_{ads.}$ =

+ 0.68 eV). This suggests that TcO_4^- will be reduced by galena near step edges, but ReO_4^- will not.

Co-adsorbates Na^+ and Cl^-, and Cl^- complexes

Although it is important to understand the interactions of pertechnetate and perrhenate alone on mineral surfaces, in nature other ions are likely to be present. Na^+ was considered as a representative co-adsorbate for neutral conditions, and the effect of Cl^- was also investigated because of the potential importance of Cl^- salts during spent fuel processing. For this reason and because differences between the two elements have already been noted in the presence of Cl^- (Volkovich et al., 2002), hydrated chloride complexes were also investigated in more detail.

In the presence of Na^+, adsorption on a galena terrace becomes more favorable in both cases, with adsorption energy increasing from -0.08 eV to -2.1 eV in both cases. However, during adsorption, both pertechnetate and perrhenate retain their ionic character when either Na^+ or Cl^- is considered as co-adsorbates on the terrace. The primary difference between the two co-adsorbate cases is that while Na^+ promotes adsorption, the presence of Cl^- causes adsorption to become unfavorable in both cases, with adsorption energies of 0.64 eV and 0.85 eV for TcO_4^- and ReO_4^- respectively.

To investigate the effects of Cl^- further, several Re and Tc chloride complexes were simulated to compare their relative complexation energies. They were calculated in vacuum according to the following equation:

$$E_{complex} = E\left[(Tc,Re)^y Cl_x\right]^{(y-x)} - E\,(Tc,Re)^y - (X^* E\,(Cl^-)) \qquad (B.4)$$

The observed aqueous chemistry of these elements differs from these simple complexes because of the complicating influences of water and other aqueous species (Said et al., 2000). Nonetheless, differences in Cl^- complexes of Re and Tc, shown in Figure B.3, can be used to explore differences in complexation behavior between the elements.

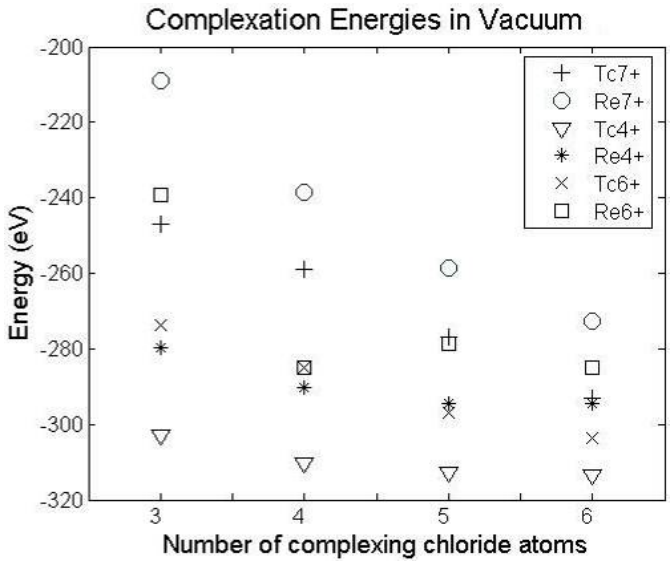

Figure B.3 Complexation energies of three Tc and Re oxidation states with three to six complexing chlorine atoms.

For both elements, the experimentally well-known complexes $TcCl_6^{2-}$ and $ReCl_6^{2-}$ appear to be preferred. They follow the same stability trends in chloride complex formation, with Re^{4+}/Tc^{4+} complexes being most preferred, followed by Re^{6+}/Tc^{6+} and then Re^{7+}/Tc^{7+}. However, the energy gap between the similar Re and Tc complexes is on the order of 20 eV in most cases. This suggests that although trends between isolated complexation of the two elements may be similar, the complexes may behave very differently when competing reactions are considered.

Experimental work

Differences between Tc and Re, and particularly between TcO_4^- and ReO_4^-, should be observed experimentally. While several simple batch experiments have been performed using

both of these species, variable experimental conditions often make them difficult to compare directly. Therefore, as a complement to the above calculations, batch sorption tests are in progress involving ReO_4^- and TcO_4^- solutions in contact with Fe metal, 10% Fe-doped hydroxyapatite, goethite, hematite, magnetite, pyrite, galena and sphalerite. These minerals were chosen because they each contain at least one of the redox sensitive elements, Fe and S. Goethite and hematite, in which the Fe is completely oxidized, are not expected to reduce Tc or Re but are included for comparison with those minerals, such as pyrite and magnetite, that do contain Fe^{2+}. These studies, combined with previous work comparing the two anions (e.g., boehmite studies: (Zhang et al., 2000) should show how comparable their behavior is across a range of conditions.

Conclusions

Perrhenate and perechnetate anions behave similarly in many but not all chemical situations. During ionic interactions on a galena cluster, for instance, the molecules behave nearly identically, but when electron transfer is involved the two ions behave very differently. Perrhenate may be an excellent analogue for pertechnetate, but when anything beyond simple coulombic interactions are involved, the analogy between Re and Tc becomes less useful. Also, given the large gaps in complexation energies between many of the Re and Tc chloride complexes, the analogy may not be useful for Re^{7+} and Tc^{7+} species in general, but only for ReO_4^- and TcO_4^-. Because Re is much easier to work with, using ReO_4^- as an analogue for TcO_4^- can still be useful in the initial stages of an investigation to obtain an understanding of general trends for how Tc might behave. However, results obtained using Re should always be confirmed with experiments on Tc.

References

Becker, U., Greatbanks, S.P., Rosso, K.M., Hillier, I.H., and Vaughan, D.J. (1997) An embedding approach for the calculation of STM images: method development and application to galena (PbS). Journal of Chemical Physics, 107, 7537-7542.

Brookins, D.G. (1986) Rhenium as analog for fissiogenic technetium: Eh-pH diagram (25 °C 1 bar) constraints. Applied Geochemistry, 1, 513-517.

Cataldo, D.A., Wildung, R.E., and Garland, T.R. (1983) Root absorption and transport behavior of technetium in soybean. Plant Physiology, 73, 849-852.

Check, C.E., Faust, T.O., Bailey, J.M., Wright, B.J., Gilbert, T.M., and Sunderlin, L.S. (2001) Addition of polarization and diffuse functions to the LANL2DZ basis set for p-block elements. Journal of Physical Chemistry A, 105, 8111-8116.

Colton, R. (1962) Technetium chlorides. Nature, 193, 872-873.

Darab, J.G., and Smith, P.A. (1996) Chemistry of technetium and rhenium species during low-level radioactive waste vitrification. Chemistry of Materials, 8, 1004-1021.

Frisch, M.J., Trucks, G.W., Schlegel, H.B., Scuseria, G.E., Robb, M.A., Cheeseman, J.R., Jr., J.A.M., T. Vreven, Kudin, K.N., Burant, J.C., Millam, J.M., Iyengar, S.S., Tomasi, J., Barone, V., Mennucci, B., Cossi, M., Scalman, G., Rega, N., Petersson, G.A., Nakatsuji, H., Hada, M., Ehara, M., Toyota, K., Fukuda, R., Hasegawa, J., Ishida, M., Nakajima, T., Honda, Y., Kitao, O., Nakai, H., Klene, M., Li, X., Knox, J.E., Hratchian, H.P., Cross, J.B., Adamo, C., Jaramillo, J., Gomperts, R., Stratmann, R.E., Yazyev, O., Austin, A.J., Cammi, R., Pomelli, C., Ochterski, J.W., Ayala, P.Y., Morokuma, K., Voth, G.A., Salvador, P., Dannenberg, J.J., Zakrzewski, V.G., Dapprich, S., Daniels, A.D., Strain, M.C., Farkas, O., Malick, D.K., Rabuck, A.D., Raghavachari, K., Foresman, J.B., Ortiz, J.V., Cui, Q., Baboul, A.G., Clifford, S., Cioslowsk, J., Stefanov, B.B., Liu, G., Liashenko, A., Piskorz, P., Komaromi, I., Martin, R.L., Fox, D.J., Keith, T., Al-Laham, M.A., Peng, C.Y., Nanayakkara, A., Challacombe, M., Gill, P.M.W., Johnson, B., Chen, W., Wong, M.W., Gonzalez, C., and Pople, J.A. (2004) Gaussian 03, Revision C.02. Gaussian, Inc, Wallingford CT.

Ishii, N., Tagami, K., and Uchida, S. (2004) Physicochemical forms of technetium in surface water covering paddy and upland fields. Chemosphere, 57, 953-959.

Muller, O., White, W.B., and Roy, R. (1964) Crystal chemistry of some technetium-containing oxides. Journal of Inorganic & Nuclear Chemistry, 26, 2075-2086.

Rashin, A.A., and Honig, B. (1985) Reevaluation of the Born model of ion hydration. Journal of Physical Chemistry, 89, 5588-5593.

Said, B.K., Fattahi, M., Musikas, C., Revel, R., and Abbe, J.C. (2000) The speciation of Tc(IV) in chloride solutions. Radiochimica Acta, 88, 567-571.

Volkovich, V.A., May, I., Charnock, J.M., and Lewin, B. (2002) Reactions and speciation of technetium and rhenium in chloride melts: a spectroscopy study. Physical Chemistry Chemical Physics, 4, 5753-5760.

Wadt, W.R., and Hay, P.J. (1985) Ab initio effective core potentials for molecular calculations - potentials for main group elements Na to Bi. Journal of Chemical Physics, 82, 284-298.

Wharton, M.J., Atkins, B., Charnock, J.M., Livens, F.R., Pattrick, R.A.D., and Collison, D. (2000) An X-ray absorption spectroscopy study of the coprecipitation of Tc and Re with mackinawite (FeS). Applied Geochemistry, 15, 347-354.

Zhang, P.C., Krumhansl, J.L., and Brady, P.V. (2000) Boehmite sorbs perrhenate and pertechnetate. Radiochimica Acta, 88, 369-373.